

Jun 2003

## **Vertical Tail Dynamic Response in Vortex Breakdown Flow**

Oleg Levinski

DSTO-RR-0256

**DISTRIBUTION STATEMENT A**

Approved for Public Release

Distribution Unlimited

20030905 032



# Vertical Tail Dynamic Response in Vortex Breakdown Flow

*Oleg Levinski*

**Air Vehicles Division**  
Platforms Sciences Laboratory

DSTO-RR-0256

## ABSTRACT

The paper describes the development of an aeroelastic model for the prediction of empennage dynamic response due to vortex induced buffet loads. The multidisciplinary problem of tail buffeting is solved accurately in the time domain using an unsteady vortex model for prediction of aerodynamic loads and coupled aeroelastic equations for the bending and torsional deflections of the tail which are resolved using the Galerkin method. A dynamic aeroelastic analysis of empennage buffet is performed for a generic delta wing, twin vertical-tail configuration at high angles of attack. Results of computations are validated using experimental and flight test data. The present research provides advances in the predictive capability and our understanding of aircraft empennage buffet.

## RELEASE LIMITATION

*Approved for public release*

AQ F03-11-2459

*Published by*

*DSTO Platforms Sciences Laboratory  
506 Lorimer St  
Fishermans Bend, Victoria 3207 Australia*

*Telephone: (03) 9626 7000  
Fax: (03) 9626 7999*

*© Commonwealth of Australia 2003  
AR-012-790  
June 2003*

**APPROVED FOR PUBLIC RELEASE**

# Vertical Tail Dynamic Response in Vortex Breakdown Flow

## Executive Summary

The airframes of high performance aircraft, such as the F/A-18, have suffered from an aeroelastic tail buffet problem for many years. This problem is inherent to vortical flows used to generate lift at high angles of attack as they tend to break down causing severe empennage dynamic loading and premature fatigue failures.

Better understanding of the empennage buffeting problem is required for development of reliable fatigue usage monitoring systems and for the fleet management of aircraft. The challenges associated with computational simulation of empennage buffet vary from prediction of the nonlinear separated vortical flows about complex configurations to the coupled interaction between the flow and the dynamic response of the tail structure.

The work describes the development and validation of an aeroelastic model for the prediction of the F/A-18 empennage buffet due to bursting LEX vortices under various flight conditions. The multidisciplinary problem of tail buffeting is solved accurately in the time domain using an unsteady vortex model for prediction of aerodynamic loads and coupled aeroelastic equations for the bending and torsional deflections of the tail which are resolved using the Galerkin method.

A dynamic aeroelastic analysis of empennage buffet is performed for a generic delta wing, twin vertical-tail configuration at high angles of attack. Results of flow simulation indicated that the aeroelastic model is able to predict major unsteady features of the vortex induced buffet loads and the resulting coupled fluid-structure interaction.

The present research provides advances in the predictive capability and our understanding of aircraft empennage buffet. Results of the work contribute to DSTO's existing body of knowledge on vortex breakdown and can be used in assessing the buffet environments of current and future generations of fighter aircraft.

## Author

**Dr Oleg Levinski**  
Air Vehicles Division

*Oleg Levinski completed his Bachelor of Science in Aeronautical Engineering (Honours) at the Joukowski Institute of Aviation, Ukraine, in 1985. He has worked for several years with aircraft design and production organisations. He has been awarded 5 patents in the field of aeronautical/mechanical engineering and has published a number of papers. He completed his Doctorate at the University of Melbourne in 1997 and joined the Aeronautical and Maritime Research Laboratory the same year. He is currently a Research Scientist in the Air Vehicles Division and his area of research is computational unsteady aerodynamics, structural dynamics and aeroelasticity.*

---

# Contents

<b>1. INTRODUCTION .....</b>	<b>1</b>
<b>2. AEROELASTIC PHENOMENON OF TAIL BUFFETING.....</b>	<b>2</b>
<b>2.1 Past Experimental Studies.....</b>	<b>5</b>
2.1.1 Sub-scale Model Testing.....	5
2.1.2 Full Scale Tail Buffet Tests.....	9
<b>2.2 Numerical Investigation of Tail Buffeting .....</b>	<b>10</b>
2.2.1 Linear Aeroelastic Models.....	11
2.2.2 CFD/CSD Aeroelastic Solvers.....	12
<b>3. STRUCTURAL DYNAMIC MODEL.....</b>	<b>15</b>
<b>3.1 Governing Equations of Motion.....</b>	<b>16</b>
<b>4. UNSTEADY AERODYNAMIC MODEL .....</b>	<b>21</b>
<b>4.1 Overview of Vortex Method .....</b>	<b>21</b>
<b>4.2 Governing Equations .....</b>	<b>22</b>
4.2.1 Vorticity Production and Convection.....	22
4.2.2 Discretisation of Vorticity Regions .....	24
<b>4.3 Computational Algorithm.....</b>	<b>25</b>
4.3.1 Formulation of the Unsteady Problem.....	25
4.3.2 Representation of the Body and its Wake .....	27
4.3.3 Initial and Boundary Conditions.....	27
4.3.4 Calculation of the Pressure Distribution.....	28
<b>5. NUMERICAL SOLUTION OF AEROELASTIC EQUATIONS .....</b>	<b>30</b>
<b>5.1 Temporal and Spatial Discretisation .....</b>	<b>33</b>
<b>6. COMPUTATION OF VERTICAL TAIL DYNAMIC RESPONSE.....</b>	<b>34</b>
<b>6.1 Computational Model.....</b>	<b>34</b>
<b>6.2 Test Conditions .....</b>	<b>35</b>
<b>6.3 Vortex Wake Structure.....</b>	<b>36</b>
<b>6.4 Vertical Tail Buffet Loading.....</b>	<b>37</b>
6.4.1 Magnitude of Buffet Pressures .....	39
6.4.2 Spectral Content of Buffet Pressures .....	39
6.4.3 RMS Pressure Distribution.....	40
6.4.4 Vertical Tail Buffet Loads.....	42
<b>6.5 Vertical Tail Dynamic Aeroelastic Response .....</b>	<b>44</b>
<b>7. CONCLUSIONS .....</b>	<b>45</b>
<b>8. REFERENCES.....</b>	<b>47</b>

# Nomenclature

$[I]$	Identity matrix
$[K]$	Stiffness matrix
$[M]$	Mass matrix
$A$	Aerodynamic loading vector
$A_i$	Panel area
$A_d$	Dynamic component of aerodynamic loading vector
$A_F$	Tail planform area
$A_s$	Static component of aerodynamic loading vector
$C_F$	Tail root chord
$C_M$	Bending moment coefficient
$C'_M$	Root-mean-square value of bending moment coefficient
$C_N$	Normal force coefficient
$C'_N$	Root-mean-square value of normal force coefficient
$C_p$	Pressure coefficient
$C'_p$	Root-mean-square value of pressure coefficient
$EI$	Distributed bending stiffness
$e_i$	Local truncation error
$E_K$	Kinetic energy of the system
$E_P$	Potential energy of the system
$F$	Static loading vector due to gravity
$f_i$	State variable function
$f_n$	Function of surface geometry and flow velocity
$f_p$	Pressure function
$f_\sigma$	Cut-off function
$GJ$	Distributed torsional stiffness
$g$	Acceleration due to gravity
$I$	Number of bending modes
$I_\theta$	Mass moment of inertia about the elastic axis
$I_{CG}$	Mass moment of inertia about the inertial axis
$J$	Total number of modes
$L$	Vertical tail length
$l_c$	Characteristic length
$l_i$	Distance from the tail root to the centre of the panel
$M$	Distributed aerodynamic pitch moment
$m$	Distributed mass
$M_d$	Dynamic component of distributed aerodynamic pitch moment
$M_s$	Static component of distributed aerodynamic pitch moment
$N$	Distributed aerodynamic normal force
$\mathbf{n}$	Unit normal vector
$N_d$	Dynamic component of distributed aerodynamic force
$N_s$	Static component of distributed aerodynamic force
$p$	Flow pressure
$P'$	Root-mean-square value of pressure
$P_\infty$	Flow pressure at infinity
$Q$	Velocity singular kernel
$q_i$	Generalised coordinate for bending mode

$q_j$	Generalised coordinate for torsion mode
$q_\infty$	Free-stream dynamic pressure
$\mathbf{r}$	Flow field coordinate vector
$\mathbf{r}_p$	Separation line coordinate vector
$\mathbf{r}_s$	Stagnation point coordinate vector
$\mathbf{r}_{\sigma_p}$	Vortex wake coordinate vector
$\mathbf{r}_o$	Body surface coordinate vector
$s$	Parameter along the curve
$t$	Time
$\mathbf{u}$	Flow velocity
$\mathbf{U}$	Body linear velocity
$\mathbf{U}_0$	Flow field characteristic velocity
$\mathbf{V}$	Induced flow velocity
$\mathbf{V}_\infty$	Flow velocity at infinity
$w$	Dimensionless flow velocity
$\mathbf{W}$	Relative flow velocity
$W_A$	Work performed by the aerodynamic loading
$x_{CG}$	Coordinate of inertial axis
$x_e$	Coordinate of elastic axis
$x_\theta$	Local distance between the elastic and inertial axis
$Y$	Bending deflection
$Y_d$	Dynamic component of bending deflection
$Y_s$	Static component of bending deflection
$z$	Distance from the fixed support along the tail elastic axis
$\beta$	Angle between the vertical tail and delta wing plane
$\nu$	Flow viscosity
$\psi_i$	Bending mode shape
$\psi_j$	Torsion mode shape
$\theta$	Torsional deflection
$\theta_d$	Dynamic component of torsional deflection
$\theta_s$	Static component of torsional deflection
$\phi$	Dimensionless velocity potential
$\Gamma$	Circulation of a vortex filament
$\gamma$	Vorticity sheet strength
$\delta$	Vortex core size
$\eta$	Time derivative of generalised coordinate
$\kappa$	Point on a body surface
$\mu$	Variable point on a body surface
$\zeta$	Smoothing function
$\sigma$	Distributed vorticity
$\sigma_p$	Separated vorticity sheet
$\rho$	Flow density
$\Phi$	Velocity potential
$\Omega$	Body angular velocity
$\omega$	Flow vorticity



# 1. Introduction

For modern combat aircraft, the ability to fly and manoeuvre at high angles of attack and at high loading conditions gives tactical advantages. For the F/A-18 aircraft the manoeuvrability at very high angles of attack is achieved through a combination of the wing root leading edge extensions (LEXs) and the placement of twin vertical tails.

A pair of large vortices generated by highly swept wing root LEXs contribute to enhanced vortex lift by developing high suction areas over the wings. The F/A-18 aircraft is designed to utilise unique characteristics of these vortex structures which are prime contributors to the aerodynamics of an aircraft during high angle of attack flight. The twin vertical tails of the F/A-18 aircraft are placed in closer proximity to the LEX vortex flowfield to take full advantage of the concentrated energy contained in the LEX vortices to provide the directional stability and control necessary for high angle of attack manoeuvrability.

However, the characteristics of these LEX vortices are highly sensitive to flight conditions and there is a price for the enhancement in lift. At higher angles of attack, the LEX vortices are unable to withstand large adverse pressure gradients present in the flowfield over the wings and the initially stable vortices tend to break down prior to reaching the vertical tails. Flow reversal in the vortex cores occurs resulting in a highly turbulent flow that impinges on the tail surfaces causing their dynamic loading and vibrations of substantial magnitudes. Here, the appearance of vortex-induced unsteady loads exciting the tail structure is commonly known as buffet while forced response of the tail surfaces to dynamic loading is often referred to as buffeting.

While LEX vortices provide enhanced lift and maneuverability, their breakdown can cause substantial fatigue damage to the vertical tails of the F/A-18 aircraft due to unsteady buffet loading when the dominant frequency of vortex breakdown flow is close to the resonant structural frequencies of the tail structure. Based on original designs and service usage, the aft fuselage and empennage of the F/A-18 aircraft experienced cracks caused by vortex-induced tail buffet at a relatively low number of flight hours, and significant modifications of the empennage structure were required.

To alleviate the buffet loads on the F/A-18 vertical tails, the LEX fence was developed by McDonnell Douglas Corporation using extensive wind tunnel and flight tests. Although a significant reduction of the F/A-18 empennage buffet loads has been obtained as a result of using LEX fences, the search for more effective solutions is still underway for future generation fighter aircraft as their design is still focusing on high angle of attack manoeuvrability at high loading conditions, renewing interest in the empennage buffeting problem. Our ability to understand and predict empennage buffeting may not only help to alleviate inherent problems associated with this flow phenomenon but may also improve aircraft controllability and maneuverability.

The technical challenges associated with the solution of the empennage buffet problem vary from prediction of the nonlinear separated vortical flows about complex configurations to the coupled interaction between the flow and the response motion of the tail structure. Although aeroelastic models based on Euler and Navier-Stokes codes can be applied for the simulation of F/A-18 vertical tail buffeting, they require enormous computing resources to perform parametric studies. Even the single computation of a time-accurate solution of F/A-18 tail buffet at certain flight conditions using the above codes is at the very limit of the capabilities of modern supercomputers. An alternative to computationally intensive Euler and Navier-Stokes codes can be vortex-based methods which provide economy in computations by concentrating their efforts in the areas of high vorticity gradients. The vortex methods are particularly suitable for simulation of vorticity dominated regions, such as flow past a LEX.

The purpose of this research is to provide an improvement in aeroelastic analysis capabilities through the application of the unsteady vortex model to the aeroelastic formulation. This includes the modeling of leading edge vortex development and breakdown, and the interaction of a burst vortex flowfield with flexible vertical tails. Further improvements such as structural nonlinearities can be easily incorporated in the aeroelastic scheme. However, the emphasis in this research is placed on the aerodynamic model and the solution strategy.

## **2. Aeroelastic Phenomenon of Tail Buffeting**

The airframes of high performance aircraft, such as the F/A-18, have suffered from the aeroelastic tail-buffeting problem due to vortex breakdown for many years. This problem is inherent in any aircraft design which relies on the generation of vortex lift for high angle of attack capabilities. Considerable advances have been made during the past decade in the predictive capability and basic understanding of tail buffet. However, this aeroelastic phenomenon still remains one of the most challenging fundamental research problems and the search for more effective solutions to the buffeting problem is still under way for current and future generations of fighter aircraft.

The term 'tail buffeting' was first introduced after an accident resulting in the loss of a small transport airplane at Meopham, England in 1930 [1]. After detailed investigation it was concluded that the most probable cause of the accident was the horizontal tail structural failure due to its intense forced vibrations or 'empennage buffet' caused by turbulent flow separated from wings and fuselage. It was suggested that the aircraft, while in level flight, entered the region of a strong upward gust that resulted in a sharp increase of angle of attack and subsequent flow separation over the wing causing tail buffet.

Due to the nature of its geometry, tail buffeting caused by separating flow over the wing was the major concern for an early fighter-type aircraft where significant buffet usually occurred for moderate angles of attack at high subsonic speeds. The critical combination of buffeting and maneuver loads often occurred while attaining high angles of attack at low subsonic speeds.

Tail buffeting received renewed interest during the last decades with the introduction of fighter aircraft like F/A-18 which have high angle of attack manoeuvring capability typically in the range of up to  $35^\circ$  but some manoeuvres can be performed at  $60^\circ$  or even greater. The aerodynamics of present day fighter aircraft at high incidence is dominated by vortex flows since the wings are usually thin with sharp edges and the forebody is slender. The leading edge extension (LEX) is used in the design of the F/A-18 and other similar type of aircraft for the purpose of generating additional vortex lift at high angles of attack.

Large buffet loads and associated fatigue damage have been observed on the tails of aircraft such as the F/A-18 during certain flight conditions, including rapid maneuvering at subsonic Mach numbers and dynamic pressures considerably less than the maximum allowable values, see Scanlon and Prey [2] and Streber and Rioux [3]. The cause of the buffet was determined to be pressure fluctuations within the turbulent wakes formed by the breakdown of vortices over the upper surface of the wing and/or leading edge extension (LEX) surfaces, see Lee, *et al.* [4] Lee and Valerio [5] and Thompson [6]. During high angle of attack flight conditions, the pressure fluctuations, while essentially broad band and chaotic, revealed high levels of energy in a narrow band of frequency. The dominant frequency corresponding to the spectrum peak was determined to be very near to the frequency of the primary modes of the tail structure. Consequently the structure was excited, producing larger than expected deflections.

Attempts to alleviate severe empennage buffeting led to a variety of experimental and analytical investigations which attempted to clarify and quantify the tail buffet phenomenon, see Zimmerman and Ferman [7] and Zimmerman, *et al.* [8]. The behaviour of these leading edge extension vortices appeared to depend on the angle of attack, wing leading and trailing edge flap settings, and the presence of downstream airframe components such as stabilators and vertical tails and to a lesser extent on the angle of sideslip. Due to the size of the LEXs and their proximity to the forebody, a strong interaction can occur at high angles of attack between the LEX and forebody vortices, and small forebody contour distortions can promote large changes in the behaviour of forebody-LEX vortex interactions. For example, small flow disturbances generated by a nose boom can be amplified downstream by the more powerful LEX vortices affecting aircraft lateral stability at high angles of attack [9].

Separated flow from the main wings has a lesser influence on the vertical tail, but the horizontal stabilators, being in the wake of the wings, are influenced to a much larger extent than by the forebody and LEX vortices [4]. The horizontal tail buffet intensity depends on the angle of attack and stabilator settings, and these angles are related by

the flight control schedule. Detailed investigation of LEX vortices on the horizontal stabilator has not been carried out yet. However, based on the F/A-18 IFOSTP flight tests [3, 10], excitation of the horizontal stabilator was detected in a range between 12 and 28 degrees of angle of attack.

In order to alleviate the F/A-18 buffet problem, McDonnell Douglas Corporation focused their efforts on quantifying the buffet loads and response through wind tunnel studies and flight tests [2, 7, 8]. Based on some of the studies, an interim solution for the F/A-18 consisted of structural modifications to the vertical tail in an attempt to reduce the dynamic stresses in critical areas. However, the dynamic stresses were still too severe. This led to the investigation of a LEX fence which is a flat trapezoidal plate fixed perpendicular to the LEX upper surface and aligned parallel to the aircraft's longitudinal axis. The interaction between the fence and the flow beneath the LEX vortex causes a reduction in the dynamic loads applied to the tail and reduces the peak accelerations in the first modes, but compromises the aircraft's high angle of attack performance and maneuverability [4, 6]. The development of the LEX fence relied exclusively on hundreds of hours of costly wind tunnel testing and clearly showed that more cost effective solutions for predicting empennage buffet are required.

The importance of vertical tail buffeting on the fatigue life of high-performance fighter aircraft was recognised by NASA, and tail buffet became one of the research topics in its High Alpha Technology Program. Collective effort from several US research centres was directed towards investigation of the behaviour of fighter aircraft in the high angle of attack regime with the aim of achieving superior manoeuvrability in future aircraft design. The F/A-18 was chosen as a test bed because it provides a typical example of the dominant vortical flow-field (forebody and LEX vortices) generated by future advanced fighter aircraft [4]. The program involved numerous flight tests, wind tunnel investigations and numerical studies.

The Technical Cooperation Program (TTCP), comprising the Defence Departments of five nations (Australia, Canada, New Zealand, United Kingdom and United States), tasked one of its technical panels (AER TP5) to initiate a cooperative study on the F/A-18 at high angles of attack. This study, that consisted of flight tests, wind tunnel and water tunnel tests of various scale models, as well as numerical investigations, has generated a large aerodynamic database, that contains a wealth of information on aircraft empennage buffet and buffeting.

In 1989, Canada and Australia entered into a collaborative full-scale structural testing program, the F/A-18 International Follow On Structural Test Project (IFOSTP). The aim of IFOSTP was to determine the economic and safe life of the F/A-18 structure under test loading which is representative of Royal Australian Air Force (RAAF) and Canadian Forces (CF) operation conditions. One of the objectives of the IFOSTP was to develop methodologies to alleviate vertical tail buffet loads for the F/A-18 life extension program. A range of wind and water tunnel experiments [6, 11, 12] on F/A-18 sub-scale models as well as several flight test programs [3, 10, 13] were

completed in support of IFOSTP which also provide valuable information for vertical tail buffeting studies.

## 2.1 Past Experimental Studies

The appearance of empennage low speed buffet loads is known to be caused by the leading edge extension separation-induced vortex breakdown that plays a major role in dictating the spectral content of the pressure fluctuations on the tail surfaces. Characteristics of vortex breakdown flow are complex and clearly nonlinear in nature. In the early stages of an aircraft development process, the engineer often relies on either semi-empirical or linear analytic methods. These methods provide, at best, rough estimates of frequency spectrum distributions based on data from similar configurations. Currently available prediction methods are inadequate for rapid and accurate prediction of specific time dependent buffet pressure distributions. Therefore, a heavy reliance on wind tunnel testing of small-scale models persists.

Tests conducted on the F/A-18 have resulted in a large database for various model scales, from small-scale wind and water tunnels up to full-scale. Test data included tail forces and moments, steady and unsteady pressures, vortex breakdown location, tip accelerations and root strains.

Flow visualisation using water tunnels has provided much sought after information on flow physics that is difficult to obtain from wind tunnel or flight tests. The results of surface and off-body flow visualization information has been found extremely useful in the design and implementation of control strategies to alleviate tail buffet loads.

### 2.1.1 Sub-scale Model Testing

The largest amount of wind tunnel testing on the F/A-18 before the TTCP collaborative program and IFOSTP were established had been carried out by McDonnell Douglas during the aircraft development stage. Even the development of the LEX fence involved many hours of wind tunnel tests. Despite the substantial amount of knowledge on vertical tail buffeting accumulated by McDonnell Douglas, most of the results are documented in company reports and are not available in the open literature. It is known that the scale of the McDonnell Douglas wind tunnel model is 12%, and rigid fin pressures were measured and scaled to full aircraft levels [7, 8]. Some tests were also performed with a flexible tail that was dynamically scaled to match the vibration frequencies and mode shapes of the full-scale aircraft. Strain gauges were installed on the wind tunnel model for bending and torsion moment measurements, and accelerometers on the fin tip to detect the response levels. The scaling was carried out such that the dynamic pressures for the wind tunnel tests simulate those at flight.

Some of the first experimental investigations of the vertical tail buffet of the F/A-18 models have been conducted by Sellers, *at al.* [14], Erickson, *at al.* [15], Wentz [16] and

Lee and Brown [17]. These experiments showed that the vortex produced by the wing LEX breaks down ahead of the vertical tails at angles of attack of  $25^\circ$  and higher and the breakdown flow produced unsteady loads on the vertical tails.

Erickson [15] documented results of a wind tunnel test of a 6%-scale model of the F/A-18. He concluded that the high Reynolds number behaviour of the LEX vortex flow can be simulated at lower Reynolds numbers in the wind tunnel and that the vortex core breakdown is relatively unaffected by Mach number until shock waves appear over the wings that interact with the vortices. He also found that the F/A-18 forebody vortices are comparatively weak and are dominated by the LEX vortices at all Mach numbers.

Wentz [16] performed water tunnel tests to study the flow associated with the tail buffet of the F/A-18 aircraft using a 1/48<sup>th</sup> scale model. Coloured dyes were used for flow visualization of LEX vortex breakdown to determine vortex patterns. He also used surface hot film gauge placed on the outboard surface of the starboard tail to measure the heat transfer at the surface and to study the turbulent energy and the frequencies present in the unsteady wake flow. Hot film anemometer signals showed that the tail surface turbulence increased with angle of attack, and that dominant frequencies appear in the flow when breakdown occurred. Comparisons with available wind tunnel measurements showed approximately similar values of the vortex trajectories, breakdown positions and Strouhal numbers for unsteady fin pressures. These confirm the assumption that the fundamental flow patterns are independent of Reynolds number and the water tunnel results are reliable when used to supplement wind tunnel and flight test data.

Investigations of vertical tail buffeting and the effect of the LEX fence on buffet loads were performed by Lee and Brown [17] on a rigid 6% scale model of the F/A-18. The starboard vertical tail was instrumented with 24 fast response absolute pressure transducers on each of the inboard and outboard surfaces. Several strain gauges and accelerometer were installed at the starboard tail and the port tail was also instrumented with strain gauges to provide accurate measurements of the normal force, root bending and torsion moments. The studies also included the forebody pressure distributions, steady and unsteady pressure measurements on the LEX and wing, as well as the flowfield behind the vertical tails. Spectral analyses of the pressure fluctuations on the tail and in the vortical flow region behind the tail revealed the presence of dominant oscillations during buffet. Large reductions in steady and unsteady pressures were detected on the vertical tail inboard surfaces at  $30^\circ$  angle of attack with the LEX fence installed.

Hebbbar, Platzer and Cavazos [18] studied the effect of pitch rate on the development of vortex breakdown using flow visualization results of a 2% F/A-18 model tested in a water tunnel. Results indicated the presence of hysteresis in the instantaneous position of the vortex breakdown point relative to the static case. Thus, the vortex breakdown point moves rearward with increased pitch-up motion and forward with increased pitch-down motion. Vortex core breakdown position was also determined to be a function of yaw angle. The windward vortex breakdown location was seen to

move forward and inboard, while the leeward vortex breakdown point travelled aft and outboard. The results of the study confirmed that aircraft flight dynamics and vortex breakdown dynamics must be considered as coupled events.

Lee and Tang [19] measured the tail buffet on a rigid 6%-scale wind tunnel model of the F/A-18. Strain gauges were used to measure force and moments on the vertical tail surface. Fast response pressure transducers were also installed in the tail surface. Comparison of steady forces and moments on the vertical tail determined from pressure summation and strain gauge measurements showed good agreement. They concluded, that probability density functions of the vertical tail loads as well as pressures on the tail surface at low-pitch frequencies could be represented by Gaussian distributions.

An experimental investigation of vortex-tail interaction on a 76° sharp-edged delta wing, twin vertical-tail configuration has been conducted by Washburn, *et al.* [20]. The vertical tails were placed at nine locations behind the delta wing. The experimental data showed that the aerodynamic loads are more sensitive to the chordwise tail location than its spanwise location. Although the tail location did not affect the vortex core trajectories, it affected the location of vortex-core breakdown, the aerodynamic loads, and the tail buffeting levels. As the tails were moved laterally toward the vortex core trajectory, the buffeting response and excitation were reduced. Moreover, the investigation showed that the presence of a flexible tail could affect the unsteady pressures on the rigid tail on the opposite side of the model. Although the configuration was less complex than the F/A-18, results showed similarities of buffet flow characteristics. As such, this case presents an opportunity to isolate the primary flow features of concern to study the phenomenon and provides data for validation of analytical methods using a simplified model.

A buffet research program was initiated at NASA Langley Research Center (LaRC) to study vortex flowfield mechanisms, with a focus on interaction of the vortical flowfields on tail buffet stability and control, and develop a database relating configuration features to these characteristics. Topics that were directly related to tail buffet modelling and prediction included pressure and response measurements, and the effects of variation in geometry on vortex flow and subsequent impact on tail buffet loads. Shah, *et al.* [21] reported on to effects of leading edge extension modifications on the F/A-18 vertical tail buffet loads. He used a 16% scale model of the production F/A-18 designed originally as a free flight drop model. The port vertical tail was rigid while the starboard tail was flexible and dynamically scaled to match the stiffness, inertia and natural structural frequencies of the F/A-18 full-scale aircraft vertical fins. The buffeting characteristics on the flexible tail were acquired in terms of the tail root bending, mid-span torsion, and leading edge acceleration. Some flow visualisation was conducted using a laser light sheet technique.

Moss, Cole and Doggett [22] also tested a rigid 16%, full-span model of the F/A-18 aircraft that was fitted with flexible vertical tails of different stiffness. Two flexible tails were constructed which had the same planform geometry as the full-scale F/A-18, but

were not dynamically scaled. Vertical-tail buffet response results were obtained over the range of angle of attack from  $-10^\circ$  to  $+40^\circ$ , and over the range of Mach numbers from 0.3 to 0.95. The results were presented in the form of the buffet excitation parameter and indicated that the buffet response occurs in the first bending mode, increases with increasing dynamic pressure and is larger at  $M=0.3$  than that at a higher Mach number.

Moses, *et al.* [23, 24] reported results for a 16% scale wind tunnel model of the F/A-18 employed to study spatial correlation of the buffeting flow at high angles of attack. Unsteady pressures were measured on rigid and flexible tails. Cross-correlation and cross-spectral density functions were presented which illustrate the time lags and phase lags associated with the unsteady differential pressures at stations on the tails. The time and phase lags are characteristic of a wave and were shown to be functions of the distance between stations and the transport velocity. At a given angle of attack, the correlation reportedly scaled with speed, as determined through comparisons with data from other documented tests. Tail flexibility did not appear to significantly affect the time or phase delays. The results presented by Moses provide a better understanding of the complex phenomenon of buffeting, and the statistical analysis showing the existence of coherent structures in the flow over the tail's surface is useful in devising active buffet load alleviation technologies.

The initial flow visualisation tests performed at the Platform Sciences Laboratory of the Defence Science and Technology Organisation (DSTO) were devoted mainly to measurements of the vortex burst positions and comparisons with water tunnel and results from other wind tunnel studies, see [11]. It was shown by Thompson [11] that the vortex burst position was not affected by the flap settings, horizontal stabilator settings, model size and LEX fence installation. However, he found that the presence of engine inlet flow affects the behaviour of the LEX vortex and tends to move the burst point downstream for a fixed angle of attack. Refinement of flow visualisation techniques reported by Thompson [6] allowed studying the topology of the streamlines in the vicinity of the LEX fence. This study shed some light on the effect of the LEX fence on the vortical flow field.

Martin, *et al.* [12] presented results of buffet measurements carried out on a  $1/9^{\text{th}}$  scale model of the F/A-18 in 9ft x 7ft low-speed wind tunnel at the DSTO. The model was mounted on a pitch/roll rig via a six-component strain gage balance and has flow-through engine inlet simulation. A fast response pressure transducer and an accelerometer were located on the outboard side of the port fin. To measure differential steady pressures, there were three pairs of pressure taps, located on opposite sides of the fin. A ground vibration test was performed on the model fin to determine the fin primary bending mode shapes and the natural frequencies. The first natural bending was found to be 68 Hz, which does not correspond to the aircraft frequency of 15 Hz since the model was not aeroelastically scaled. However, excitation of the fin would be expected since this value fell within the range of frequencies that occur in the vortex burst of the  $1/9^{\text{th}}$  scale model at the tunnel speeds where the tests were conducted.



Results of Martin, *et al.* provided valuable insight into the character of the vortex breakdown and subsequent empennage vibration on the F/A-18. Flow visualization measurements with the vertical tail on and off showed that the presence of the vertical tail moves the point of breakdown upstream. Pressure measurements on the wing surface beneath the vortex breakdown and on the vertical tail showed that vortex-breakdown pressure field contained energy over a moderately narrow frequency band. The characteristic frequency was seen to be a linear function of free stream velocity and to vary with angle of attack.

### 2.1.2 Full Scale Tail Buffet Tests

Full-scale tail buffet tests at the NASA Ames Research Center were performed in order to study the flowfield characteristics of tail buffet over a wide range of angles of attack and sideslip, to quantify the effects of LEX fence in reducing the tail buffet loads, and to provide full-scale data for comparison with sub-scale wind tunnel model results. The test article was a full-scale F/A-18 supplied by the US Navy with the aircraft engines and avionics removed. The tests were conducted in the 80 x 120 ft wind tunnel of the National Full-Scale Aerodynamic Complex. The maximum dynamic pressure attainable was 33psf at a maximum velocity of 100 knots.

In the first entry, only 32 transducers were installed on the port vertical tail in a 4 x 4 grid on each side of the tail. Four accelerometers were installed near the tail tips to record response in both bending and torsion modes. The angle of attack ranged from 18 to 50 degrees and the sideslip varied from -15 to 15 degrees. Results on bending moment variations with angle of attack, individual and differential pressure power spectral densities, RMS pressure coefficients and peak power frequencies for the first test were reported by Meyn, *et al.* [25], Meyn and James [26, 27].

In the second wind tunnel entry, pressures were measured using a finer 6 x 8 grid on each side of the tail and James and Meyn [28] showed the effect of spatial resolution of pressure measurements on integrated buffet loads. Their results indicate that the substantial difference in the results between the two wind tunnel entries was due to insufficient number of transducers used in the first test.

Another entry in the 80 x 120 ft wind tunnel was conducted by the USAF [29]. For the majority of the test runs, the conditions were similar to those used in the Meyn and James [28] studies. However, only 72 transducers were installed on the starboard vertical tail. A limited number of runs were carried out at a dynamic pressure of 20 psf with and without the LEX fence. The angle of attack was varied from 20 to 40 degrees and the sideslip from -16 to 16 degrees. Comparison of the RMS differential pressure coefficient maps showed that the LEX fence not only reduces the overall magnitude of the buffet fluctuations, but also alters the shape of the pressure contours along the leading edge and in the tip region.

Meyn, *et al.* [30] presented a correlation of power spectral characteristics of differential pressures measured in flight and on a full-scale, production F/A-18 aircraft in the wind tunnel. For the full-scale F/A-18 wind tunnel test, the maximum wind speed obtained created a spectrum of differential pressures well below the first bending mode of the vertical tail. Therefore, the tails were considered rigid. Comparisons of power spectra of the rigid model pressure coefficients with power spectra of flight data indicated that tail flexibility resulted in lower pressure coefficient values. Further comparisons were made with results from rigid tails on a 12%-scale wind tunnel model. For angles of attack between 28 and 36 degrees, the peak power pressure coefficient was highest on the 12% model and lowest on the aircraft. This trend seems to indicate that the highest pressures are obtained on tails that are most rigid.

Results of full-scale tail buffet investigations at NASA Ames were also compared with those of wind tunnel tests on a 16%-scale model and Moses and Pendleton [31] found that the results from the two models revealed similarities in the trends of the spectral contents as a function of angle of attack. They concluded that characteristics of the differential pressures on the fin surface on smaller wind tunnel models could be scaled up to full scale with good accuracy.

## 2.2 Numerical Investigation of Tail Buffeting

As future military aircraft are also expected to operate at high angles of attack in maneuvering flight, practical methods are needed to accurately account for the buffet loads early in an aircraft development process. Present day methods rely mainly on semi-empirical analysis and use of linear aerodynamics to establish the necessary buffet loads and tail dynamic response for high angle of attack conditions. A popular method developed by Zimmerman and Ferman [7, 8] is based on the premise that some form of buffet data is available through sub-scale wind tunnel tests.

However, the use of linear aerodynamics is not quite correct since the results from flight tests on the F/A-18 vertical tails show large regions of separated flow. The idea of using linear aerodynamics is based on the assumption that even though the flow on the rigid model is highly nonlinear with regions of flow separation, the perturbations on the flow due to the tail vibrations can still be approximately determined from linear theory. This may be valid for attached flows with small amplitudes of tail motion, but when flow separation is present, the tail motion will certainly change the separation and attachment lines on the tail surfaces. The study of aeroelasticity in separated flows is a challenging problem and Forsching [32] discussed the use of semi-empirical aerodynamics for separated flows in estimating the structural response during buffeting.

Much work is required before a better aerodynamic model can be substituted for the widely used linear theory. There is presently no analytical method for the prediction of unsteady separated flows during buffeting. The use of computational fluid dynamics

(CFD) is promising but the computing cost is still prohibitively expensive. The only alternative is to test dynamically scaled flexible models in the wind tunnel, and that is also an extremely expensive and time consuming process. Ideally, this requires matching the Reynolds number and Mach number exactly to satisfy scaling laws [7, 8] in order that measurands from a wind tunnel environment can be converted to actual flight conditions.

### 2.2.1 Linear Aeroelastic Models

As the buffet problem is inherently aeroelastic in nature, its solution depends on the advances in theoretical research in the areas of structural dynamics and unsteady aerodynamics as well as numerical solution schemes associated with computational aeroelasticity. General aeroelastic phenomena were described by Theodorsen [33], Bisplinghoff, Adhley and Halfman [34], and Dowell [35]. A more complete formulation of the general aeroelastic equations was described by Bisplinghoff [36] and Fung [37]. Pines [38] presented physical models of flutter, examined the governing equations in a general sense and established relationships for which flutter can exist.

In the 1960s, only simple computational aeroelastic models, such as a two-dimensional wing mounted on an elastic support or lumped mass structural models with theoretical, or semi-empirical aerodynamics, were applied in aeroelastic design. The first aeroelastic analyses considered incompressible flow and linear springs. Although convenient for their simplicity and minimal computational requirements, they lack the reality of three-dimensional nonlinear flows. Beginning in the 1970s, structural analysis codes based on the Finite Element Method (FEM) initiated the use of aero-structural models by implementing flat plate vortex lattice methods. While this provided for three-dimensional effects, the analysis was restricted to linear aerodynamics, often neglecting thickness effects.

In the early 1980s, a significant advance was made when the analysis was extended to transonic flows. Because transonic flows are described by nonlinear equations, there were methods developed for simultaneous numerical integration of the governing equations for the flow and the dynamic equations of motion of the structure. The first efforts in this pioneering work were by Rizetta [39, 40], Ballhaus and Goorjian [41], Yang, Guruswamy, and Striz [42], Yang, *et al.* [43], and Guruswamy and Yang [44]. Their work was the first to truly capture dynamic/aerodynamic interaction by considering the flowing fluid and airfoil together to be a single dynamic system.

Desmarais and Bennett [45] described an approach for flutter analysis where the generalised mass and mode shapes are determined through the use of an external structural dynamics analysis. These modes describe the shape of the wing and are used to compute an aerodynamic influence matrix. The aerodynamics are modelled using a subsonic kernel function approach. The solution is performed in the frequency domain, and the roots of the eigensolution, which are dependant upon the velocity, density, and Mach number, are used to determine the critical conditions necessary for flutter. The

governing equations are cast in a linear form, and a simple harmonic form of the solution is assumed and application of the method is limited by these assumptions.

Frequency domain solutions are the most widely used since they require less resources and are a more convenient solution scheme. However, a frequency domain solution does not provide a physical description of the motion as do time domain solutions which provide a more general approach, and do not assume a form of the solution, i.e. harmonic motion, as do the frequency domain schemes.

One of the first time domain solutions of the governing aeroelastic equations was developed by Devers [46]. He used a vortex-lattice method as an aerodynamic model. However, simplifications in his model prevented the unsteady nature of trailing edge and wing-tip vortex effects from being considered. In addition, his integration scheme assumed a form of the solution and, consequently, the simulation was limited by this assumption.

In the early 1980s, Guruswamy and Goorjian [47] successfully demonstrated an unsteady transonic small disturbance CFD code that was combined with a modal analysis computational structural dynamics code to calculate the transonic flutter of an unswept rectangular wing which was later extended to include the effects of moving control surfaces.

Batina [48, 49] developed a method that solved the inviscid transonic small disturbance (TSD) equations for use in aeroelastic analysis. This work was undertaken in order to provide an alternative to the widely used linear methods, such as doublet lattice, and to improve upon previous TSD codes. The code developed to solve the TSD equation allowed transonic effects to be determined in flutter calculations. The method was limited to inviscid, irrotational, attached flows and is invalid for the prediction of high angle of attack vortex-induced tail buffet.

Some attention has also been given to the problem of modelling the aeroelastic response of flexible wings. Among the earliest investigators to capture dynamic/aerodynamic interaction by considering the wing and the flowing fluid to be a single dynamic system were Eastep and Olsen [50] and Borland and Rizzetta [51]. These efforts were directed toward transonic flows and used small disturbance models of the flowfield.

## 2.2.2 CFD/CSD Aeroelastic Solvers

By the 1990s advances in aeroelastic CFD and computer speeds led to a more sophisticated analysis tool through the introduction of three-dimensional unsteady CFD solvers combined with a computational structural dynamics (CSD) modal model analysis.

Strganac [52] and Strganac and Mook [53] also analysed the unsteady aeroelastic behaviour of flexible wings. They developed a method for analysing the aeroelastic response of rigid and flexible finite-aspect-ratio wings mounted on elastic supports. The method is based on the general unsteady vortex-lattice method and can accommodate non-linear structural models and small, but finite, amplitudes of motion that make it suitable for limit cycle, *i.e.* post flutter, analyses.

In their approach, Strganac and Mook followed a procedure that was first proposed by Loring [54], who introduced generalised coordinates through the use of the natural modes to solve the flutter problem. They expressed the deflections as expansions in terms of the linear free-vibration modes and considered the time-dependant coefficients in the expansions to be the generalised coordinates of the motion. The aerodynamic loads were also expressed as expansions in the modes. Following Galerkin's procedure, they reduced the original set of governing partial differential equations to a finite set of ordinary differential equations. The governing equations are developed for motion about arbitrary static angles of attack, providing a capability to study the associated nonlinear effects.

The three-dimensional unsteady vortex-lattice method, as used by Strganac and Mook, is able to treat arbitrary manoeuvres of wings of arbitrary planforms, including highly swept delta wings which exhibit leading-edge separation, configurations of multiple closely coupled lifting surfaces, and low aspect ratio planforms. It can also treat arbitrary angles of attack and camber, as long as stall or vortex bursting in the near wake does not occur. The method accurately predicts spanwise distributions of static loads and accounts for the nonlinear effects of the wakes adjoining the tips and trailing edge. Because the governing equations are solved in the time domain, the method provides an opportunity to analyse the results using visualisation of the flowfield and wing motion.

Schuster, *et al.* [55] presented an aeroelastic approach based on a blocked structured Euler/Navier-Stokes CFD method. Since that time, a number of static and dynamic rigid and aeroelastic test cases have been analyzed. The Navier-Stokes solver was coupled with a linear structural modal model to provide static aeroelastic analysis of wings at extreme flight conditions. The method compared well with experimental data and was later extended to enable analysis of more general configurations including vertical tail surfaces.

Guruswamy [56] reported on an Euler CFD based solver coupled with a modal structural model for computing aeroelastic responses of wings. Later he extended the method to include a Navier-Stokes CFD based dynamic aeroelastic analysis capability. The computed results compared well with the available experimental data for steady and unsteady flows. Effects of flexibility, wing sweep angle and pitch rate were included in the prediction of aeroelastic response of a wing-alone configuration.

Kandil, Kandil and Massey [57] presented the first computational simulation of the vertical tail buffet using a delta wing-vertical tail configuration. A 76° swept

sharp-edged delta wing has been used along with a single rectangular vertical tail which was placed aft of the wing along the plane of geometric symmetry. The tail was allowed to oscillate in bending modes. The flow conditions and wing angle of attack have been selected to produce an unsteady vortex-breakdown flow. Unsteady vortex breakdown of leading-edge vortex cores was captured, and unsteady pressure forces were obtained on the tail. Their computational results are in good qualitative agreement with the experimental data of Washburn, Jenkins and Ferman [20].

Kandil, Massey and Sheta [58] studied the effects of coupling and uncoupling the bending and torsional modes and the flow Reynolds number on the buffet response of a single rectangular tail. It has been shown that the coupled response produces higher deflection than that of the uncoupled response. Moreover, the response of the coupled case reaches periodicity faster than that of the uncoupled case. It has also been shown that the deflections of the low-Reynolds number case are substantially lower than those of the high Reynolds number case.

Kandil, Sheta and Massey [59] presented a finite volume CFD-based study including buffet response of the F/A-18 twin tails in a generic delta wing-fin configuration. The leading-edge vortex breakdown flow has been generated using a  $76^\circ$ -swept back sharp-edged delta wing which was pitched at  $32^\circ$  angle of attack. Each of the twin tails was cantilevered at a trailing edge extension of the delta wing. A multi-block grid was used to solve the problem for two lateral locations of the twin tails. Only uncoupled bending-torsion response cases were considered in this study. While validation against experimental data was not reported, the results represent expected trends showing promise for the method.

Computational simulations on the complete F/A-18 geometry for long time histories required for statistical analysis are prohibitively expensive and have been carried out only in large research organisations such as NASA Ames and NASA LaRC where sufficient computing resources are available. One of the first attempts at numerical simulation of the F/A-18 tail buffeting found in the open literature was undertaken by Rizk, *et al.* [60] and Gee, *et al.* [61]. They carried out unsteady flow calculations around the F/A-18 aircraft and also investigated buffeting of the vertical tails at  $M=0.243$  and  $30.3$  degrees angle of attack and compared predictions with wind tunnel tests to show the accuracy of their numerical schemes.

In Rizk, *et al.* [60], the computations were carried out for a rigid vertical tail, so no aerodynamic coupling was taken into account. Also, only a symmetrical configuration was considered. Comparisons with full-scale F/A-18 wind tunnel tests showed rather poor correlation and Gee, *et al.* [61] improved the CFD results using an enhanced grid system. The new grid system contained a finer grid resolution in the fuselage forebody and LEX regions, and included the details of the engine inlet geometry. This led to more accurate prediction of the LEX vortex burst position and improved prediction of the vertical fin unsteady loads.

When compared with experiments, the predictions of Gee, *et al.* [61] were found to be quite good in some of the pressure results, but were poor in the fin root bending moment and peak power coefficients. Inclusion of the aeroelastic deformation in the numerical simulations is necessary to improve the predictions, as the structural-induced aerodynamic loads can be significant at higher dynamic pressures. This requires simultaneous solutions of the aerodynamic loads and structural response of the vertical tail so that the interaction at each time step can be accounted for.

The most rigorous attempt to computationally simulate the F/A-18 vertical fin buffeting was undertaken by Findlay [62]. He used a tightly coupled dynamic aeroelastic analysis to predict empennage buffet at 30 degrees angle of attack. The method employs the solution of the time-dependent Navier-Stokes equations to describe the unsteady flowfield and a structural dynamics modal analysis to compute response of the structure. The model was employed to perform a computational study of steady and unsteady calculations of the F/A-18 aircraft with rigid and flexible tails.

The results of Findlay showed reasonable agreement with in-flight, and full-scale wind tunnel test measured trends. However, the absolute magnitudes of buffet loads and dominant frequencies of the buffet pressures were under-predicted. This is primarily attributed to insufficient grid resolution, as increases in flowfield field fidelity showed improvements in surface pressures for steady-state calculations. However, as reported in [62], computational requirements, expected to be adequate for unsteady calculations with a grid of sufficient fidelity were beyond the resources available.

As reported by Findlay, the effect of flexibility of the tail showed a decrease in buffet pressure magnitude from the values for the rigid calculations which is consistent with experimental results. The difference in the two values compared well with measured differences between rigid and flexible model tests. This is an important finding as buffet is often assumed to be independent of tail response when computing unsteady aerodynamic loads. Thus, rigid computations usually over-predict the flight data and comparison between rigid computations and flexible flight test data could be misleading.

### 3. Structural Dynamic Model

A general approach to the computation of the response of a structure to dynamic loads is provided by energy methods, see Meirovitch [63]. In such methods, the solution is derived by describing the dynamic response in terms of small displacements about equilibrium points.

### 3.1 Governing Equations of Motion

The equation governing the motion of the dynamical system representing the vertical tail can be obtained by Hamilton's principle [63], which can be stated in the form

$$\int_0^t \int_0^L (\partial E_K - \partial E_P + \partial W_A) dl dt = 0 \quad (1)$$

where  $E_K$  and  $E_P$  are kinetic and potential energy of the system,  $W_A$  is the work performed by the aerodynamic loading and  $L$  is the vertical tail length.

To facilitate the development of the approach, the vertical tail can be represented as a flexible cantilevered beam with rigidly fixed root and rigid cross-section. The tail bending  $Y$  and torsional  $\theta$  deflections occur about an elastic axis that is not necessary coincident with the inertial axis. If spanwise motion is ignored, then components of the velocity of the beam centre of gravity can be described in the inertial frame as

$$V_x = -x_0(\mathbf{z}) \sin(\theta(\mathbf{z}, t)) \frac{\partial \theta(\mathbf{z}, t)}{\partial t}, \quad (2)$$

and

$$V_y = \frac{\partial Y(\mathbf{z}, t)}{\partial t} + x_0(\mathbf{z}) \cos(\theta(\mathbf{z}, t)) \frac{\partial \theta(\mathbf{z}, t)}{\partial t}, \quad (3)$$

where  $\mathbf{z}$  axis of the frame coincides with the tail elastic axis and measures the vertical distance from the fixed support along the tail length while  $\mathbf{x}$  axis is placed in the vertical tail plane and  $x_0(\mathbf{z}) = x_{CG}(\mathbf{z}) - x_e(\mathbf{z})$  is the distance between the elastic axis and inertial axis.

Thus, the kinetic and potential energy of the system can be expressed as

$$E_K = \int_0^L \frac{1}{2} \left\{ m(\mathbf{z}) \left[ \left( \frac{\partial Y(\mathbf{z}, t)}{\partial t} + x_0(\mathbf{z}) \cos(\theta(\mathbf{z}, t)) \frac{\partial \theta(\mathbf{z}, t)}{\partial t} \right)^2 + \left( x_0(\mathbf{z}) \sin(\theta(\mathbf{z}, t)) \frac{\partial \theta(\mathbf{z}, t)}{\partial t} \right)^2 \right] + I_{CG}(\mathbf{z}) \left( \frac{\partial \theta(\mathbf{z}, t)}{\partial t} \right)^2 \right\} d\mathbf{z}, \quad (4)$$

and

$$E_P = \int_0^L \frac{1}{2} \left\{ EI(\mathbf{z}) \left( \frac{\partial^2 Y(\mathbf{z}, t)}{\partial \mathbf{z}^2} \right)^2 + GJ(\mathbf{z}) \left( \frac{\partial \theta(\mathbf{z}, t)}{\partial \mathbf{z}} \right)^2 - m(\mathbf{z}) g (Y(\mathbf{z}, t) + x_0(\mathbf{z}) \sin(\theta(\mathbf{z}, t))) \cos \beta \right\} d\mathbf{z}, \quad (5)$$



accordingly, while the work performed by the aerodynamic loading can be expressed as

$$W_A = \int_0^L \{N(\mathbf{z}, t)Y(\mathbf{z}, t) + M(\mathbf{z}, t)\theta(\mathbf{z}, t)\} d\mathbf{z} \quad (6)$$

where:  $El(\mathbf{z})$  and  $GJ(\mathbf{z})$  are the bending and torsional stiffness of the tail section,

$g$  is the acceleration due to gravity,

$\beta$  is the angle between vertical tail and delta wing plane,

$m(\mathbf{z})$  is the mass per unit length,

$I_{CG}(\mathbf{z})$  is the mass moment of inertia per unit length about the centre of gravity,

$N(\mathbf{z})$  is the normal force per unit length,

$M(\mathbf{z})$  is the torsional moment per unit length.

Introducing Equations (4)-(6) into Equation (1), the following differential equations of motion can be obtained:

$$\begin{aligned} m(\mathbf{z}) \frac{\partial^2 Y(\mathbf{z}, t)}{\partial t^2} + m(\mathbf{z}) x_0(\mathbf{z}) \cos(\theta(\mathbf{z}, t)) \frac{\partial^2 \theta(\mathbf{z}, t)}{\partial t^2} - m(\mathbf{z}) x_0(\mathbf{z}) \sin(\theta(\mathbf{z}, t)) \left( \frac{\partial \theta(\mathbf{z}, t)}{\partial t} \right)^2 \\ + \frac{\partial^2}{\partial \mathbf{z}^2} \left( El(\mathbf{z}) \frac{\partial^2 Y(\mathbf{z}, t)}{\partial \mathbf{z}^2} \right) - m(\mathbf{z}) g \cos \beta = N(\mathbf{z}, t) \end{aligned} \quad (7)$$

$$\begin{aligned} I_0(\mathbf{z}) \frac{\partial \theta(\mathbf{z}, t)}{\partial t} + m(\mathbf{z}) x_0(\mathbf{z}) \cos(\theta(\mathbf{z}, t)) \frac{\partial^2 Y(\mathbf{z}, t)}{\partial t^2} - \frac{\partial}{\partial \mathbf{z}} \left( GJ(\mathbf{z}) \frac{\partial \theta(\mathbf{z}, t)}{\partial \mathbf{z}} \right) \\ - m(\mathbf{z}) g x_0(\mathbf{z}) \cos(\theta(\mathbf{z}, t)) \cos \beta = M(\mathbf{z}, t) \end{aligned} \quad (8)$$

The initial assumption of small motion about an equilibrium point allows for the above equations of motion to be presented in linear form as:

$$m(\mathbf{z}) \frac{\partial^2 Y(\mathbf{z}, t)}{\partial t^2} + m(\mathbf{z}) x_0(\mathbf{z}) \frac{\partial^2 \theta(\mathbf{z}, t)}{\partial t^2} + \frac{\partial^2}{\partial \mathbf{z}^2} \left( El(\mathbf{z}) \frac{\partial^2 Y(\mathbf{z}, t)}{\partial \mathbf{z}^2} \right) - m(\mathbf{z}) g \cos \beta = N(\mathbf{z}, t) \quad (9)$$

$$I_0(\mathbf{z}) \frac{\partial \theta(\mathbf{z}, t)}{\partial t} + m(\mathbf{z}) x_0(\mathbf{z}) \frac{\partial^2 Y(\mathbf{z}, t)}{\partial t^2} - \frac{\partial}{\partial \mathbf{z}} \left( GJ(\mathbf{z}) \frac{\partial \theta(\mathbf{z}, t)}{\partial \mathbf{z}} \right) - m(\mathbf{z}) x_0(\mathbf{z}) g \cos \beta = M(\mathbf{z}, t) \quad (10)$$

For a flexible vertical tail represented as a cantilevered beam with rigidly fixed root, the geometrical and natural boundary conditions on  $Y$  and  $\theta$  are given as:

$$Y(0,t) = \frac{\partial Y(0,t)}{\partial t} = \frac{\partial^2 Y(L,t)}{\partial \mathbf{z}^2} = \frac{\partial}{\partial \mathbf{z}} \left[ EI(L) \frac{\partial^2 Y(L,t)}{\partial \mathbf{z}^2} \right] = 0, \quad (11)$$

and

$$\theta(0,t) = \frac{\partial \theta(L,t)}{\partial \mathbf{z}} = 0 \quad (12)$$

The solution of Equations (9) and (10) with the above boundary conditions provides the total response of a dynamic system to an unsteady aerodynamic loading.

Following Strganac [52], the system's total response can be represented in terms of the static and dynamic solutions as

$$Y(\mathbf{z},t) = Y_s(\mathbf{z}) + Y_d(\mathbf{z},t), \quad (13)$$

and

$$\theta(\mathbf{z},t) = \theta_s(\mathbf{z}) + \theta_d(\mathbf{z},t). \quad (14)$$

In case of decaying motions the solution of the Equations (9) and (10) will converge to the static solution and may not require unnecessary computation of the dynamic contributions. Also, for the case of large static deformations, the solutions of the dynamical equations about the static deformations will conform to the original assumption of small motions about an equilibrium points. Therefore, the Equations (9) and (10) can be presented in terms of the static and dynamic contributions as

$$\begin{aligned} m(\mathbf{z}) \frac{\partial^2 Y_d(\mathbf{z},t)}{\partial t^2} + m(\mathbf{z}) x_0(\mathbf{z}) \frac{\partial^2 \theta_d(\mathbf{z},t)}{\partial t^2} + \frac{\partial^2}{\partial \mathbf{z}^2} \left( EI(\mathbf{z}) \frac{\partial^2 Y_s(\mathbf{z})}{\partial \mathbf{z}^2} \right) \\ + \frac{\partial^2}{\partial \mathbf{z}^2} \left( EI(\mathbf{z}) \frac{\partial^2 Y_d(\mathbf{z},t)}{\partial \mathbf{z}^2} \right) - m(\mathbf{z}) g \cos \beta = N_s(\mathbf{z}) + N_d(\mathbf{z},t), \end{aligned} \quad (15)$$

and

$$\begin{aligned} I_0(\mathbf{z}) \frac{\partial \theta_d(\mathbf{z},t)}{\partial t} + m(\mathbf{z}) x_0(\mathbf{z}) \frac{\partial^2 Y_d(\mathbf{z},t)}{\partial t^2} - \frac{\partial}{\partial \mathbf{z}} \left( GJ(\mathbf{z}) \frac{\partial \theta_s(\mathbf{z})}{\partial \mathbf{z}} \right) \\ - \frac{\partial}{\partial \mathbf{z}} \left( GJ(\mathbf{z}) \frac{\partial \theta_d(\mathbf{z},t)}{\partial \mathbf{z}} \right) - m(\mathbf{z}) g x_0(\mathbf{z}) \cos \beta = M_s(\mathbf{z}) + M_d(\mathbf{z},t). \end{aligned} \quad (16)$$

Here, the equations for the static deformations can be written as

$$\frac{\partial^2}{\partial \mathbf{z}^2} \left( EI(\mathbf{z}) \frac{\partial^2 Y_s(\mathbf{z})}{\partial \mathbf{z}^2} \right) - m(\mathbf{z}) g \cos \beta = N_s(\mathbf{z}), \quad (17)$$

$$- \frac{\partial}{\partial \mathbf{z}} \left( GJ(\mathbf{z}) \frac{\partial \theta_s(\mathbf{z})}{\partial \mathbf{z}} \right) - m(\mathbf{z}) x_0(\mathbf{z}) g \cos \beta = M_s(\mathbf{z}), \quad (18)$$

and the dynamic equations for small motion about the static deformations can be presented as

$$m(\mathbf{z}) \frac{\partial^2 Y_d(\mathbf{z}, t)}{\partial t^2} + m(\mathbf{z}) x_\theta(\mathbf{z}) \frac{\partial^2 \theta_d(\mathbf{z}, t)}{\partial t^2} + \frac{\partial^2}{\partial \mathbf{z}^2} \left( EI(\mathbf{z}) \frac{\partial^2 Y_d(\mathbf{z}, t)}{\partial \mathbf{z}^2} \right) = N_d(\mathbf{z}, t), \quad (19)$$

$$I_\theta(\mathbf{z}) \frac{\partial \theta_d(\mathbf{z}, t)}{\partial t} + m(\mathbf{z}) x_\theta(\mathbf{z}) \frac{\partial^2 Y_d(\mathbf{z}, t)}{\partial t^2} - \frac{\partial}{\partial \mathbf{z}} \left( GJ(\mathbf{z}) \frac{\partial \theta_d(\mathbf{z}, t)}{\partial \mathbf{z}} \right) = M_d(\mathbf{z}, t). \quad (20)$$

A solution of the above equations can be obtained by an expansion of the dependent variables in terms of the natural free vibration modes of the system, see Meirovitch [63]. Here, the variables  $Y_d$  and  $\theta_d$  can be represented as

$$Y_d(\mathbf{z}, t) = \sum_{i=1}^I \psi_i(\mathbf{z}) q_i(t), \quad (21)$$

and

$$\theta_d(\mathbf{z}, t) = \sum_{j=I+1}^J \psi_j(\mathbf{z}) q_j(t), \quad (22)$$

where  $\psi_i$  and  $\psi_j$  are modeshapes satisfying the free-vibration modes of bending and torsion,

$q_i$  and  $q_j$  are generalised coordinates for bending and torsion modes,

$I$  is the number of bending modes,

$(J-I)$  is the number of torsion modes selected to represent the solution.

Substituting these expansions into Equations (15) and (16) and using the Galerkin method along with integration by parts and imposing the boundary conditions, Equations (11) and (12), one can get the following equations for the generalised coordinates  $q_i$  and  $q_j$  in matrix form:

$$\begin{bmatrix} K_{11} & K_{12} \\ K_{21} & K_{22} \end{bmatrix} \begin{pmatrix} q_i \\ q_j \end{pmatrix}_s = \begin{pmatrix} A_{si} + F_i \\ A_{sj} + F_j \end{pmatrix}, \quad (23)$$

$$\begin{bmatrix} M_{11} & M_{12} \\ M_{21} & M_{22} \end{bmatrix} \begin{pmatrix} \frac{\partial^2 q_i}{\partial t^2} \\ \frac{\partial^2 q_j}{\partial t^2} \end{pmatrix}_d + \begin{bmatrix} K_{11} & K_{12} \\ K_{21} & K_{22} \end{bmatrix} \begin{pmatrix} q_i \\ q_j \end{pmatrix}_d = \begin{pmatrix} A_{di} \\ A_{dj} \end{pmatrix}, \quad (24)$$

where

$[K]$  is the stiffness matrix,

$[M]$  is the mass matrix,

$(A_s)$  is the static component of aerodynamic loading vector,

$(A_d)$  is the dynamic component of aerodynamic loading vector,

$(F)$  is the static loading vector due to gravity,

and

$$\begin{aligned}
 K_{11} &= \int_0^L EI(\mathbf{z}) \frac{\partial^2 \psi_i}{\partial \mathbf{z}^2} \frac{\partial^2 \psi_j}{\partial \mathbf{z}^2} d\mathbf{z} && \text{for } i = 1, 2, \dots, I \text{ and } j = 1, 2, \dots, I \\
 K_{12} &= K_{21} = 0 \\
 K_{22} &= \int_0^L GJ(\mathbf{z}) \frac{\partial \psi_i}{\partial \mathbf{z}} \frac{\partial \psi_j}{\partial \mathbf{z}} d\mathbf{z} && \text{for } i = I + 1, \dots, J \text{ and } j = I + 1, \dots, J \\
 M_{11} &= \int_0^L m(\mathbf{z}) \psi_i \psi_j d\mathbf{z} && \text{for } i = 1, 2, \dots, I \text{ and } j = 1, 2, \dots, I \\
 M_{12} &= M_{21} = \int_0^L m(\mathbf{z}) x_0(\mathbf{z}) \psi_i \psi_j d\mathbf{z} && \text{for } i = 1, 2, \dots, I \text{ and } j = I + 1, \dots, J \\
 M_{22} &= \int_0^L I_0(\mathbf{z}) \psi_i \psi_j d\mathbf{z} && \text{for } i = I + 1, \dots, J \text{ and } j = I + 1, \dots, J \\
 A_{si} &= \int_0^L \psi_i N_s(\mathbf{z}) d\mathbf{z} && \text{for } i = 1, 2, \dots, I \\
 A_{sj} &= \int_0^L \psi_j M_s(\mathbf{z}) d\mathbf{z} && \text{for } j = I + 1, \dots, J \\
 A_{di} &= \int_0^L \psi_i N_d(\mathbf{z}, t) d\mathbf{z} && \text{for } i = 1, 2, \dots, I \\
 A_{dj} &= \int_0^L \psi_j M_d(\mathbf{z}, t) d\mathbf{z} && \text{for } j = I + 1, \dots, J \\
 F_i &= \int_0^L \psi_i m(\mathbf{z}) g d\mathbf{z} && \text{for } i = 1, 2, \dots, I \\
 F_j &= \int_0^L \psi_j m(\mathbf{z}) g x_0(\mathbf{z}) d\mathbf{z} && \text{for } j = I + 1, \dots, J
 \end{aligned}$$

which are similar to those developed by Strganac [52]. Note, that the above equations of motion are coupled both inertially and aerodynamically, as the sectional center of gravity and elastic axis are not generally coincident and the aerodynamic loads are motion dependent.

## 4. Unsteady Aerodynamic Model

The equations of motion (23, 24) describing dynamic response of the system require an aerodynamic model that is able to predict unsteady buffet loads on a vertical tail simultaneously with the motion. Although Euler or Navier-Stokes codes can be applied for the simulation of unsteady flows over delta wings, the limitation of the available computational resources calls for more economical methods when it comes to such computationally intensive problems as time-accurate prediction of empennage buffet. Therefore, a vortex approach is used for the development of an unsteady aerodynamic model that provides economy in computation by focusing the computational effort on the areas of concentrated vorticity.

### 4.1 Overview of Vortex Method

Vortex methods simulate the unsteady fluid flows under the assumption of nonlinear dynamics of vorticity, so fluid flows at high Reynolds numbers can be simulated by regions of concentrated vorticity embedded in irrotational fluid. The evolution of vortex elements can be tracked numerically in a Lagrangian or hybrid Euler-Lagrangian reference frame. As stated by the theorems of Helmholtz and Kelvin, the inviscid motion of vorticity in these regions is provided by the local fluid velocity, which in turn is determined kinematically from the vorticity field. Thus, it is very convenient to consider inviscid fluid dynamics in terms of concentrated vorticity regions, which induce motion on each other as an alternative to pressure-velocity considerations.

Over the past decades, vortex methods have been developed and applied as a reliable predictive tool for a wide range of engineering problems. Their area of application has extended from simple inviscid potential flow calculations to the modelling of unsteady viscous flows by simulating the three-dimensional Navier-Stokes equations. This ability of vortex methods to account for the complex features of fluid dynamics from within a single computational framework makes them a very attractive tool for a wide range of engineering problems.

It was shown by Levinski [64, 65], that the vortex model is able to predict the onset of leading edge vortex breakdown past a delta wing, twin-tail configuration and qualitatively describe its unsteady behaviour. Also, spatial and temporal characteristics of unsteady buffet pressures arising on the rigid tail were found to be in qualitative agreement with available experimental data. A detailed description of the unsteady vortex method can be found in Levinski [65] and only a brief review of the technique is provided here.

## 4.2 Governing Equations

Fluid flows are governed by the Navier-Stokes equations, which for incompressible viscous fluid flow may be expressed as

$$\frac{\partial \mathbf{u}}{\partial t} + (\mathbf{u} \cdot \nabla) \mathbf{u} = -\frac{\nabla p}{\rho} + \nu \nabla^2 \mathbf{u}, \quad (25)$$

$$\nabla \cdot \mathbf{u} = 0, \quad (26)$$

where  $\mathbf{u}$  is a flow velocity,  
 $p$  is a pressure,  
 $\rho$  is the fluid density,  
 $\nu$  is a flow viscosity.

In homogeneous fluids, vorticity  $\boldsymbol{\omega}$  is defined as

$$\boldsymbol{\omega} = \nabla \times \mathbf{u}. \quad (27)$$

Then in terms of vorticity, Equation (25) can be written as

$$\frac{\partial \boldsymbol{\omega}}{\partial t} + (\mathbf{u} \cdot \nabla) \boldsymbol{\omega} = \boldsymbol{\omega} \cdot \nabla \mathbf{u} + \nu \nabla^2 \boldsymbol{\omega}, \quad (28)$$

which is the vorticity transport equation and represents simultaneous convection and diffusion of vorticity in the flow field as well as concentration of vorticity due to vortex filament stretching. The solution can be obtained using the widely adopted fractional step method, which simulates the convection and the diffusion processes sequentially rather than simultaneously, see Leonard [66]. This can be achieved by solving Euler's equations by the vortex method and using the proper numerical technique to model the diffusion equation. The required local velocities can be computed as the solution of Poisson's equation for the velocity field in terms of Biot-Savart integration.

### 4.2.1 Vorticity Production and Convection

In a real flow, the well-known viscous boundary layer, caused by the presence of viscosity, develops adjacent to the body surface. The essence of the majority of vortex methods is to replace this boundary layer by a region of concentrated vorticity, which causes a reduction in the fluid velocity from its local value to zero right on the body surface. For computational simplicity the real fluid flow can be represented as a bulk of irrotational inviscid outer flow separated from the actual body surface by the thin boundary shear layer, where the effects of viscosity and turbulence are simulated.

For very high Reynolds number flows the fluid can be considered as inviscid and the boundary layer cannot be developed on the body surface. In such flows the fluid velocity changes discontinuously from zero at the point that belongs to the body

surface up to the value of local flow velocity just above it. In this case, the body surface itself must be represented as the distributed vorticity sheet  $\sigma$  of strength  $\gamma$  and the boundary condition of zero normal velocity is used to ensure 'no-leak' velocity through the body surface.

It can be shown that the rate of vorticity production in the shear layer is directly related to the pressure gradient [66], so vorticity creation is largely attributable to the dynamic behaviour of the outer flow. Here, a statement of the Neumann boundary condition of 'no-leak' velocity at a point  $\kappa$  on a body surface  $\sigma$  may be expressed by the following integral equation

$$-\frac{1}{4\pi} \int_{\sigma} Q(\kappa, \mu) \gamma(\mu) d\sigma_{\mu} \times \mathbf{n}_{\kappa} + f_n(\mathbf{n}_{\kappa}, \mathbf{V}_{\infty}) = 0, \quad (29)$$

where  $\mathbf{n}_{\kappa}$  is a unit normal vector at point  $\kappa$ .  
 $\mu$  is a variable point on a body surface  $\sigma$ ,  
 $Q$  is a velocity singular kernel,  
 $f_n$  is a function of surface geometry and outer flow velocity.

The integral equation (29) describes the process of vorticity creation on the solid boundaries and can be used to define the distribution of vorticity over the body surface. It states that the local vorticity density  $\gamma(\mu)$  must be such that, in the presence of an incident flow velocity  $\mathbf{V}_{\infty}$ , the resultant flow remains parallel to the body surface.

A natural consequence of the process of vorticity production and convection along the body surface is its shedding from certain separation points into the flow field. Although in a real flow the viscous boundary layer may separate spontaneously under various conditions, the assumption of a fully attached boundary layer is commonly used in inviscid potential flow calculations. In such an approach the flow is allowed to separate only at a finite number of prescribed separation points, such as the body trailing edge, in order to satisfy the unsteady Kutta-Joukowski condition, see Belotserkovskii and Nisht [67].

The equations of motion of separated vortices are given by the value of the velocity field at their present locations

$$\frac{d\mathbf{r}_i}{dt} = \mathbf{u}(\mathbf{r}_i, t). \quad (30)$$

The spatial evolution of the flowfield can be obtained by integrating the above equation using the Adams-Bashford scheme, which is recommended for vortex methods [66].

The required local velocities can be computed as the solution of Poisson's equation for the velocity field

$$\nabla^2 \mathbf{u} = -\nabla \times \boldsymbol{\omega}. \quad (31)$$

For a flow field without interior boundaries and with the fluid at rest at infinity, the solution to Poisson's equation (31) may be written as the Biot-Savart integral equation, which gives a velocity distribution induced by an area of concentrated vorticity, see Lamb [68]. Hence, one can get a nonlinear system of ordinary differential equations giving the temporal evolution of the vorticity field.

#### 4.2.2 Discretisation of Vorticity Regions

According to the vortex method, the compact vorticity regions can be confined to a finite number of isolated tubes of vorticity or vortex filaments. Similar to the point vortex representation in two-dimensional vortex flows, these flows in three-dimensional coordinates can be modelled by a system of space curves, each with zero cross-sectional area and constant circulation.

Although the vortex filaments with an infinitesimal core is the simplest method for vorticity discretisation, many investigators have used vortices with cores of constant and finite shape or vortex 'blobs', see for example Chorin [69] or Kuwahara & Takami [70]. In the vortex blob method, the vortex core has a constant axisymmetrical shape which is defined by a 'cut-off' radius and a 'cut-off' function to yield a description of vorticity distribution within the core. Thus, if the spatial configuration of the vortex filament with a blob-like core is defined by space curve  $\mathbf{r}_i(s, t)$ , then its vorticity field is given by

$$\boldsymbol{\omega}_i(\mathbf{r}, t) = \Gamma_i \int f_\sigma [\mathbf{r} - \mathbf{r}_i(s, t)] \frac{\partial \mathbf{r}_i}{\partial s} ds. \quad (32)$$

where  $s$  is a parameter along the curve,  
 $f_\sigma$  is a cut-off function,  
 $\Gamma_i$  is a vortex filament circulation.

Following Leonard [71], the velocity field induced by this filament in an unbounded domain, with no interior boundaries, can be determined as

$$\mathbf{u}_i(\mathbf{r}, t) = -\frac{1}{4\pi} \Gamma_i \int \frac{[\mathbf{r} - \mathbf{r}_i(s, t)] \times \frac{\partial \mathbf{r}_i}{\partial s} \xi(|\mathbf{r} - \mathbf{r}_i(s, t)|/\delta_i)}{|\mathbf{r} - \mathbf{r}_i(s, t)|^3} ds, \quad (33)$$

where smoothing function  $\xi$  is determined by the choice of 'cut-off' function. In the current study, the curvilinear vortex filament of arbitrary shape is represented as a combination of rectilinear vortex filaments of constant strength.



The use of distributed vortex cores or vortex blobs yields more realistic vorticity distributions and bounded induced velocities compared to the vortex filaments with infinitesimal cores [69]. It can be shown that the vortex blob calculation scheme satisfies the principles of conservation of circulation, of impulse and momentum of impulse for the system of vortices with the same core sizes, see Leonard [71].

Despite certain advantages of the high-order explicit cut-off functions, a simpler function of vorticity distribution within the core as proposed by Rosenhead [72] is adopted in the present study. The core radius is assumed to be time invariant and similar for all the vortex elements. Such a scheme was found to be adequate for accurate representation of the velocity field modelled by well-spaced vortex filaments with low rate of adjacent cores overlapping.

### 4.3 Computational Algorithm

To derive a solution for the unsteady aerodynamic problem the general approach needs to be formulated with appropriate initial and boundary conditions as well as conditions of spatial and temporal discretisation of the body and its wake. A numerical solution is developed in the following sections by the author where the vortex filament method is used to describe inviscid, incompressible flow aerodynamics. The solution is derived using the fractional step method, which provides a sequential simulation of the physical processes of vorticity development and evolution in the flow field.

#### 4.3.1 Formulation of the Unsteady Problem

Consider a lifting body  $\sigma$ , undergoing an arbitrary motion in an infinite space of homogeneous incompressible fluid. As the governing equations of motion are developed in terms of a translating, but non-rotating, reference frame, then it is appropriate to define the unsteady flow problem in the body-fixed coordinate system that is aligned with the vertical tail root and has linear velocity  $\mathbf{U}_0(t)$  with respect to the fixed inertial frame.

In the general case the body motion can be described by its linear velocity  $\mathbf{U}(\mathbf{r}, t)$  and angular velocity  $\Omega(\mathbf{r}, t)$  with respect to the body-fixed reference frame. Therefore, the resulting velocity at a point on a body surface  $\sigma$  can be defined as

$$\mathbf{W}(\mathbf{r}_\sigma, t) = \mathbf{V}(\mathbf{r}, t) + \mathbf{U}_0(t) + \mathbf{U}(\mathbf{r}_\sigma, t) + \Omega(\mathbf{r}_\sigma, t) \times \mathbf{r}_\sigma, \quad (34)$$

where  $\mathbf{V}(\mathbf{r}, t)$  is the velocity field, induced by the body and its wake.

Here, the unknown velocity field  $\mathbf{V}(\mathbf{r}, t)$  in the fluid domain must satisfy the Navier-Stokes equation

$$\frac{\partial \mathbf{V}(\mathbf{r}, t)}{\partial t} + (\mathbf{V}(\mathbf{r}, t) \cdot \nabla) \mathbf{V}(\mathbf{r}, t) = -\frac{1}{\rho} \nabla p(\mathbf{r}, t) + \nu \nabla^2 \mathbf{V}(\mathbf{r}, t), \quad (35)$$

as well as the continuity equation

$$\nabla \cdot \mathbf{V}(\mathbf{r}, t) = 0. \quad (36)$$

It is known that for high Reynolds number flows convective processes in the wake dominate, and the influence of viscous diffusion is minimal. For such flows with negligibly small viscosity, the assumption of fully inviscid flow can be justified and adopted. In this case, the original equation (35) in the inviscid fluid domain can be reduced to Euler's equation for the unknown velocity field  $\mathbf{V}(\mathbf{r}, t)$

$$\frac{\partial \mathbf{V}(\mathbf{r}, t)}{\partial t} + (\mathbf{V}(\mathbf{r}, t) \cdot \nabla) \mathbf{V}(\mathbf{r}, t) = -\frac{1}{\rho} \nabla p(\mathbf{r}, t). \quad (37)$$

The induced velocity field  $\mathbf{V}(\mathbf{r}, t)$  can be assumed to be irrotational in the whole fluid domain except the body surface  $\sigma$  and its trailing wake  $\sigma_p$  i.e.,

$$\nabla \times \mathbf{V}(\mathbf{r}, t) = 0, \quad \mathbf{r} \notin \sigma \cup \left( \sum \sigma_p \right). \quad (38)$$

Then for the induced velocity field a velocity potential  $\Phi$  exists such that

$$\mathbf{V}(\mathbf{r}, t) = \nabla \Phi(\mathbf{r}, t). \quad (39)$$

Therefore, according to Equations (36) and (39) the unknown induced velocity field can be found as a solution to Laplace's equation

$$\Delta \Phi(\mathbf{r}, t) = 0, \quad \mathbf{r} \notin \sigma \cup \left( \sum \sigma_p \right). \quad (40)$$

The fundamental objective of such a problem is to find the velocity potential  $\Phi(\mathbf{r}, t)$  that satisfies Laplace's equation. Under the above initial and boundary conditions, the problem has a unique solution, which gives us the unknown velocity potential  $\Phi(\mathbf{r}, t)$  in the fluid domain [68]. It is also known from Lamb [68], that the solution for Laplace's equation can be obtained by a suitable choice of basic singularities such as doublets, sources or vortices. In fact, no one among these singularities has a special advantage over the others, as the potential flow can be modelled correctly by an appropriate distribution of either sources or vortices. This is guaranteed by the uniqueness theorems for Laplace's equation. But the numerical solution can be formulated at different levels of accuracy and computational efficiency. Therefore, it is particularly advantageous to consider the flow

simulation method, based on vortex singularities, because such important physical processes as flow separation from the body surface as well as unsteady wake development and their interaction, can be modelled using a single approach.

### 4.3.2 Representation of the Body and its Wake

Following vortex theory, a body surface and its wake can be replaced by infinitely thin layers of vorticity or vortex sheets consisting of spanwise and chordwise vortex lines of variable strength. Here, the presence of spanwise vorticity in a body vortex system is caused by a continuous change of the boundary condition at the wall brought about by the flow unsteadiness. The unsteadiness of the boundary conditions is also responsible for the presence of spanwise vorticity in a continuous vortex wake separating from the body surface. In the process of spatial discretisation of the continuous vorticity layer, the curvilinear vortex lines of variable intensity can be represented as a system of rectilinear chordwise and spanwise vortex filaments of constant strengths.

In the current numerical scheme the boundary layer is allowed to separate only at a finite number of separation points, assuming potential flow modelling for the rest of the body. Here, the vorticity diffusion and convection activities within the body boundary layer are completely ignored, thereby substantially reducing the computational effort. It is assumed that the places of separation are known *a priori* and fixed at sharp edges of the body surface. Such an approximation, as well as the assumption of fully attached flow on the rest of the body surface, is commonly used in inviscid flow calculations. Following this simplified technique a reasonably accurate prediction of overall aerodynamic characteristic may be obtained especially for sharp edged bluff bodies.

### 4.3.3 Initial and Boundary Conditions

As the process of flow development will be considered from the time  $t = 0$ , it is assumed that during the period of time  $t \leq 0$  the fluid in the domain and the lifting body itself are in a state of rest. Then for  $t > 0$  both the flow and the body are suddenly set in motion. According to vortex theory, the body unsteady motion will be accompanied by the development of its trailing wake which can be represented as a combination of vortex wake sheets  $\sigma_p$ . Therefore, the unknown velocity field  $\mathbf{V}(\mathbf{r}, t)$  in Equation (35) must satisfy the initial condition

$$\mathbf{V}(\mathbf{r}, t) = 0, \quad \mathbf{W}(\mathbf{r}, t) = 0, \quad t \leq 0, \quad (41)$$

as well as the following boundary conditions:

1. For inviscid flow a statement of the Neumann boundary condition of 'no-leak' velocity at any point on a body surface  $\sigma$  can be written as

$$\mathbf{W}(\mathbf{r}_\sigma, t) \cdot \mathbf{n}(\mathbf{r}_\sigma, t) = 0, \quad (42)$$

where  $\mathbf{n}(\mathbf{r}_\sigma, t)$  is a unit normal vector to the body surface at  $\mathbf{r}_\sigma$ .

2. At an infinite distance from the body and its wake, the condition of induced velocities decay must be satisfied as

$$\lim_{\mathbf{r} \rightarrow \infty} \mathbf{V}(\mathbf{r}, t) = 0. \quad (43)$$

This condition is satisfied identically through the Bio-Savart Law.

3. The Kutta-Joukowski condition of finite velocities must be satisfied at the lines  $p$  of trailing wake separation such that

$$\mathbf{W}(\mathbf{r}_p, t) \neq \infty. \quad (44)$$

As a consequence of the Kutta-Joukowski condition, a vortex wake will be created at the points of flow separation. The kinematic condition of normal velocity continuity

$$\mathbf{W}_i(\mathbf{r}_{\sigma_p}, t) \cdot \mathbf{n}_i(\mathbf{r}_{\sigma_p}, t) = \mathbf{W}_j(\mathbf{r}_{\sigma_p}, t) \cdot \mathbf{n}_j(\mathbf{r}_{\sigma_p}, t), \quad (45)$$

as well as pressure continuity

$$p_i(\mathbf{r}_{\sigma_p}, t) = p_j(\mathbf{r}_{\sigma_p}, t), \quad (46)$$

must be imposed on the upper  $i$  and lower  $j$  surfaces of the vortex wake sheet  $\sigma_p$ . Following the Kelvin-Helmholtz theorem, this kinematic condition is satisfied by allowing the trailing wake to move with the local fluid velocity while preserving its circulation, see Lamb [68].

#### 4.3.4 Calculation of the Pressure Distribution

Having obtained the induced velocity potential  $\Phi(\mathbf{r}, t)$  from the solution of Equation (40), the unsteady velocity field  $\mathbf{W}(\mathbf{r}, t)$  can be determined. The unsteady pressure field in the inertial frame can be calculated using the Cauchy-Lagrange equation [67] for inviscid incompressible flow as

$$P(\mathbf{r}, t) = f_p(t) - \rho \left[ \frac{\partial \Phi(\mathbf{r}, t)}{\partial t} + \frac{\mathbf{V}^2(\mathbf{r}, t)}{2} \right], \quad (47)$$

where the pressure function  $f_p(t)$  can be determined from the boundary condition at infinity. Thus, if the induced velocities decay at infinite distance from the body and its wake, so that

$$\Phi(\mathbf{r}, t) \rightarrow 0, \quad |\nabla \Phi(\mathbf{r}, t)| \rightarrow 0, \quad (48)$$

and assuming constant pressure at infinity, one can get

$$P(\mathbf{r}, t) = P_\infty - \rho \left[ \frac{\partial \Phi(\mathbf{r}, t)}{\partial t} + \frac{\mathbf{V}^2(\mathbf{r}, t)}{2} \right]. \quad (49)$$

Therefore, an unsteady pressure coefficient on the body surface  $\sigma$  can be defined as

$$C_p(\mathbf{r}, t) = \frac{P(\mathbf{r}, t) - P_\infty}{\rho U_0^2 / 2} = 1 - w^2(\mathbf{r}, t) - 2 \frac{\partial \phi(\mathbf{r}, t)}{\partial t}, \quad (50)$$

where  $U_0$  - is the flow field characteristic velocity,

$w = W / U_0$  - is a dimensionless flow velocity,

$\phi = \Phi / U_0 b$  - is a dimensionless velocity potential.

The unsteady pressure distribution can be found using the potential difference  $\Delta\phi$  across the vorticity sheet  $\sigma$ , which is defined as

$$\Delta\phi(\mathbf{r}_\sigma) = \phi_i(\mathbf{r}_\sigma) - \phi_j(\mathbf{r}_\sigma) = \Gamma_\sigma, \quad (51)$$

where  $\Gamma_\sigma$  is the circulation of a vortex element representing the vortex sheet at  $\mathbf{r}_\sigma$ , and indices  $i$  and  $j$  refer to the upper and lower sides of the vorticity sheet  $\sigma$ , respectively.

Thus, the Equation (50) can be presented as

$$C_p(\mathbf{r}_\sigma, t) = 1 - w^2(\mathbf{r}_\sigma, t) - 2 \frac{\partial [\phi(\mathbf{r}_\sigma, t) - \phi(\mathbf{r}_s, t)]}{\partial t} - 2 \frac{\partial \phi(\mathbf{r}_s, t)}{\partial t}, \quad (52)$$

where  $\mathbf{r}_s$  is a coordinate vector of the leading edge stagnation point.

Then, according to the Equation (51)

$$\phi_i(\mathbf{r}_\sigma, t) - \phi_i(\mathbf{r}_s, t) = [\phi_j(\mathbf{r}_\sigma, t) + \Delta\phi(\mathbf{r}_\sigma, t)] - [\phi_j(\mathbf{r}_s, t) + \Delta\phi(\mathbf{r}_s, t)]. \quad (53)$$

Assuming that  $\Delta\phi(\mathbf{r}_\sigma) = \Gamma_\sigma$  and  $\Delta\phi(\mathbf{r}_s) = \Gamma_s$ , the above equation can be differentiated as

$$\frac{\partial}{\partial t} [\phi_i(\mathbf{r}_\sigma, t) - \phi_i(\mathbf{r}_s, t)] = \frac{\partial}{\partial t} [\phi_j(\mathbf{r}_\sigma, t) - \phi_j(\mathbf{r}_s, t)] + \frac{\partial}{\partial t} (\Gamma_\sigma - \Gamma_s). \quad (54)$$

According to the boundary conditions, there is no motion allowed inside the body surface, so

$$\phi_j(\mathbf{r}_\sigma, t) - \phi_j(\mathbf{r}_s, t) = 0, \quad (55)$$

giving

$$\frac{\partial}{\partial t} [\phi_i(\mathbf{r}_\sigma, t) - \phi_i(\mathbf{r}_s, t)] = \frac{\partial}{\partial t} (\Gamma_\sigma - \Gamma_s). \quad (56)$$

Due to temporal discretisation of the problem, the above equation can be written as

$$\frac{\partial}{\partial t} [\phi_i(\mathbf{r}_\sigma, t) - \phi_i(\mathbf{r}_s, t)] = \frac{(\Gamma'_\sigma - \Gamma'^{i-1}_\sigma - \Gamma'_s + \Gamma'^{i-1}_s)}{\Delta t}. \quad (57)$$

By definition

$$\phi_i(\mathbf{r}_s, t) = \phi_\infty + \int_{+\infty}^s \mathbf{w}_x dx, \quad (58)$$

where  $\phi_\infty$  is the potential of free-stream velocity field and

$$\frac{\partial \phi_i(\mathbf{r}_s, t)}{\partial t} = \int_{+\infty}^s \frac{\partial \mathbf{w}_x}{\partial t} dx. \quad (59)$$

Having defined all the unknown terms from Equation (50), a distribution of unsteady pressure coefficients can be integrated over the whole body surface to obtain instantaneous values of aerodynamic forces  $N(\mathbf{z}, t)$  and moments  $M(\mathbf{z}, t)$  required for the solution of the equations of motion (23), (24).

## 5. Numerical Solution of Aeroelastic Equations

The aeroelastic equations, describing dynamic response of a buffeting tail, and an unsteady aerodynamic model that determines motion-dependent buffet loads have been developed in non-dimensional form in previous sections. After introduction of the variable  $\eta_i = \partial q_i(t) / \partial t$ , the governing equations of motion (23), (24) result in a set of first-order differential equations, which can be presented in state space form as

$$\left\{ \begin{array}{c} \left\{ \frac{\partial \eta}{\partial t} \right\} \\ \left\{ \frac{\partial q}{\partial t} \right\}_d \end{array} \right\} = \begin{bmatrix} 0 & -[M]^{-1}[K] \\ [I] & 0 \end{bmatrix} \left\{ \begin{array}{c} \{\eta\} \\ \{q\}_d \end{array} \right\} + \left\{ \begin{array}{c} [M]^{-1}\{A\}_d \\ 0 \end{array} \right\}, \quad (60)$$

see Strganac [52]. Here, the number of equations is twice the number of modes chosen to represent the dynamical system.

Solution of the above equations in the time domain presents a certain challenge since the aerodynamic loads depend on the tail motion, yet the tail motion cannot be determined unless the aerodynamic loads are known. Following Strganac, an iterative numerical integration scheme that accounts for the interaction between the aerodynamic loads and tail dynamic response is developed which determines the motion of the structure and the motion-dependent aerodynamic loads simultaneously. The method is based on a fourth-order Hamming's predictor-corrector method, see Carnahan, *et al.* [73]. An advantage of the predictor-corrector method is that it does not subdivide a time step of integration, as do other numerical integration techniques, such as the Runge-Kutta method, providing substantial economy of computations.

Hamming's scheme requires the values of the dependent variables at the current and three previous time steps as well as their derivatives at the current and two previous time steps. Using initial conditions, the starting values of the dependent variables and their derivatives can be found using a fourth order Runge-Kutta method. Having this data, the values of state variables  $f_i$  for the next time step  $t + 1$  can be predicted by a fourth order Milne predictor as

$$f_i^{t+1} = f_i^{t-3} + \frac{4}{3} \Delta t (2f_i'' - f_i^{t-1} + 2f_i^{t-2}) \quad (61)$$

At the end of each time step, the local truncation error  $e_i'$  is estimated and used to modify the predicted value of the state variables as

$$\tilde{f}_{i,0}^{t+1} = f_{i,0}^{t+1} + \frac{112}{9} e_i', \quad (62)$$

assuming that the value of the local truncation error does not change significantly on successive intervals [73]. Then Hamming's corrector equation is solved iteratively using the successive substitution algorithm at each iteration step  $j$  to obtain the updated state variables

$$f_{i,j}^{t+1} = \frac{1}{8} \left[ 9f_i' - f_i^{t-2} + 3\Delta t (\tilde{f}_{i,j-1}^{t+1} + 2f_i'' - f_i^{t-1}) \right], \quad j = 1, 2, \dots, k \quad (63)$$

until convergence of all the state variables is achieved after  $k$  iterations.

Once convergence of the state variables and loads has been achieved, the local truncation error for the corrector equation is estimated as

$$e_i^{t+1} = \frac{9}{121} (f_{i,k}^{t+1} - f_{i,0}^{t+1}), \quad (64)$$

and the final values of the state variables are determined similarly to Milne's method as

$$f_i^{t+1} = f_{i,k}^{t+1} - e_i^{t+1}. \quad (65)$$

For each time step, integration of the equation of motion by Hamming's method begins with the computation of the fluid flow by solving Equation (37) and convection of wake vorticity to the new force-free position from the position generated at the end of the last time step. A flowchart detailing the general approach for computation of the dynamic solution is presented in Figure 1.

Here, the new state variables are predicted using aerodynamic loads computed at the last time step and applied to the structural dynamics model. This new wake geometry and new state variables are used to compute the aerodynamic loads. Then, the state variables are corrected, new tail geometry is computed, the aerodynamic loads are updated, and convergence of both the state variables and aerodynamic loads is checked. If convergence is not achieved, the state variables are corrected again and new aerodynamic loads are determined. This process is repeated until convergence of the loads and tail motion is achieved. Here, the new state variables are predicted for the first integration pass and are corrected for all subsequent passes while maintaining the flowfield in a fixed position.

Next, the wake vorticity is re-convected from its position generated at the end of the last time step using flow conditions based on the initial and corrected values of the state variables. This updated position of the wake vorticity is checked for convergence with its previous position and is convected by an iterative process to a new converged position while keeping the state variables fixed. The iteration continues with the use of the new converged flowfield conditions for updating the state variables until their convergence with the aerodynamic loads is achieved during the fixed flowfield computations and then again proceeds with the iterative convection of wake. This two-stage iterative scheme is aimed at providing full convergence of the wake position, state variables and the aerodynamic loads at the end of each time step prior to advancing to the next time step.

Despite this integration scheme for the aeroelastic equations being able to provide rather accurate convergence of motion and loads, its excessive computational requirements were found to be prohibitive for buffet computations when long computed time histories are required to resolve time-dependent data. Thus, a simplified algorithm was investigated for integration of the equations of motion, where the geometry of the wake remains the same as generated at the first iteration pass and is not updated each time the state variables are determined, see Figure 2. When the new tail geometry is computed, the aerodynamic loads are updated, and convergence



of both the state variables and aerodynamic loads is checked. If convergence is not achieved, the state variables are corrected and new aerodynamic loads are determined. Here, only unsteady aerodynamic loads are updated each time the state variables are predicted or corrected. This process is repeated until convergence of the loads and tail motion is achieved while maintaining the flowfield in a fixed position.

It was found that the results of the lower-order integration scheme for some test cases show no noticeable difference over the more accurate higher-order scheme while providing substantial economy of computation. Therefore, this simplified integration scheme was adopted and subsequently used for modelling the vertical tail buffet in this study.

## 5.1 Temporal and Spatial Discretisation

Note, that the vortex algorithm for simulation of unsteady separated flow employs an iterative time marching scheme in which one system of vortex elements is shed from the body surface at every time step. The accuracy of such a model depends on a correct balance between the scales of spatial and temporal discretisation of the unsteady problem. For high Reynolds number flows with dominating influence of convection over diffusion, an appropriate spatial discretisation of the body must correspond to the scale of vorticity convective motion. According to vorticity inviscid dynamics, an average convective displacement  $\Delta l_c$  of the vorticity in a shear layer can be defined as

$$\Delta l_c = \frac{1}{2} U_0 \Delta t_c, \quad (66)$$

where  $U_0$  is a free-stream velocity and  $\Delta t_c$  is time step based on vorticity convective motion. A link between the convection displacement of vorticity  $\Delta l_c$ , governed by inviscid vorticity dynamics, and the corresponding scale  $\Delta s$  of the body surface discretisation may be defined as

$$k = \frac{\Delta l_c}{\Delta s}, \quad (67)$$

where  $k$  is in the range of  $[0...1]$ . Here, the scale of the body surface discretisation depends on the number of vortex elements  $n_v = l_c/\Delta s$  approximating the body surface where  $l_c$  is the body characteristic length equal to the length of the delta wing root chord.

Here, the scale of temporal discretisation must be chosen such as to satisfy numerical stability of the integration scheme for the structural dynamics part of the problem in order to resolve the highest order modes selected to represent the dynamic system.

## 6. Computation of Vertical Tail Dynamic Response

While an ultimate aim of the work is to investigate the F/A-18 empennage buffet, it was shown by Levinski [65] that the vertical tail buffet problem could be simulated efficiently using a generic delta wing, twin vertical-tail configuration. This simple configuration contains all the pertinent physics involved in the development and burst of a leading-edge vortex and its subsequent interaction with the vertical tails. Here, the delta wing is used to generate the leading-edge vortices, which tend to break down over the wing resulting in highly turbulent swirling flow. This energetic, vortex-breakdown flow then impinges on the vertical tails producing unsteady, unbalanced buffet loads on the tail surfaces and causing their dynamic response (buffeting).

The dynamic aeroelastic computational model described in the previous sections is employed to simulate the development of the unsteady buffet loads produced by the vortex breakdown flow as well as to predict the vertical tail dynamic response. In this way, the major characteristics of the vertical tail buffet can be investigated without complications associated with simulation of the flow over the complete F/A-18 aircraft.

### 6.1 Computational Model

The same delta wing, twin vertical-tail configuration as used in the previous buffet study of Levinski [65] is employed to computationally simulate the vertical tail dynamic response. It consists of a sharp-edged, 76-degree leading edge sweep delta wing and swept-back F/A-18 twin tails, see Figure 3 and Figure 4. Both the delta wing and twin tails are of zero thickness. Each of the tails is of aspect ratio 1.2 with the root chord length of 0.4 and a tip chord length of 0.159, based on the delta wing root chord. The tails are cantilevered on the upper surface of a trailing edge extension of the delta wing and have a sweepback angle of 35 degrees for a quarter-chord spanwise line. The tip of each tail is inclined outboard such that dihedral angle between the two tails is 40 degrees. The spanwise separation distance between the tails at the root is 50% of the delta wing span.

The numerical simulation procedure requires a discretisation of the computational model, thus a total of 2986 closed vortex rings, or panels, are used for spatial discretisation of the delta wing, trailing edge extension and twin vertical tails. A unit aspect ratio delta wing is modelled using 2178 quadrilateral vortex panels. The vortex system of the trailing edge extension continues the discretisation pattern of the delta wing and is represented by 416 rectangular panels while 196 trapezoidal panels model each of the vertical tails.

The 'no-penetration' boundary condition is imposed on all of the lifting surfaces. The unsteady wake is modelled as a vortex sheet, composed of vortex panels, which emanates from the sharp edges of the delta wing, trailing edge extension and vertical

tails. Only symmetrical flow cases are considered in the present buffet study. In all the test cases, the condition of flow symmetry is enforced during the computational simulation of the flow over the delta wing, twin-tail configuration.

Each of the elastic vertical tails of the computational model is treated as a swept back beam which is allowed to oscillate in bending and torsion modes representing the first bending and torsion modes of the F/A-18 vertical tails. In the present study of coupled bending-torsion response, the distance between the elastic axis and the inertia axis for each of the tails is set equal to 0.04 based on delta wing root chord.

## 6.2 Test Conditions

Previous sub-scale and full-scale experimental investigations of the F/A-18 vertical tail buffet as well as flight trials have shown that the frequency characteristics and intensity of the tail buffet vary primarily as a function of angle of attack and dynamic pressure. Analysis of the dynamic flight test results indicated that vertical tail first bending (15.8Hz) and first torsion (45.7Hz) modes have the most significant impact on the fatigue life of the empennage structure so these two modes are considered as fatigue critical modes of vibration. The flight conditions at which peak response levels occur for the most damaging vertical tail modes are found to be at 20-39 degrees angle of attack and 175-400 psf dynamic pressure [74]. Based on the critical dynamic response region, the test conditions for the dynamic aeroelastic model were selected to vary between 20 and 40 degrees angle of attack at 250 psf dynamic pressure and altitude of 10,000 ft as these conditions are most important in vertical tail buffet studies.

During the simulations, the fluid was started impulsively and computation was carried out for 300 time steps with a dimensionless time increment of  $\Delta t = 0.012$  that allows the vortex wake to travel 8.6 tail root chord lengths at the rate of the free-stream velocity. At the selected test condition of 10,000 ft altitude and 250 psf dynamic pressure, the total computed time interval corresponds to 0.143 seconds of real flight time. This computational time span is deemed to be adequate to obtain a fully developed vortex wake allowing the unsteady buffet loads to be considered as random and stationary in a statistical sense.

However, at the above test conditions the dynamically scaled elastic tail would complete only two oscillations in the first bending mode, and that is not sufficient for a reliable statistical analysis of its dynamic response especially when taking into account the initial transition period of vortex wake development. Therefore, stiffness and inertial properties of the elastic tail are selected such that during the computational time span the vertical tail is expected to complete more than four oscillations in the first bending mode and about eight oscillations in the first torsion mode.

### 6.3 Vortex Wake Structure

Particle traces of unsteady wake development over the delta wing, vertical-tail configuration at different angles of attack after 300 time steps are presented in Figure 5, Figure 7 and Figure 9 for the rigid tail computations obtained in [65] and in Figure 11, Figure 13 and Figure 15 for the flexible tail computations. Here, only the leading edge vortex wakes are visualised for clarity. Comparison of the results shows a similarity of the wake structures for all the test cases. As can be seen in all the test cases, the initially stable leading edge vortex experiences perturbations and breaks down prior to impinging on the vertical tails and results in a highly disturbed wake, which convects downstream undergoing gradual expansion.

The characteristic feature of the wake structure for all the test cases is the presence of periodic vortex clusters in the severely degenerated vortex wake. The wake periodicity is observed in the results obtained during both the rigid and flexible tail computations. The presence of coherent structures in the wake indicates an existence of a dominant frequency in the process of wake-structure interaction. It appears that dynamic response of the flexible tails affects the process of formation of the vortex clusters, as their periodicity is different compared with the rigid tail results.

Details of the leading edge flow development are provided in Figure 6, Figure 8 and Figure 10 for rigid tail computation and in Figure 12, Figure 14 and Figure 16 for flexible tail computation. Here, the leading edge vortex is visualised by particle traces, which are plotted for several consecutive time steps. As one can see, for all the test cases the vortex model reproduces the leading edge vortex roll-up, which is typical of the flow over delta wings. This leading edge vortex expands in a continuous manner while convecting downstream. The vortex core is initially intact and stable as indicated by the coinciding particle traces. However, at some point downstream, the growing scatter of the particle traces reveals the onset of instability and perturbation of the vortex cores, followed by sudden enlargement of the vortex core size.

For both the rigid and flexible tail calculations, the increase of the vortex core size is followed by development of highly diffuse and disorganised vortical flow, which indicates an appearance of the vortex breakdown. However, in the case of the flexible vertical tail, the regions of vortex wake appear to be larger and more diffuse as a result of interaction of wake vorticity with the deflecting vertical tails.

It can be seen for all the test cases that highly diffuse vortex flow convects downstream and partially covers the region inboard of the twin vertical tails. The twin tails cut through the leading edge vortices, forming two vortical flows inside the region between the twin tails and smaller vortical flows outside each tail. As in the case of rigid tails, the vortical flows inside the region are larger but weaker than those vortices that develop outside the tips of the twin tails. It is observed from the plots of vortex wake structure that interaction of the leading edge vortex flow with the flexible vertical tail causes more degeneration of the vortex wake compared with the rigid tail case, as indicated by highly scattered particle traces.

The severity of leading edge vortex burst becomes more pronounced at the higher angle of attack. For example, at 40 degrees angle of attack, the computed leading edge vortex is larger in size and its deterioration into an unsteady wake-like flow starts earlier compared to the lower angle of attack cases, see Figure 16. As indicated by a progressing scatter in particle traces, this perturbation in the well-defined leading edge vortex structure produces more severe degeneration of the vortex wake.

Insignificant scatter of the particle traces at the 20-degree angle of attack in Figure 12 shows only slight perturbation of the leading edge vortex when it approaches the trailing edge region. It indicates that in this case the wake has not deteriorated to the degree found at the higher angles of attack and actually remains stable all the way along the wing. This result is consistent with the result of rigid tail computation presented in Figure 6 and suggests that for this angle of attack the location of vortex breakdown is very close to the trailing edge.

Analysis of results indicates that for the angle of attack of 20 degrees and higher, the predicted burst location is forward of the wing trailing edge and moves upstream with the increase in the angle of attack. In all the test cases, the breakdown flow is located inside the region between the twin tails. It can be concluded that the increase in the angle of attack changes the shape of the vortex breakdown flow and the area occupied by the breakdown flow becomes larger in size.

Additional investigation into the structure of the leading edge vortex breakdown is performed using a three-dimensional view of the iso-surfaces of time-averaged pressure coefficient at 30 degrees angle of attack, see Figure 17 and Figure 18, for rigid and flexible tails, respectively. As indicated by the iso-surfaces in Figure 18, the centre of the vortex breakdown flow is located inboard of the vertical tail which is consistent with the rigid tail results and predictions of others, see [59, 65]. Similar to the rigid tail case, the area of vortex breakdown grows in size as it approaches the vertical tail and the decelerated flow starts to recover just after it passes the wing's trailing edge. However, it is evident that the deflections of the vertical tail change the location and shape of the vortex breakdown flow. The area of flow deceleration is larger in size and placed slightly upstream indicating that the leading edge vortex is experiencing more intense breakdown compared with the rigid tail case. Also, the fluid-structure interaction becomes more intense near the tail tips where deflections of the tail are the largest, and that results in further deceleration of vortex breakdown flow in the upper tail region.

## 6.4 Vertical Tail Buffet Loading

The magnitude and frequency content of instantaneous pressure fluctuations on the tail surface are the most important characteristics of tail buffet. Analysis of time-dependent random buffet data was performed using statistical data reduction techniques in the time and frequency domains, see, for example, Pettit, *et al.* [75].

The differential (buffet) pressure was estimated from time histories of surface pressure fluctuations as the difference between the inner surface pressure values and outer surface pressure values on the tail. The values of unsteady differential pressures were integrated over the vertical tail surface to give components of aerodynamic load coefficients. The unsteady pressure and loads coefficients were reduced to root-mean-square (RMS) and power spectral density (PSD) forms. The peak power and the dominant frequency of the unsteady buffet loads were determined from their PSD plots.

The root-mean-square (RMS) value of zero-mean differential pressure  $\Delta P'(\mathbf{r})$  at the vertical tail provides a measure of magnitude of the time-averaged fluctuations of the unsteady net pressure across the tail. It was determined by averaging the differential pressure history over a specified elapsed time  $t_e - t_s$  as follows

$$\Delta P'^2(\mathbf{r}) = \frac{1}{t_e - t_s} \int_{t_s}^{t_e} (P_{in}(\mathbf{r}, t) - P_{out}(\mathbf{r}, t))^2 dt = \frac{1}{t_e - t_s} \int_{t_s}^{t_e} \Delta P^2(\mathbf{r}, t) dt, \quad (68)$$

where  $P_{in}(\mathbf{r}, t)$  and  $P_{out}(\mathbf{r}, t)$  are zero-mean inner and outer pressure values on the tail. The averaging is performed from the moment the wake is considered as fully developed until the end of computation so that the dimensionless times for start  $t_s$  and end  $t_e$  of sampling are selected as 1.4 and 8.6 units, respectively.

The RMS differential pressure coefficient is then defined as

$$C'_{\Delta P}(\mathbf{r}) = \Delta P'(\mathbf{r}) / q_{\infty}, \quad (69)$$

where  $q_{\infty}$  is the free-stream dynamic pressure.

The frequency content of instantaneous pressure fluctuations was estimated using the power spectral density function of the unsteady component of the differential pressure coefficient. The differential pressure time histories from each test condition were converted into the frequency domain using Fast Fourier Transform (FFT) techniques. The pressure time histories were divided into blocks and the Hanning window was applied to reduce bandwidth leakage. The average PSD functions were obtained by averaging the fast Fourier transforms of each of the blocks with 50% overlap in order to increase statistical confidence. The dominant frequencies of the buffet pressure were identified from the power spectral density plots with dimensionless frequency resolution of 0.73 based on the tail's root chord.

### 6.4.1 Magnitude of Buffet Pressures

It is common in vertical tail buffet studies to examine and compare characteristics of surface pressure fluctuations measured at the 45% chord and 60% span location on the vertical tail. It provides a common base for comparison of the results of various experimental and numerical tail buffet studies. A computed time history of the differential pressure fluctuations at 45% chord and 60% span location obtained on the flexible vertical tail at 30 degrees angle of attack is presented in Figure 19 and accompanied by computational results obtained on a rigid tail. As one can see, for both the rigid and flexible tails, the differential pressure coefficients fluctuate substantially and exhibit oscillatory motion with large random fluctuations about a local mean value. However, the magnitude of differential pressure fluctuations on the flexible vertical tail is lower compared with the rigid tail case. This reduction of magnitude of buffet pressure fluctuations measured on the flexible tail is consistent with the trends obtained from experimental and flight test data in Figure 20, [30]. Here, the full-scale wind tunnel test of F/A-18 tail buffet [75] was performed at low dynamic pressure so the tail does not deflect and it could be considered as almost rigid in contrast to flight condition where the tail's dynamic response is significant.

As one can see in Figure 20, the flight and full-scale data follows the same trend as angle of attack increases, reaching a maximum value of buffet pressure near 30 degrees angle of attack. However, the flight data are lower in magnitude than the full-scale test data through all the angle of attack range, with the largest difference of up to 25% near 30 degrees angle of attack, which is explained by 'elastic relief effects'.

Variation of RMS differential pressure fluctuations obtained at 45% chord and 60% span location on rigid and flexible tails, and a full-scale wind tunnel test of F/A-18 tail buffet [75] at different angles of attack is presented in Figure 21. As one can see, the RMS buffet pressure fluctuations obtained on the flexible tail are lower than the rigid tail values for all the angles of attack but higher than full-scale test data. Despite the computed RMS buffet pressures not being expected to closely match measured data due to simplified geometry of the computational model, the overall reduction of buffet pressure values representing the effect of tail flexibility matches experimentally observed trends.

### 6.4.2 Spectral Content of Buffet Pressures

Spectral content of the differential pressure fluctuations at 30 degrees angle of attack at the 45% chord, 60% span location is presented in Figure 22 for rigid and flexible tail models. One can see that on the rigid tail the differential pressure contains energy over a relatively narrow frequency band with centre frequency of 2.9 corresponding to the dominant frequency of vortex breakdown flow. This differential pressure power peak occurs at about the same frequency values across the whole surface of the rigid tail. However, power spectral densities of considerably lower magnitudes are predicted for the flexible tail model where two distinct peaks are now aligned with the frequencies of

the tail bending and torsion modes. The presence of pressure fluctuations near the tail natural frequencies is the result of coupled flow-structure interaction where elastic tail response modifies the differential pressure fluctuations initially caused by turbulent vortex breakdown alone. These changes in magnitude and dominant frequencies of power spectral density of differential pressure between the rigid and flexible tails found at the 45% chord, 60% span location appear to be representative for the majority of other locations on the tail.

Random fluctuations of the buffet pressures are caused by interaction of the highly turbulent leading edge vortex flow with the vortex system of the twin vertical tails. The leading edge vortex breakdown causes flow deceleration and the leading edge vorticity tends to concentrate in the region near the twin tails, gradually building up a vortex cloud. The process of formation and destruction of the vortex clouds interacting with the tail vortex system drives the oscillatory behaviour of the buffet loads. These drifting clouds of scattered vorticity are also subjected to random-like motion caused by vortices bouncing back off the tail surface that also imposes a certain degree of randomness to the surface pressure distribution.

The periodicity of the vortex cloud formation determines the dominant frequencies of buffeting flow. However, this is further affected by the dynamic response of the flexible vertical tails. The vertical tail deflections change the location and shape of the vortex breakdown flow that modifies pressure distribution on the tails, as well as its frequency content, by the appearance of motion-driven pressure fluctuations. The resulting buffet pressure magnitudes and frequency content depend on intensity and coupling of both the unsteady aerodynamic loads arising from the leading edge vortex burst and those caused by the vibration of the tail.

Note, that the vortex model overpredicts the characteristic frequency of the pressure fluctuations on the rigid tail as the dominant frequency of about 0.5 was identified in most of the sub-scale and full-scale experiments on F/A-18 tail buffet, see [12, 75]. This characteristic frequency is a property of the flowfield of the burst LEX vortex and further development of the vortex model is required to rectify this discrepancy.

#### 6.4.3 RMS Pressure Distribution

Contour plots of the calculated RMS differential pressure fluctuations on a flexible vertical tail are presented in Figure 23 through Figure 27 for five values of angle of attack between 20 and 40 degrees. They are accompanied by rigid tail results to investigate variation of buffet pressure distribution at different test conditions.

For both the rigid and flexible models, the magnitude of RMS differential pressure in most of the locations increases with the increase of angle of attack due to an increase in the strength of the leading edge vortex before its subsequent burst as well as the upstream movement of the location of vortex breakdown.



On the flexible tail, the pressure fluctuations are higher at the leading edge as this area is the closest to the breakdown location, while the pressure fluctuations tend to decrease towards the trailing edge. However, on a rigid tail, the decrease in differential pressure towards the trailing edge is rather uniform while on a flexible tail the pattern is more complex and irregular. On the flexible tail, high RMS differential pressure values are found not only near the leading edge close to the tail's root, but also at the tail tip and near the upper part of the trailing edge. The largest gradients of the RMS differential pressure values are still detected in the leading edge area. Although the general trend of decrease of buffet pressure RMS towards the trailing edge is present for most of the test cases, the pressure field is obviously affected by the tail dynamic response, especially at those parts of the tail surface where deflections are the largest.

In general, the patterns of the intensity of the unsteady pressure fluctuations on rigid and flexible tails have more similarity for angles of attack of 30 degrees and higher, with some considerable differences appearing for the lower values of incidence. For example, at 20 and 25 degrees angle of attack, the magnitude of the RMS differential pressure on the rigid tail gradually decreases towards the trailing edge in the chordwise direction and towards the tail tip in spanwise direction. Here, the position of the centre of the vortex breakdown flow accounts for the pattern of the pressure fluctuations where the lower half of the tails experience larger RMS pressure levels than those on the rest of the tail. However, dynamic response of the flexible tail affects the flowfield around the tail and this considerably changes the pattern of buffet pressure distribution resulting in lower RMS pressure values than those obtained on the rigid tail model.

It should be noted that an improved vorticity convection algorithm was incorporated into the flexible tail model following computation of the rigid tail pressures. It was found that higher RMS differential pressure values in this area on the rigid tail model were caused by the development of a local stagnation zone and overproduction of vorticity at the junction of vertical tail, and delta wing and its trailing edge extension vortex systems. This shortcoming was rectified in the vorticity convection algorithm in the flexible tail model and this partially explains the difference between the rigid and flexible tail results in the area near the leading edge near the tail root.

The results indicate that an increase in the angle of attack intensified tail buffet by increasing the RMS levels of differential pressure fluctuations and expanded the region of peak loading from the root of the tail toward the leading edge and centre of the tail. Thus, at angles of attack of 30 degrees and higher, the distribution of the differential pressures on the rigid tail is more even in the spanwise direction and decreases towards the trailing edge mainly in the chordwise direction. The results for the flexible tail show similar trends with the major difference in the upper trailing edge area where deflections are large but there is little interaction with vortex breakdown flow as it passes over the upper part of the tail.

#### 6.4.4 Vertical Tail Buffet Loads

At each time step, the zero-mean differential pressures were integrated over the tail surface to obtain the instantaneous values of normal force and root bending moment coefficients. The time history of the zero-mean unsteady normal force coefficient was determined as

$$C_N(t) = \frac{1}{q_\infty A_F} \sum_i (P_{in}(\mathbf{r}_i, t) - P_{out}(\mathbf{r}_i, t)) A_i = \frac{1}{A_F} \sum_i C_{\Delta P}(\mathbf{r}_i, t) A_i, \quad (70)$$

where  $A_F$  is the total planform area of the tail,  $A_i$  is the area of the  $i$ -th panel on the tail and the instantaneous pressure differential  $C_{\Delta P}$  is evaluated at the centre of the  $i$ -th panel. Here, the surface pressure over the panel area was assumed to be constant and equal to the pressure computed at the centre of the panel, which is defined as the point of intersection of two lines connecting midpoints of the opposite sides of the panel.

The time history of zero-mean root bending moment was evaluated in a similar manner, assuming that the resultant force over the  $i$ -th panel is acting at the panel's centre

$$C_M(t) = \frac{1}{q_\infty A_F c_F} \sum_i (P_{in}(\mathbf{r}_i, t) - P_{out}(\mathbf{r}_i, t)) A_i l_i = \frac{1}{A_F c_F} \sum_i C_{\Delta P}(\mathbf{r}_i, t) A_i l_i, \quad (71)$$

where  $c_F$  is the tail root chord and  $l_i$  is the distance from the tail root to the centre of the  $i$ -th panel.

Finally, the zero-mean RMS values of fluctuating normal force and root bending moment coefficients, which provide a measure of the average fluctuations of the unsteady buffet loads at the vertical tail are determined as

$$C_N'^2 = \frac{1}{t_e - t_s} \int_{t_s}^{t_e} C_N^2(t) dt, \quad (72)$$

and

$$C_M'^2 = \frac{1}{t_e - t_s} \int_{t_s}^{t_e} C_M^2(t) dt, \quad (73)$$

respectively.

The variation of RMS normal force coefficients for rigid and flexible tails as a function of angle of attack is presented in Figure 28, and compared with full-scale experimental data from [75]. The variation of RMS root bending moment coefficients at different

angles of attack is also presented in Figure 29 and compared with the results of full-scale tail buffet test [75].

Comparison of the computed RMS normal forces and bending moments in Figure 28 and Figure 29 shows that flexible tail model produces higher values of both the normal force and bending moment coefficients compared with rigid tail model despite predicting lower RMS differential pressure values for most of the tail surface. This is because differential buffet pressures generated by the flexible tail model have higher values of cross-correlation over the tail surface as the flowfield near the tail is modified by tail's motion.

In general, both the flexible and rigid tail models produce values of RMS buffet loads which are reasonably close to those measured during full-scale test. Note that despite higher magnitudes of RMS buffet loads generated by the flexible tail model, their variation with angle of attack closely matches the trends observed in the rigid tail results. Initially, both the computed and measured values of RMS buffet loads increase with the angle of attack. This is caused by the increase of the RMS differential pressures for most of the locations on the tail, due to the increase of leading edge vortex strength at higher angles of attack. However, both the rigid and flexible models fail to follow the experimentally obtained trend for angles of attack of 30 degrees and higher where the values of experimentally measured RMS buffet loads start to decline after reaching a peak value at 32 degrees of angle of attack. Here, predicted RMS buffet loads for both rigid and flexible tail experience a local minimum at 30 degrees and continue to increase at higher angles of attack. Further numerical and experimental investigation is required to determine if such a behaviour of predicted RMS buffet loads is either specific to the computational model geometry or to the predictive capabilities of the vortex model at higher angles of attack.

Power spectral density functions of unsteady normal force and root bending moment coefficients are determined from their time histories in a manner similar to the buffet pressure PSD. Variation in the spectral content of unsteady normal force coefficient with angle of attack is presented in Figure 30 and Figure 31 for rigid and flexible tails, respectively. Variation in the spectral content of unsteady root bending moment coefficient with angle of attack is also presented in Figure 32 and Figure 33 for both the rigid and flexible tails.

Investigation of the PSD plots for the rigid and flexible tails indicates that the peaks of the power spectral density of normal force coefficient can be detected for all the angles of attack, and dominant frequencies at which the normal force is exerted on the vertical tail tend to decrease at higher angles of attack. It can be noted that there is a similarity of variation of dominant frequencies with angle of attack between the rigid and flexible tail cases, however spectral content of normal force coefficient on the flexible tail seems to be affected by its dynamic response in bending and torsion modes.

Here, for the flexible tail at 20 degrees angle of attack, a main peak is generated at the reduced frequency of 3.6 while a noticeable peak is also present near 0.73, which is the

frequency of the tail bending mode. At 30 degrees angle of attack, a strong single peak of load power is aligned with the frequency of 1.9 that is close to the frequency of the tail torsion mode. For both the rigid and flexible tails at 40 degrees angle of attack, the stronger of the two peaks is generated at the frequency of the tail bending mode and the other is at the frequency of 3.6. A number of minor peaks can also be identified in the PSD plots but their frequencies are well above the vertical tail modal frequencies and they are not considered as critical for the present study.

Variation in the spectral content of unsteady root bending moment coefficient with angle of attack in Figure 32 and Figure 33 experiences similar trends, however at 40 degrees angle of attack, a much stronger peak of bending moment power is generated at the frequency of 3.6 which becomes comparable in magnitude to the other major peak that is aligned with the frequency of the tail bending mode.

## 6.5 Vertical Tail Dynamic Aeroelastic Response

Computational time histories of generalised coordinates  $q$  for bending and torsion modes of vibration for the vertical tail are presented in Figure 34 through Figure 38 for five different angles of attack in 20 to 40 degrees range. The time histories show near harmonic variations of generalised coordinates for both bending and torsion responses for most of the test cases. However, it can be noticed that periodicity of dynamic response was not fully developed due to insufficient length of computed time histories. This is most evident for the bending mode due to its lower natural frequency, but can also be seen for the torsional mode having intermittent oscillations of higher than average amplitude. A certain degree of irregularity in the time histories of generalised coordinates for bending and torsion can be explained by aerodynamic as well as structural coupling between the modes.

It is known from test data that for high angle of attack manoeuvring conditions the modal response of the vertical tails is vulnerable to changes from one dominant mode to another, see Triplett [76]. Measured variation of relative magnitudes of peak PSD associated with the first two modes of the F/A-18 tail is presented in Figure 39. A rapid decline in relative magnitude of the torsion mode after 25 degrees, dominance of the bending mode by 35 degrees and their crossover at about 30 degrees angle of attack, are the most interesting features of the modal response variation.

In the present study, the length of computed time histories does not allow for accurate assessment of PSD peaks values. Thus, the variation of participation of the bending and torsion modes in the total dynamic response of the tail at different angles of attack is evaluated by calculating generalised coordinate RMS values for each of the modes, see Figure 40. The results indicate that, in general, the predicted variation in modal response follows the experimentally observed trends with the torsion mode peaking around 25 degrees angle of attack and bending mode peaking at 35 degrees angle of attack. Despite some scatter in the computed data, both the increase in relative magnitude of the bending mode and decline of the torsion mode at higher angles of

attack are reproduced correctly. Note, that the predicted decline of relative magnitude of bending mode after 35 degrees angles of attack is also in agreement with experimental data.

Computed time histories of tail forward and aft tip deflections are shown in Figure 41 through Figure 45 for five values of angle of attack. Here, the variation of relative magnitudes of the bending and torsion modes determines the overall tip response where the contribution of the torsion mode is only noticeable at 25 degrees of attack or higher while the bending mode dominates the overall tip response for all the test conditions. The difference between the amplitudes of tips deflection is the result of coupling between the bending and torsion modes and the presence of static aeroelastic deformations of the tail. As one can see, the tail aft tip experiences larger total deflections compared with the forward tip.

## 7. Conclusions

The development of a computational model for the prediction of the unsteady aeroelastic behavior of a flexible tail under buffet-induced loads has been described. The multidisciplinary problem of tail buffeting is solved in a time domain using an unsteady vortex model for the prediction of aerodynamic loads and coupled aeroelastic equations for the bending and torsional deflections of the tail which are resolved using the Galerkin method. The set of ordinary differential equations governing the motion of the dynamic system is integrated by a predictor-corrector algorithm.

A dynamic aeroelastic analysis of empennage buffet is performed for a generic delta wing, twin vertical-tail configuration at high angles of attack. The computational model consists of a 76-degree sharp-edged delta wing along with F/A-18 twin vertical tails, where only the twin vertical tails are flexible and modelled using a linear modal method.

The aim of the study is to simulate the coupled fluid-structure interaction and present time-accurate integration of the empennage dynamic aeroelastic response to the unsteady pressure loads caused by the vortex breakdown present at the high angle of attack conditions. Results include time histories of unsteady buffet loads and dynamic response of the tail. Comparisons are made with the rigid tail differential pressures and loads, as well as available test data.

It was shown that the numerical solution is able to predict onset of the vortex burst and qualitatively describe the characteristics of unsteady buffet loads on the vertical tail. It is found that inclusion of the tail flexibility affects the shape and location of vortex breakdown and results in degeneration of the leading edge vortex structure into a

larger and more diffuse flow region where the location of vortex breakdown tends to move forward compared to the rigid tail case.

It is found that the magnitude of differential pressure fluctuations on a flexible vertical tail is lower compared to the rigid tail case and this is consistent with experimental and flight test data. Despite both the rigid and flexible tail models over-predicting the measured data, the overall reduction of buffet pressure values representing the effect of tail flexibility matches experimentally observed trends.

A comparison of computational results with available wind-tunnel and flight test data of F/A-18 tail buffet revealed that the dynamic aeroelastic model performed reasonably well in simulating the spatial and temporal characteristics of the buffet loads. Computational analysis of the flexible tail showed a difference in buffet loading when compared to the rigid tail model. Here, both the tail bending and torsion modes had a noticeable contribution to the buffet load magnitude and frequency content and this emphasises the need to account for tail flexibility during computations of the empennage buffet.

Investigation of the power spectral density plots for the buffet loads indicates that the dominant frequencies at which the normal force and root bending moment are exerted on the vertical tail tend to decrease at higher angles of attack and this compares well with available experimental results.

It is also noted that the predicted variation in modal response of the flexible vertical tail follows the experimentally observed trends. Despite some scatter in the computed data, both the increase in relative magnitude of the bending mode and decline of the torsion mode at higher angles of attack are reproduced correctly.

Although the aeroelastic model captured many of the experimentally observed trends, analysis of the power spectral density of the predicted differential pressures on the tail indicated that the characteristic frequency of vortex breakdown is higher than the measured values. Predictive capabilities of the vortex model should be refined in order to correctly predict variation of buffet loads and dynamic response of the tail at different angles of attack. This is left for future studies.

The present study demonstrates the use of an unsteady vortex model coupled with a structural dynamics model for time-domain aeroelastic analysis of aircraft empennage buffeting. The method is capable of predicting major unsteady features of vortex breakdown induced buffet loads that are required for characterizing empennage buffet and the resulting structural response. The present research provides advances in the predictive capability and our understanding of aircraft empennage buffet.

## 8. References

1. Technical Report by the Accident Investigation Sub-committee on the Accident to the Airplane G.AAZK at Meophan, Kent, on 21<sup>st</sup> July, 1930, R. & M. No. 1360, British A.R.C., January 1931.
2. Scanlon, R.W., Prey, S.W. (1985) *F-18 Vibrational Environmental Analysis Report, Addendum 2 - Vertical Tail Dynamic Response Test and Analysis*, McDonnell Aircraft Company, Report MDC A4488, Addendum 2.
3. Streber K. K., Rioux J. P. L., (1992) *CF-188 Aft Fuselage Flight Strain and Vibration Survey*, AETE Report 88/12, Aerospace Engineering Test Establishment, Alberta, Canada, May 1992.
4. Lee, B.H.K., Brown, D., Zdelá, M. and Poiré, D., (1990) *Wind tunnel investigation and flight test of tail buffet on the CF-18 aircraft*, AGARD CP-483, Aircraft Dynamic Loads due to Flow Separation, pp. 11-26.
5. Lee, B.H.K., Valerio, N.R., (1994) Vortical Flow structure near the F/A-18 LEX at high incidence, *Journal of Aircraft*, 31(5), pp.1221-3.
6. Thompson, D.H. (1997) *Effect of the Leading Edge Extension (LEX) Fence on the Vortex Structure over the F/A-18*, Aeronautical and Maritime Research Laboratory, DSTO-TP-0489.
7. Zimmerman, N.H., and Ferman, M.A. (1987) *Prediction of Tail Buffet Loads for Design Application*, Final Report, McDonnell Aircraft Company, St. Louis, Missouri, 63166.
8. Zimmerman, N.H., Ferman, M.A., and Yurkovich, R.N. (1989) *Prediction of Tail Buffet Loads for Design Application*, AIAA 89-1378-CP, AIAA/ASME/ASCE 30<sup>th</sup> Structures, Structural Dynamics and Materials Conference, Mobile, Alabama, April 1989, pp.1911-9.
9. Olafson, A. (2001) Private communication during PD9826 flight trials, Aerospace Engineering Test Establishment, CFB Cold Lake, Alberta, Canada, February 2001.
10. Rendo, C.J., Coulson, N.G., and Ward, L.R. (1997) *Hornet In-Flight Structural Acceleration and Strain Measurement - Aft Fuselage*, Australian Department of Defence, Royal Australian Air Force, Aircraft Research and Development Unit Formal Report - Task 0174.
11. Thompson, D.H. (1990) *Water tunnel flow visualization of vortex breakdown over the F/A-18*, Aeronautical Research Laboratory, Flight Mechanics Report 179.
12. Martin, C.A., Thompson, D.H. (1991) *Scale Model Measurements of Fin Buffet Due to Vortex Bursting on F/A-18*, AGARD Manoeuvring Aerodynamics, AGARD-CP-497.
13. Inan, S. (2002) *AETE PD98/26 F/A-18 Flight Test Dynamic Response Results*, Australian Department of Defence, DSTO, Aeronautical and Maritime Research Laboratory, Technical Report, DSTO-TR-1252.
14. Sellers, W.L. III, Meyers, J.F., Hephner, T.E. (1988) LDV surveys over a fighter model at moderate to high angles of attack, SAE Paper 88-1448, Aerospace Technology Conference and Exposition, Anaheim, California, October 1988.
15. Erickson, G.E., (1991) *Wind Tunnel Investigation of Vortex Flows on F/A-18 at Subsonic Through Transonic Speeds*, NASA TP 3111, December 1991.
16. Wentz, W.R., Jr. (1987) *Vortex-fin interaction on a fighter aircraft*, AIAA 7<sup>th</sup> Lighter-Than-Air Technology Conference, AIAA 87-2474, Monterey, California, August 1987.

17. Lee, B.H.K., Brown, D. (1992) Wind tunnel studies of F/A-18 tail buffet, *Journal of Aircraft*, 29(1), pp. 146-52.
18. Hebbar, S.K., Platzler, M.F., Cavazos, O.V. (1991) A water tunnel investigation of the effects of pitch rate and yaw on LEX generated vortices of an F/A-18 fighter aircraft model, AIAA 91-0280, 29<sup>th</sup> AIAA Aerospace Sciences Meeting, Reno, Nevada, January 1991.
19. Lee, B.H.K. and Tang, F. (1994) Characteristics of the Surface Pressure on a F/A-18 Vertical tail Fin Due to Buffet, AIAA Paper 92-2127, *Journal of Aircraft*, 31(1), January 1994.
20. Washburn, A.E., Jenkins, L.N., Ferman, M.A. (1993) Experimental Investigation of Vortex-Fin Interaction, AIAA Paper 93-0050, Reno, NV.
21. Shah, G., Grafton, S.B., Guynn, M.D., Brandon, J.M., Dansberry, B.E., Patel, S.R. (1991) Effect of Vortex Characteristics on Tail Buffet and High Angle of Attack Aerodynamics of a Twin Tail Fighter Configuration, NASA CP-3149, *High Angle of Attack Technology Conference*, October 1991.
22. Moss, S.W., Cole, S.R., Doggett, R.V., Jr. (1991) Some subsonic and transonic buffet characteristics of the twin-vertical-tails of a fighter airplane configuration, AIAA 91-1049-CP, AIAA/ASME/ASCE 32<sup>nd</sup> Structures, Structural Dynamics, and Materials Conference, Baltimore, Maryland, April, 1991, pp. 1742-50.
23. Moses, R.W. (1997) Spatial characteristics of the unsteady differential pressures on vertical tails of a twin-tailed aircraft at high angles of attack with emphasis on buffeting alleviation, PhD Thesis, Stanford University, August 1997.
24. Moses, R.W., Ashley, H. (1998) Spatial characteristics of the unsteady differential pressures on 16% F/A-18 vertical tails, AIAA 98-0519, 36<sup>th</sup> aerospace Sciences Meeting and Exhibit, Reno, Nevada, January, 1998.
25. Meyn, L.A., Lanser, W.R., James, K.D. (1992) Full-scale high angle-of-attack tests of an F/A-18, AIAA 92-2676, 10<sup>th</sup> AIAA Applied Aerodynamics Conference, Palo Alto, California, June 1992.
26. Meyn, L.A., James, K. D. (1993) Full Scale Wind Tunnel Studies of F/A-18 Tail Buffet, AIAA Applied Aerodynamics Conference, AIAA 93-3519, August 9-11, Monterey, CA.
27. Meyn, L.A., James, K. D. (1996) Full scale wind tunnel studies of F/A-18 tail buffet, *Journal of Aircraft*, 33(3), pp.589-95.
28. Meyn, L.A., James, K. D. (1994) Integrated tail buffet loads on the F/A-18, AIAA 94-1801, 12<sup>th</sup> AIAA Applied Aerodynamics Conference, Colorado Springs, Colorado, June 1994.
29. Pettit, C.L., Brown, D.L., and Pendleton, E. (1994) Wind tunnel tests of full-scale F/A-18 twin tail buffet: a summary of pressure and response measurements, AIAA-94-3476-CP.
30. Meyn, L.A., James, K.D., and Geenen, R.J. (1994) Correlation of F/A-18 Tail Buffet Results, *High-Alpha Projects & Technology Conference*, NASA Dryden Flight Research Center, July 1994.
31. Moses, R.W., Pendleton, E. (1996) A comparison of pressure measurements between a full-scale and a 1/6-Scale F/A-18 twin tail during buffet, NASA TM-110282.



32. Forshing, H.W. (1990) Unsteady aerodynamic forces on an oscillating wing at high incidences and flow separation. AGARD CP-483, *Aircraft Dynamic Loads due to Flow Separation*, 1990, pp. 7.1-18.
33. Theodorsen, T. (1940) *General Theory of Aerodynamic Instability and the Mechanism of Flutter*, NACA Report No. 496.
34. Bisplinghoff, R.L., Ashley, H., and Halfman R.L. (1955) *Aeroelasticity*, Addison-Wesley Publishing Company, Inc., Reading, Massachusetts.
35. Dowell, E.N. (Editor), et al. (1980) *A Modern Course in Aeroelasticity*, Sijtohoff & Noordhoff International Publishers, Alphen ann den Rijn, The Netherlands.
36. Bisplinghoff, R.L., and Ashley, H. (1975) *Principles of Aeroelasticity*, Dover Publications, Inc., New York.
37. Fung, Y.C. (1955) *An Introduction to the Theory of Aeroelasticity*, John Wiley & Sons, Inc. New York.
38. Pines, S. (1958) An Elementary Explanation of the Flutter Mechanism, *Proceedings of the National Specialists Meeting on Dynamics and Aeroelasticity*, November 1958.
39. Rizetta, D.P. (1979) Time-Dependent Responses of a Two-Dimensional Airfoil in Transonic Flow, *AIAA Journal*, Vol. 17, No. 1, pp. 26-32.
40. Rizetta D.P. (1977) Transonic Flutter Analysis of a Two-Dimensional Airfoil, AFFDL, TM-77-64-FBR.
41. Ballhaus, W.F., and Goorjian, P.M. (1978) Computation of Unsteady Transonic Flows by the Indicial Method, *AIAA Journal*, Vol. 16, No. 2, pp. 117-124.
42. Yang, T.Y., Guruswamy, P., and Striz, A.G. (1979) Aeroelastic Response Analysis of Two-Dimensional, Single and Two Degree of Freedom Airfoils in Low Frequency, Small Disturbance Unsteady Transonic Flow, AFFDL, TR-79-3077.
43. Yang, T.Y., Guruswamy, P., Striz, A.G., and Olsen, J.J. (1980) Flutter Analysis of a NACA 64A006 Airfoil in Small Disturbance Transonic Flow, *Journal of Aircraft*, Vol. 7, No. 4, pp. 225-232.
44. Guruswamy, P., and Yang, T.Y. (1981) Aeroelastic Time Response Analysis of Thin Airfoils by Transonic Code LTRAN2, *Computers and Fluids*, Vol. 9, No. 4, pp. 409-425.
45. Desmarais, R.N., Bennett, R.M. (1978) *User's Guide for a Modular Flutter Analysis Software System (FASS Version 1.0)*, NASA TM 78720.
46. Devers, A.D. (1972) *A General Method for Calculating Three Dimensional Nonstationary Aeroelastic Response in Subsonic Flows*, Arnold Engineering Development Center, TR-72-59, May 1972.
47. Guruswamy, P. and Goorjian, P.M. (1982) Comparison Between Computations and Experimental Data in Unsteady Three-Dimensional Transonic Aerodynamics, Including Aeroelastic Computations, *AIAA Paper 82-0690-CP*, May 1982.
48. Batina, J.T. (1988) Efficient Algorithm for Solution of the Unsteady Transonic Small-Disturbance Equation, *Journal of Aircraft*, Volume 25, pp. 598-605, July 1988.
49. Batina, J.T. (1989) Unsteady Transonic Algorithm Improvements for Realistic Aircraft Applications, *Journal of Aircraft*, Volume 26, pp. 131-139, February 1989.
50. Eastep, F.E., and Olsen, J.J. (1980) Transonic Flutter Analysis of a Rectangular Wing with Conventional Airfoil Sections, *AIAA Journal*, Vol. 18, No. 10, pp. 1159-1164.
51. Borland, C.J., and Rizetta, D.P. (1982) Nonlinear Transonic Flutter Analysis, *AIAA Journal*, Vol. 20, Nov. 1982, pp. 1606-1615.

52. Strganac, T.W. (1987) *A Numerical Model of Unsteady, Subsonic Aeroelastic Behavior*, NASA-TM-100487, December 1987.
53. Strganac, T.W., Mook, D.T. (1987) *A New Method to Predict Unsteady Aeroelastic Behavior*, AIAA Paper Number 87-0736, 28<sup>th</sup> Structures, Structural Dynamics and Materials Conference, April 1987.
54. Loring, S.J. (1941) General Approach to the Flutter Problem, *Society of Automotive Engineers Journal*, Vol. 49, No. 2, pp. 345-356.
55. Schuster, C.J., et al. (1989) *Euler/Navier-Stokes Aeroelastic Method (ENS3DAE) Technical Development Summary*, Flight Loads Prediction Methods for Aircraft, Volume 1, WRDC-TR-3104.
56. Guruswamy, G.P. (1990) Unsteady Aerodynamics and Aeroelastic Calculations for Wings Using Euler Equations, *AIAA Journal*, Volume 28, Number 3, March 1990.
57. Kandil, O.A., Kandil, H.A., and Massey, S.J. (1993) Simulation of Tail Buffet Using Delta Wing-Vertical Tail Configuration, AIAA93-3688-CP, AIAA Atmospheric Flight Mechanics Conference, Monterey, CA, pp. 566-577.
58. Kandil, O.A., Massey, S.J., and Sheta, E.F. (1995) Structural Dynamics/CFD Interaction for Computation of Vertical Tail Buffet, *International Forum on Aeroelasticity and Structural Dynamics*, Royal Aeronautical Society, Manchester, U.K., June 26-28, pp. 52.1-52.14.
59. Kandil, O.A., Sheta, E.F., Massey, S.J. (1996) Twin Tail/Delta Wing Configuration Buffet due to Unsteady Vortex Breakdown Flow, AIAA Paper 96-2517-CP.
60. Rizk Y., Guruswamy, G.P., and Gee, K. (1992) Numerical Investigation of Tail Buffet on F/A-18 Aircraft, AIAA Paper 92-2673, AIAA 10<sup>th</sup> Applied Aerodynamics Conference, Palo Alto, CA, June 1992.
61. Gee, K., Murman, S., and Schiff, L. (1996) Computation of F/A-18 Tail Buffet, *Journal of Aircraft*, Volume 33, Number 6, November-December 1996.
62. Findlay, D.B. (1999) *A Numerical Study of Aircraft Empennage Buffet*, PhD Thesis, Georgia Institute of Technology, June 1999.
63. Meirovitch, L. (1980) *Computational Methods in Structural Dynamics*, Sijtohoff & Noordhoff International Publishers, Alphen ann den Rijn, The Netherlands.
64. Levinski, O. (2001) *Review of Vortex Methods for Simulation of Vortex Breakdown*, Aeronautical and Maritime Research Laboratory, DSTO-TR-1211.
65. Levinski, O. (2001) *Prediction of Buffet Loads on Twin Vertical Tails Using a Vortex Method*, Aeronautical and Maritime Research Laboratory, DSTO-RR-0217.
66. Leonard, A. (1980) Vortex Methods for Flow Simulation. *J. Comp Phys.* 37, No. 3, 289-335.
67. Belotserkovskii, S.M., Nisht, M.I. (1978) Modelling of Turbulent Wakes in Ideal Fluids (Separated Flow Over Bluff Bodies), *Fluid Mech.-Research*, Vol.7, No. 1, 102-115.
68. Lamb, H. (1945) *Hydrodynamics*, Cambridge University Press.
69. Chorin, A.J. (1973) Numerical study of slightly viscous flows, *J. Fluid Mech.*, 57, 785-796.
70. Kuwahara, K., Takami, H. (1973) Numerical Studies of Two-Dimensional Vortex Motion by a System of a Point Vortices, *J. Phys. Soc. Japan*, Vol. 34, 247-253.
71. Leonard, A. (1985) Computing three-dimensional incompressible flows with vortex elements, *Ann. Rev. Fluid Mech.*, Vol. 17, 523-559.

72. Rosenhead, L. (1931) The Formation of Vortices from a Surface of Discontinuity, *Proc. Roy. Soc, Series A*, Vol.134, 170-192.
73. Carnahan, B., Luther, H.A., and Wilkes, J.O. (1969) *Applied Numerical Methods*, John Wiley & Sons, Inc., New York.
74. Mouser, C.R., Conser, D.P. (2001) *F/A-18 IFOSTP FT46 Pre Block 1 and Post Block 5 Dynamic Strain Survey Testing and Results*, Australian Department of Defence, DSTO, Aeronautical and Maritime Research Laboratory, DSTO-TR-1218.
75. Pettit, C.L., Brown, D.L., and Pendleton, E. (1994) Wind Tunnel Tests of Full-Scale F/A-18 Twin Tail Buffet: A Summary of Pressure and Response Measurements, AIAA Paper 94-3476.
76. Triplett, W.E. (1982) *Pressure Measurements on Twin Vertical Tails in Buffeting Flow, Volume I - General Description*, AFWAL-TP-82-3015, April 1982.

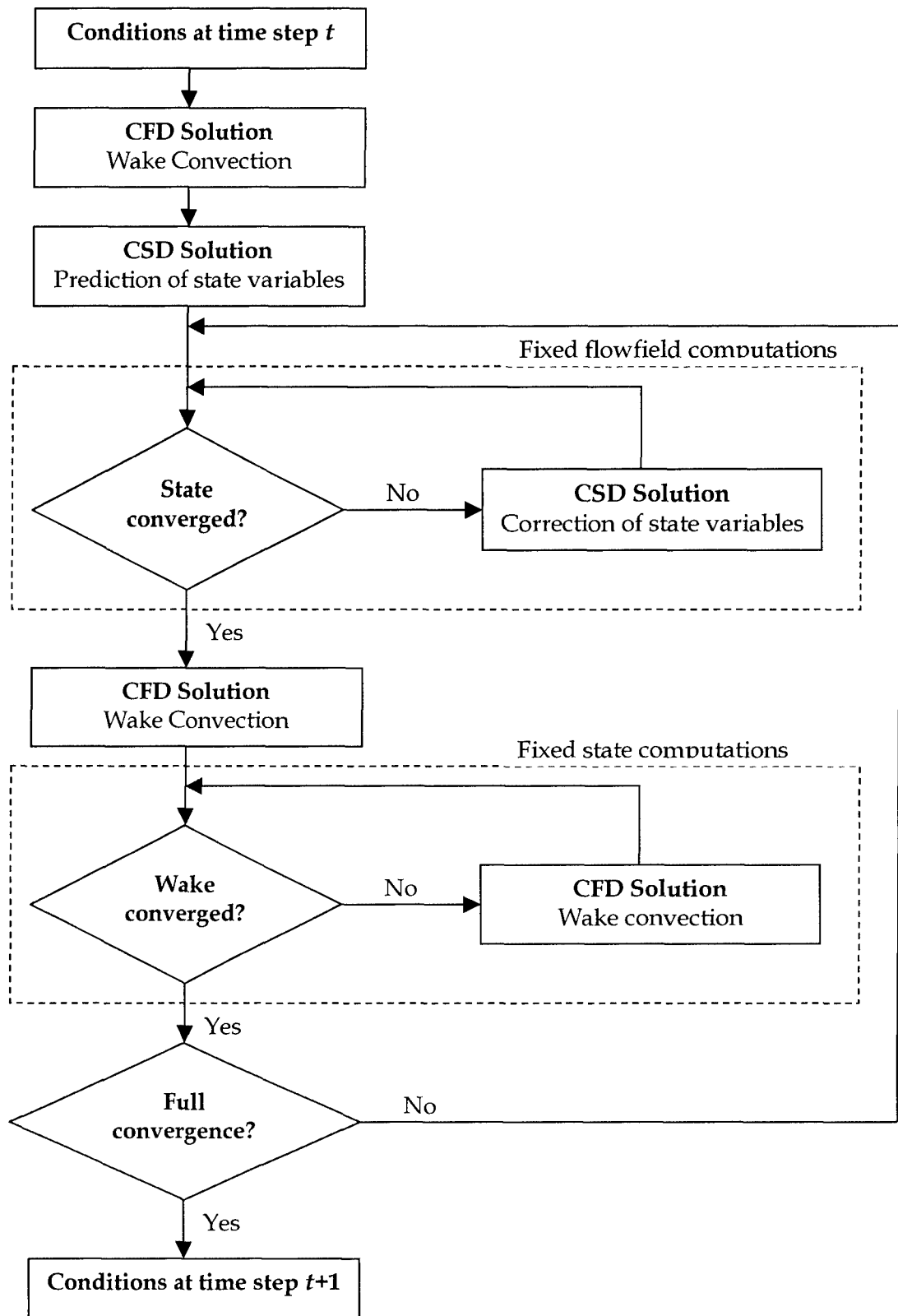


Figure 1 General integration scheme for dynamic solution

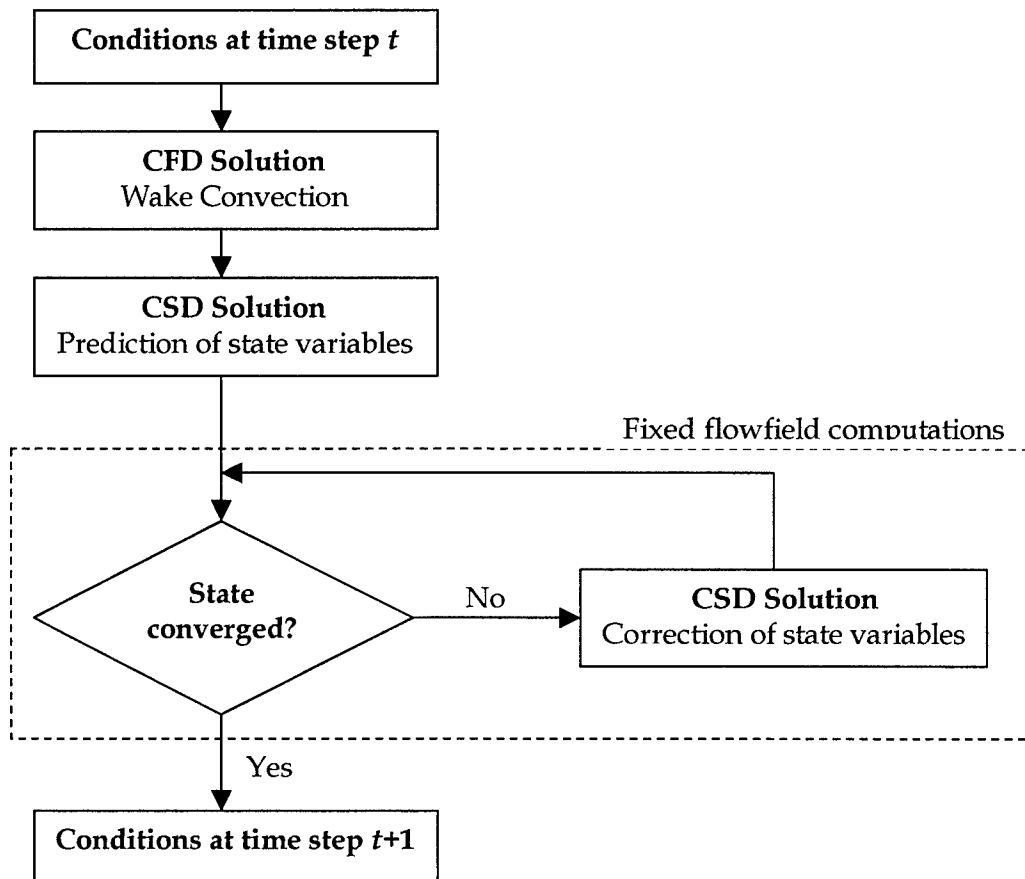


Figure 2 Simplified integration scheme for dynamic solution

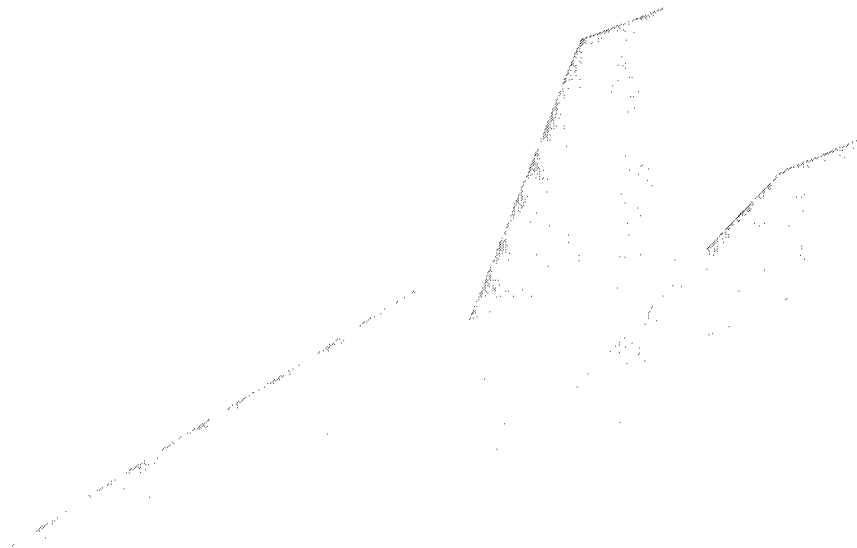


Figure 3 General view of delta wing, twin vertical-tail configuration

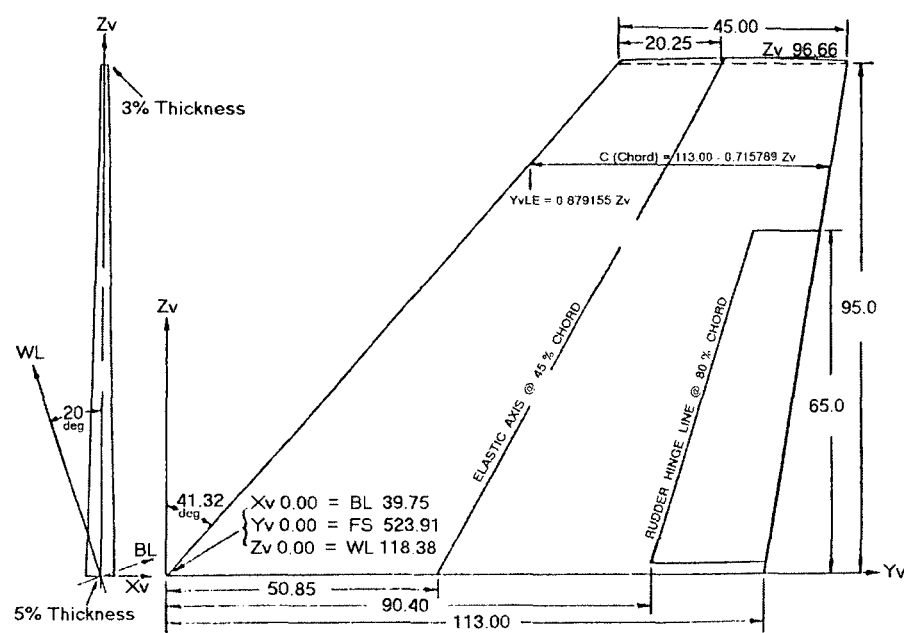
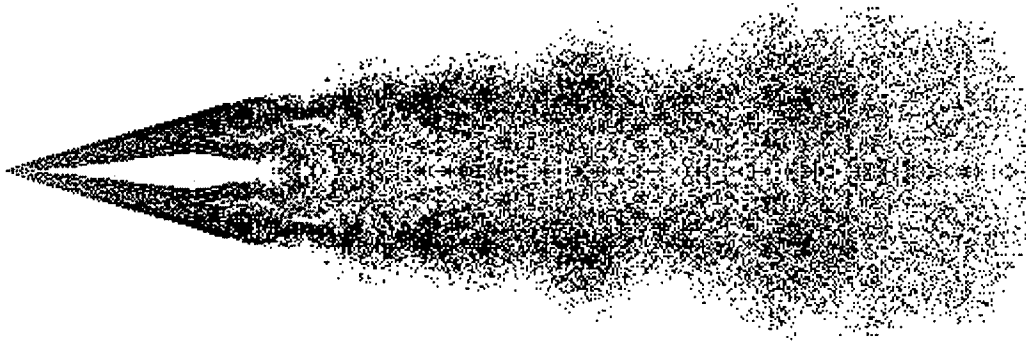
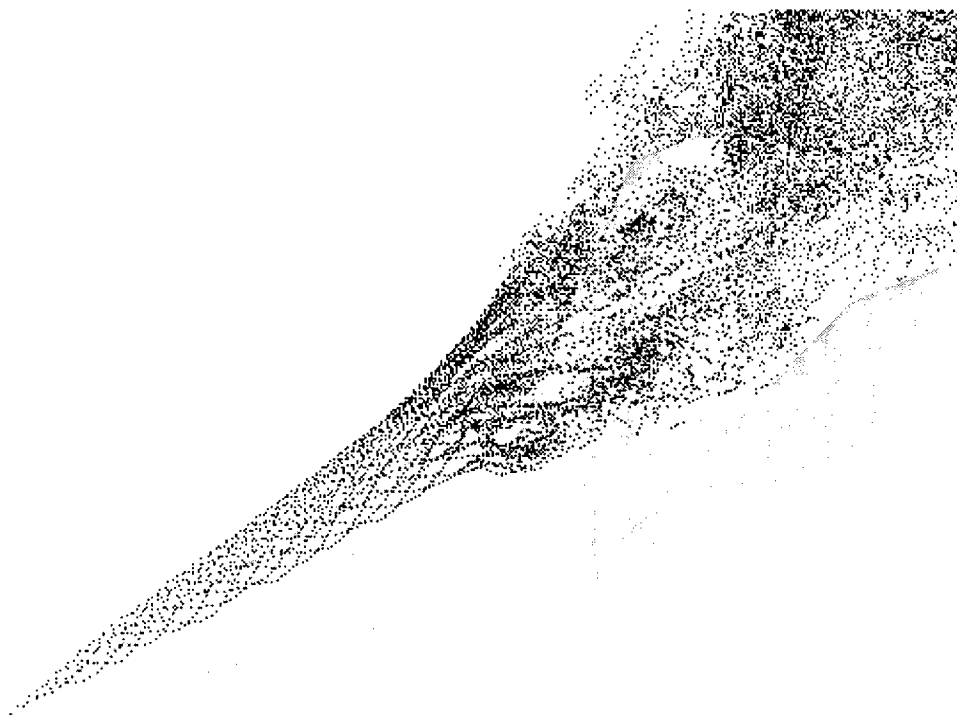


Figure 4 F/A-18 Vertical Tail Geometry



*Figure 5 Top view of vortex wake structure at 20 degrees angle of attack for rigid tail computation*



*Figure 6 Particle traces of the leading edge vortex core at 20 degrees angle of attack for rigid tail computation*

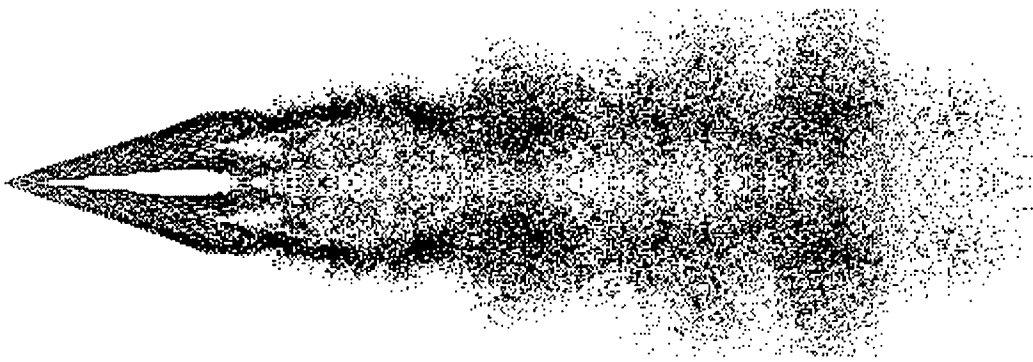


*Figure 7 Top view of vortex wake structure at 30 degrees angle of attack for rigid tail computation*

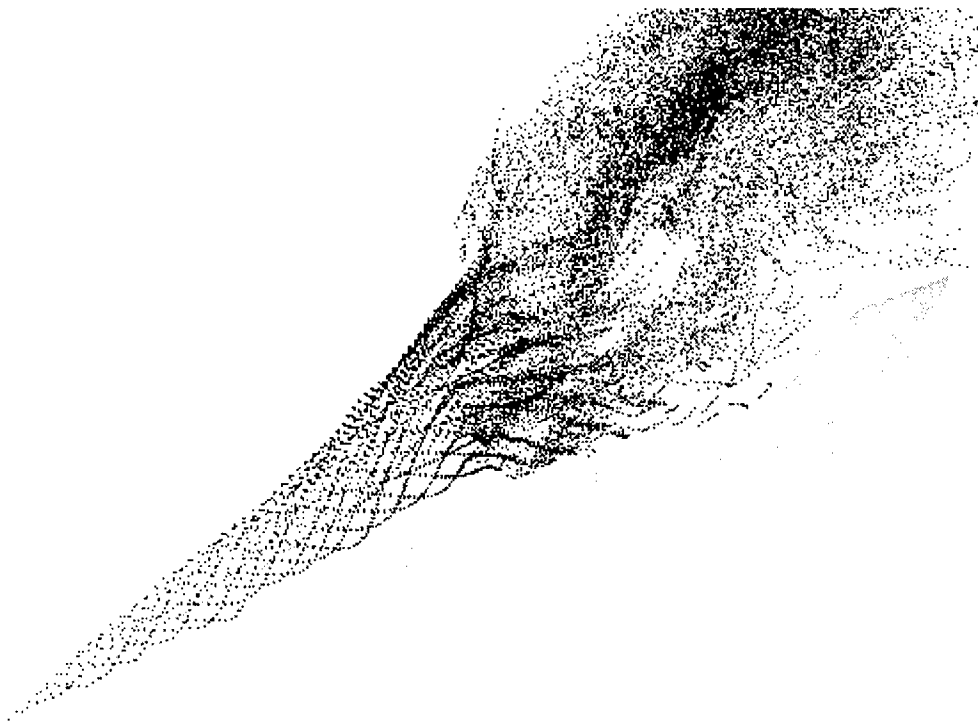


*Figure 8 Particle traces of the leading edge vortex core at 30 degrees angle of attack for rigid tail computation*



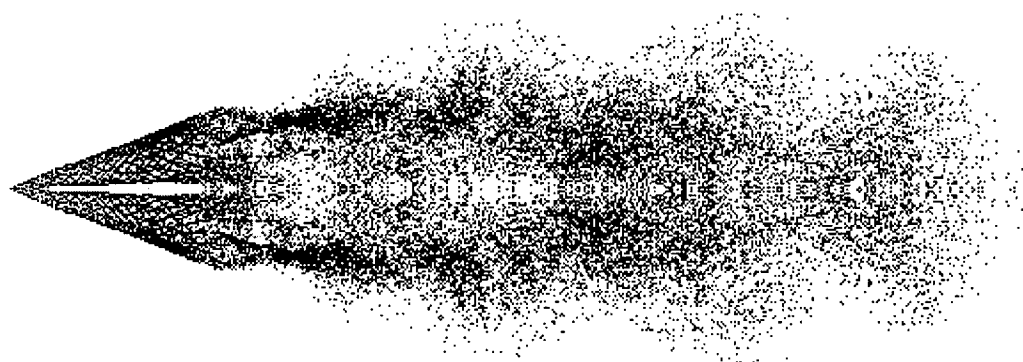


Figure 9 Top view of vortex wake structure at 40 degrees angle of attack for rigid tail computation

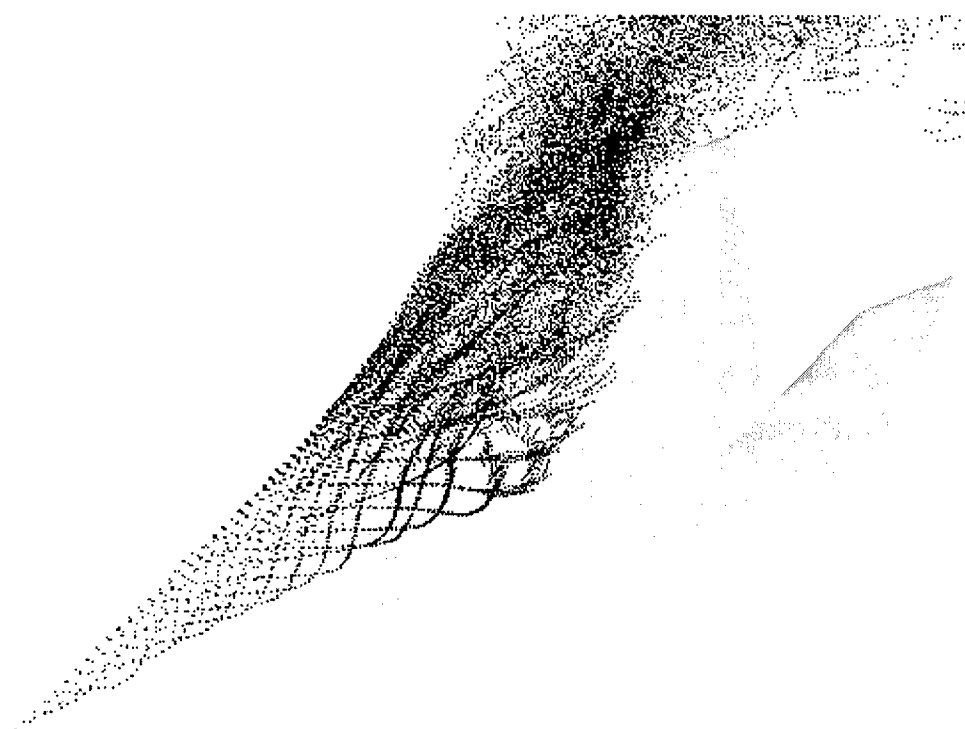
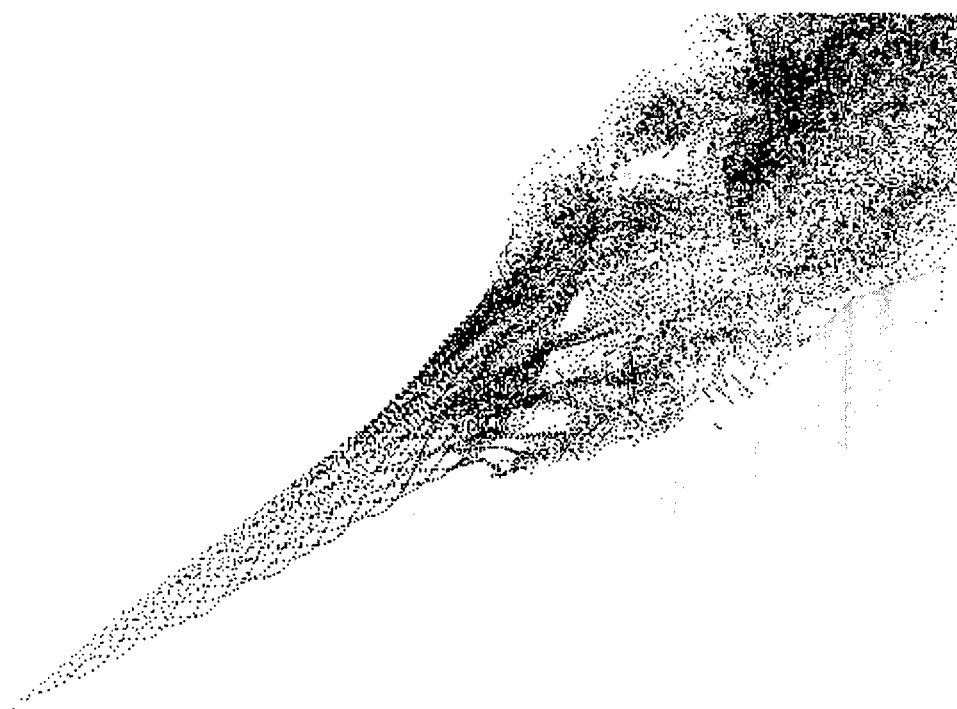


Figure 10 Particle traces of the leading edge vortex core at 40 degrees angle of attack for rigid tail computation



*Figure 11 Top view of vortex wake structure at 20 degrees angle of attack for flexible tail computation*



*Figure 12 Particle traces of the leading edge vortex core at 20 degrees angle of attack for flexible tail computation*

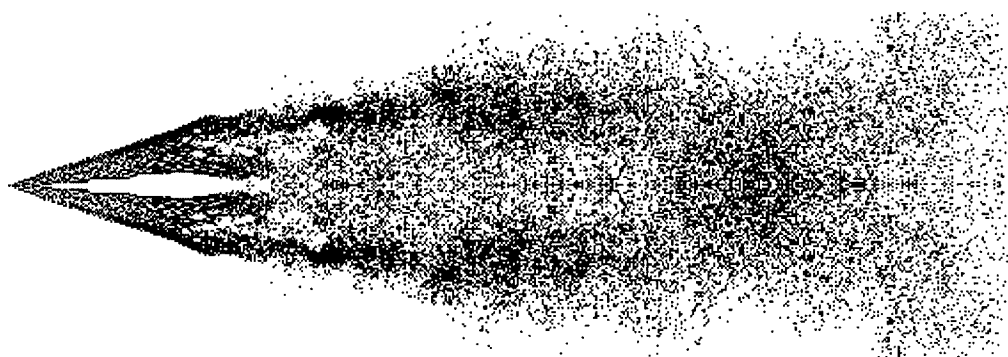


*Figure 13 Top view of vortex wake structure at 30 degrees angle of attack for flexible tail computation*

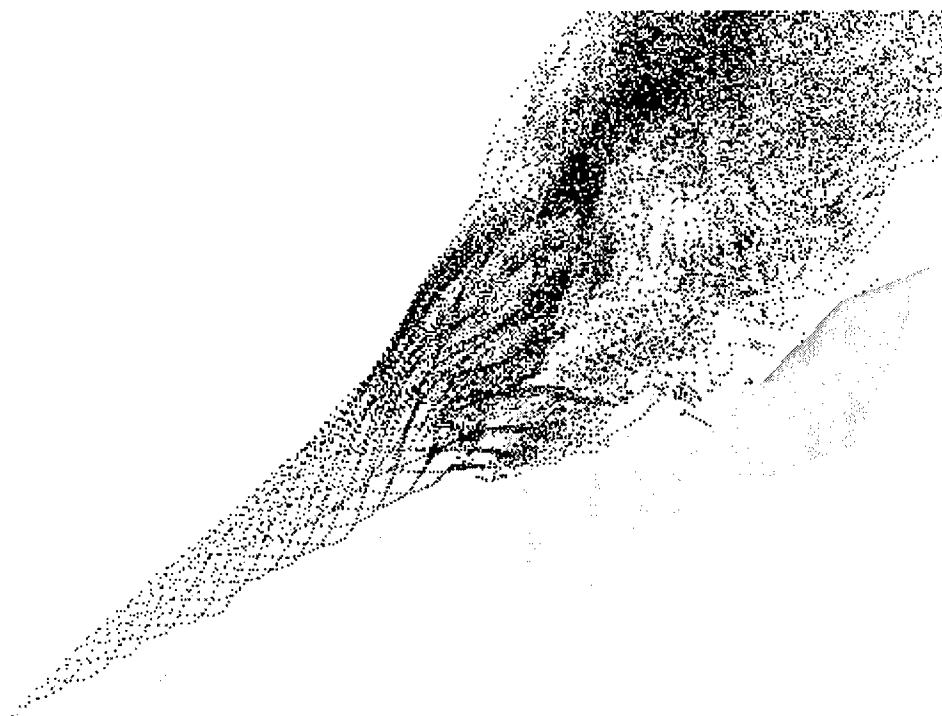


*Figure 14 Particle traces of the leading edge vortex core at 30 degrees angle of attack for flexible tail computation*

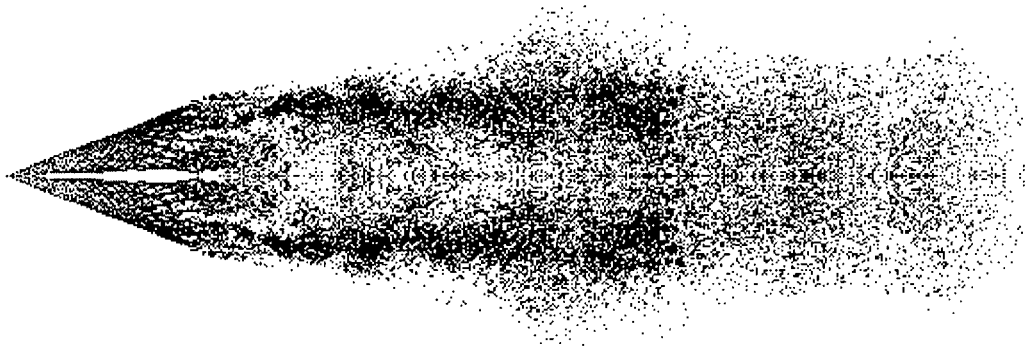


*Figure 15 Top view of vortex wake structure at 40 degrees angle of attack for flexible tail computation*

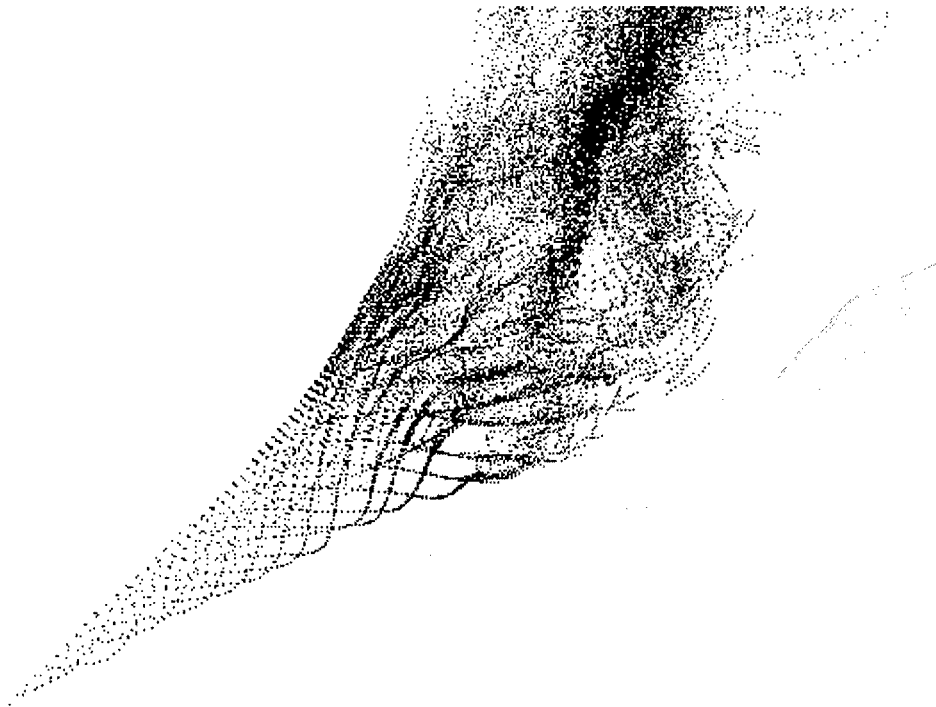


*Figure 16 Particle traces of the leading edge vortex core at 40 degrees angle of attack for flexible tail computation*

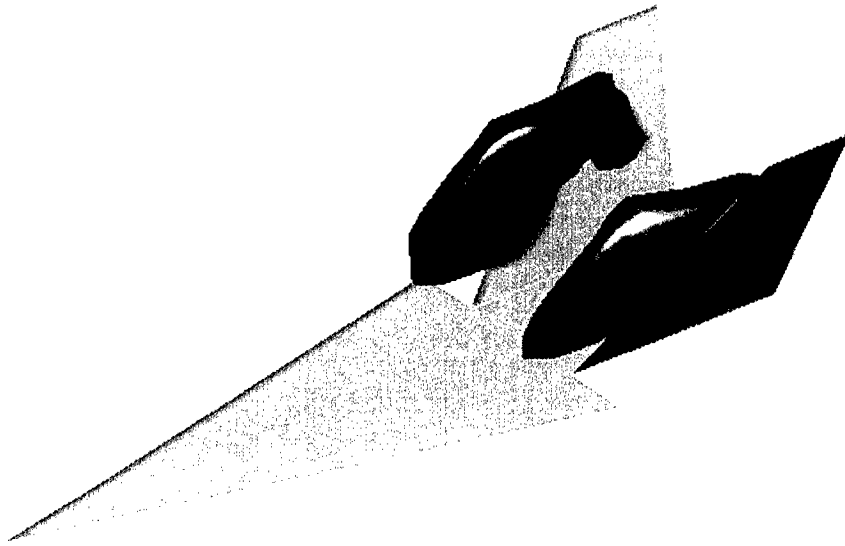


Figure 17 *Iso-surface of time-averaged pressure coefficient at 30 degrees angle of attack for rigid tail computation*

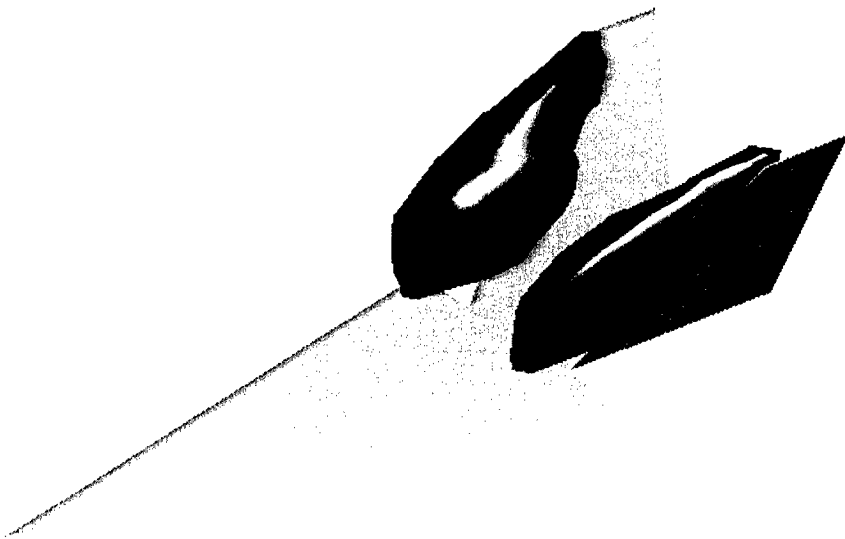


Figure 18 *Iso-surface of time-averaged pressure coefficient at 30 degrees angle of attack for flexible tail computation*

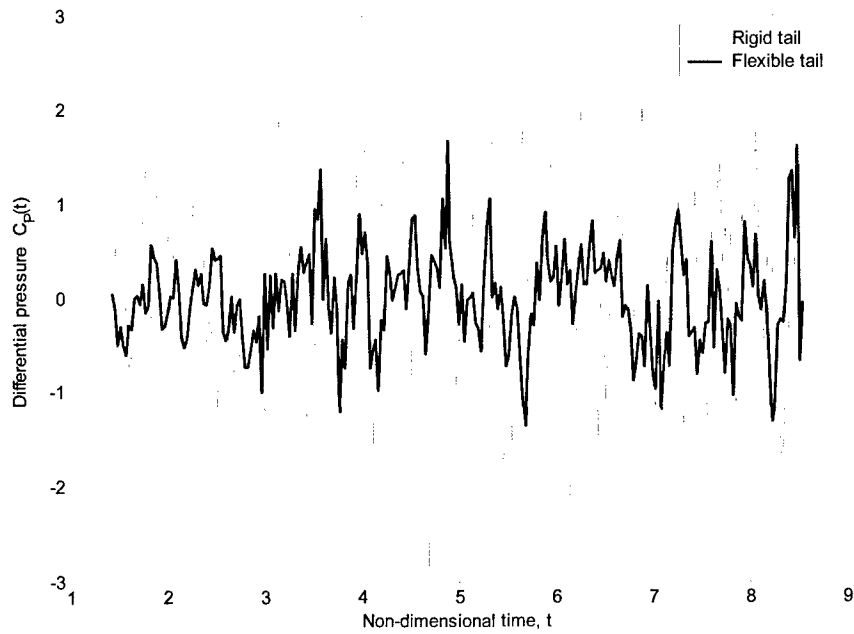


Figure 19 Time history of differential pressure coefficient at 45% chord and 60% span location

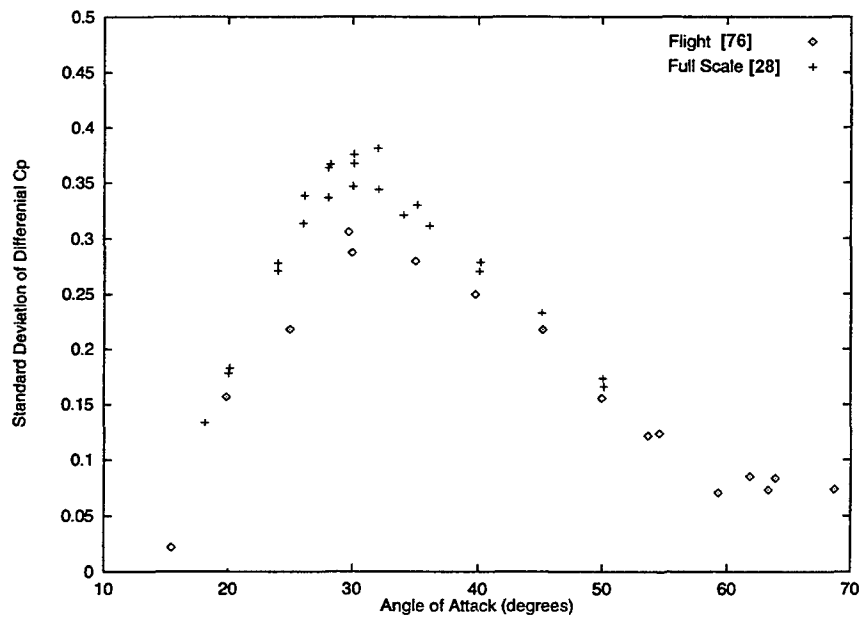


Figure 20 Comparison of RMS differential pressure coefficient values at 45% chord and 60% span location on the tail for full-scale wind tunnel test and in flight (Meyn et al. [30])

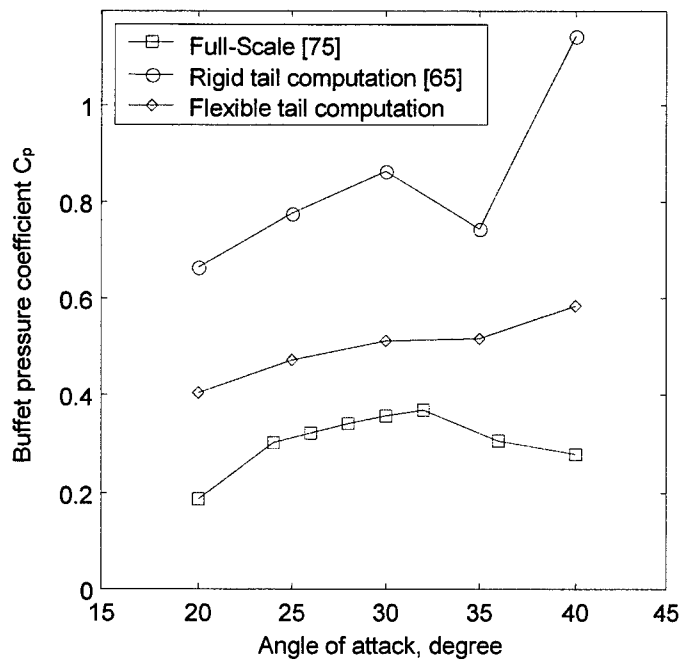


Figure 21 Comparison of RMS differential pressure values at various angles of attack at 60% span, 45% chord location on the tail

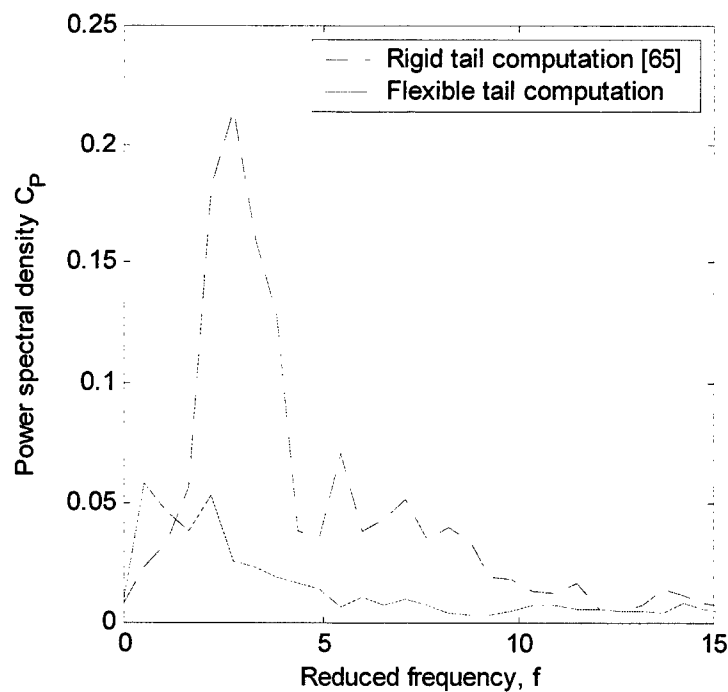


Figure 22 Power spectral density of differential pressure fluctuations at 45% chord and 60% span location on the tail

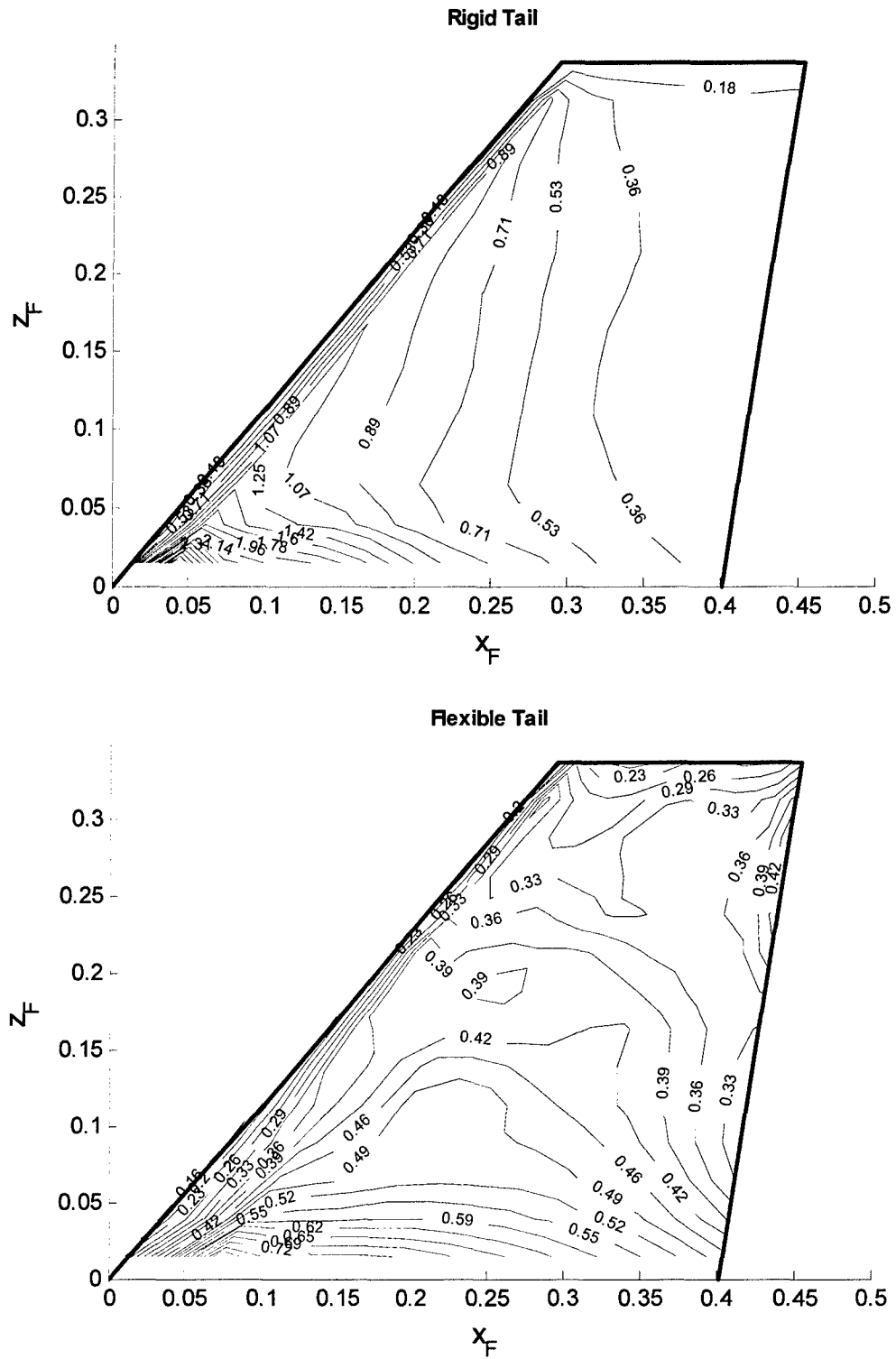
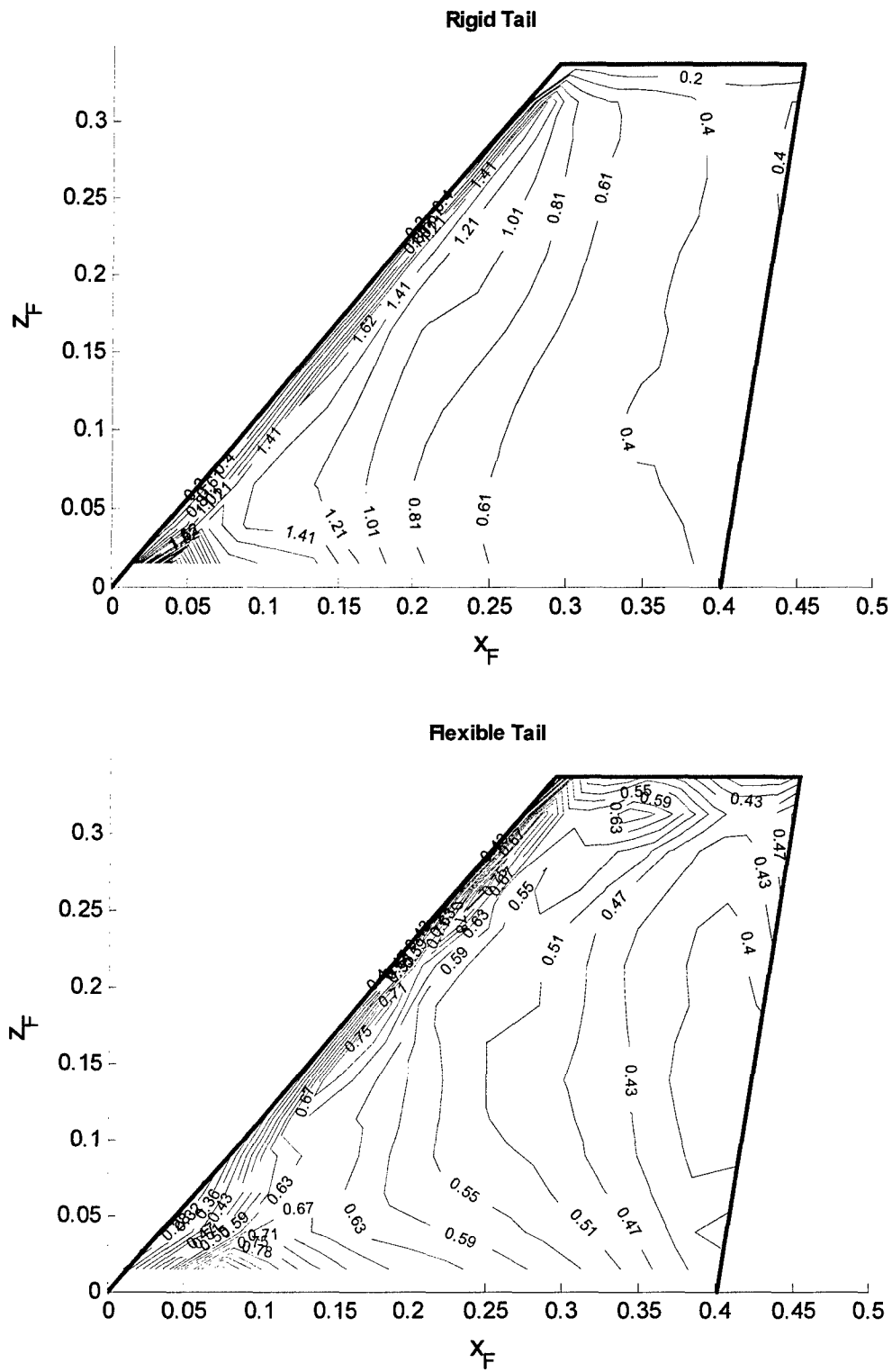


Figure 23 Distribution of RMS differential pressure over the tail at 20 degrees angle of attack







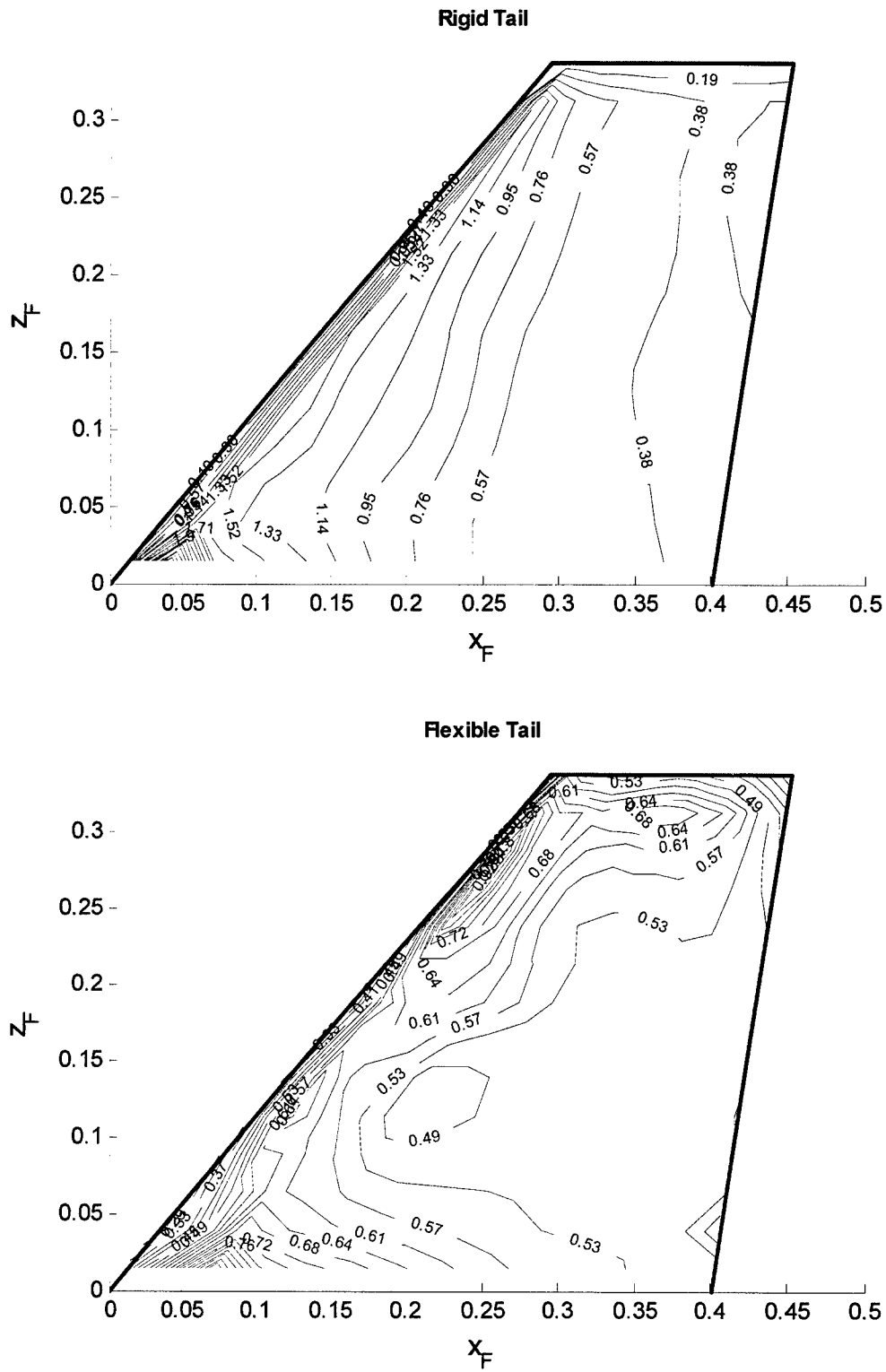


Figure 26 Distribution of RMS differential pressure over the tail at 35 degrees angle of attack

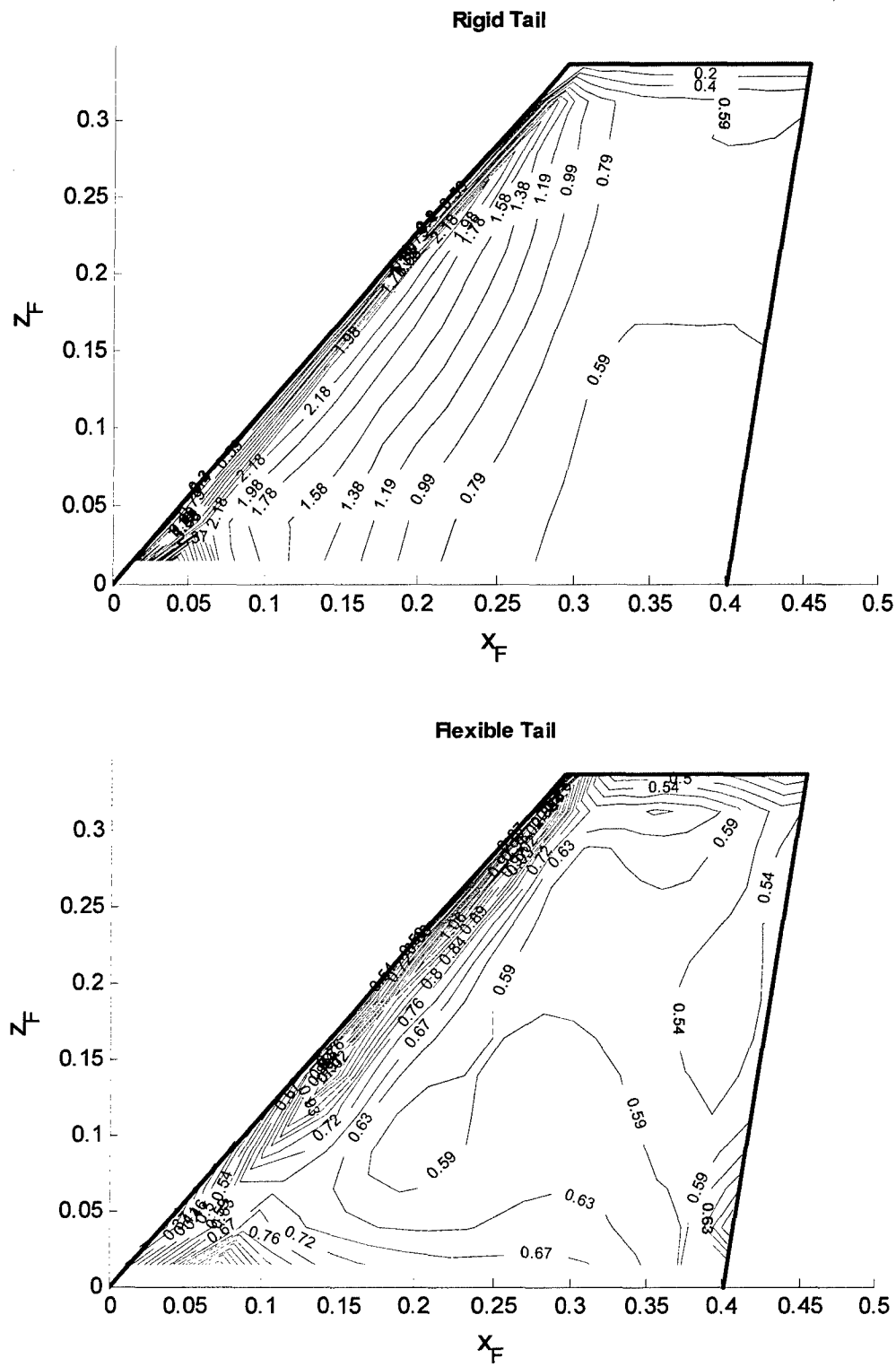


Figure 27 Distribution of RMS differential pressure over the tail at 40 degrees angle of attack

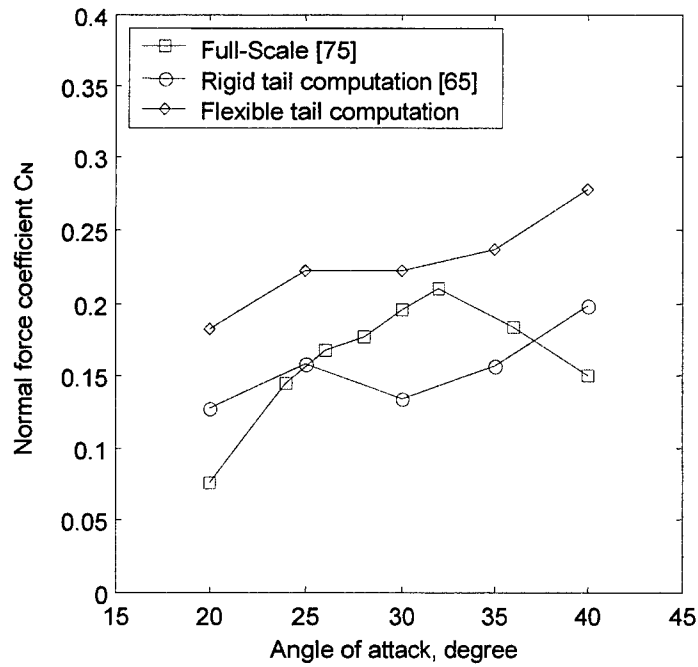


Figure 28 Comparison of RMS normal force coefficient values at various angles of attack

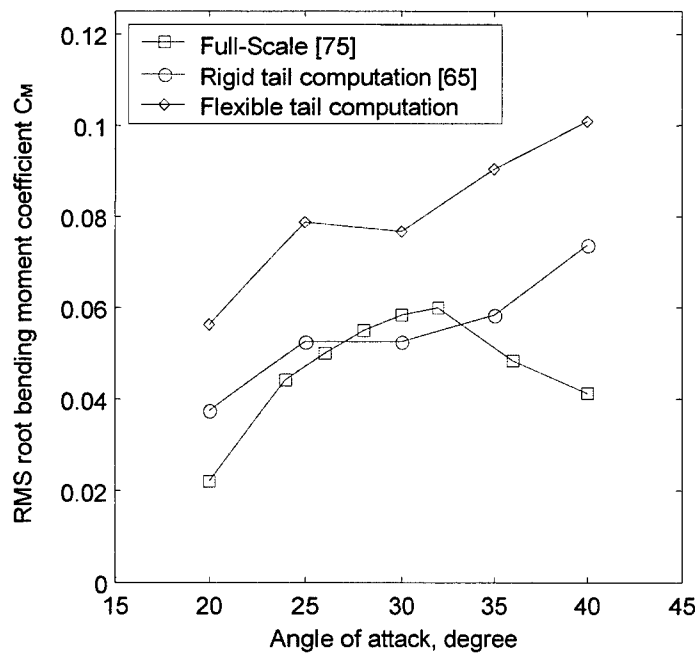


Figure 29 Comparison of RMS bending moment coefficient values at various angles of attack

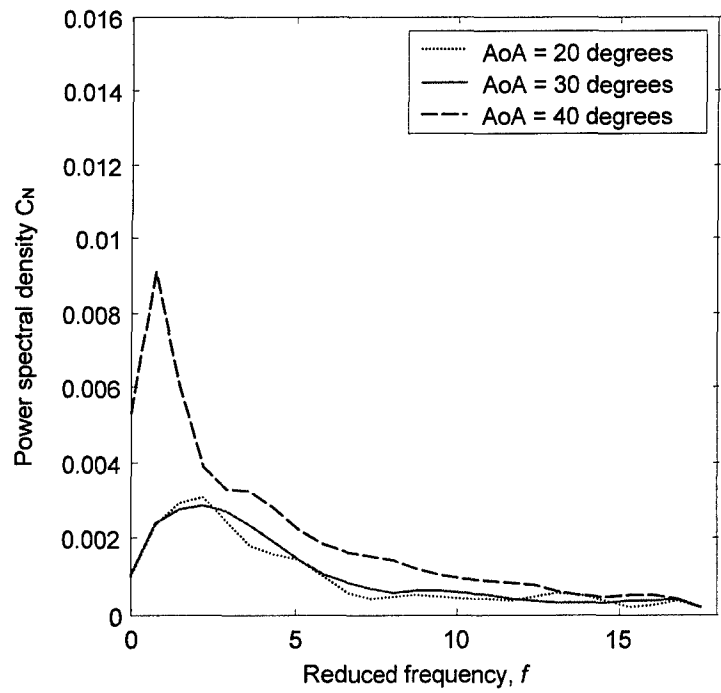


Figure 30 Variation of rigid tail normal force power spectral density with angle of attack

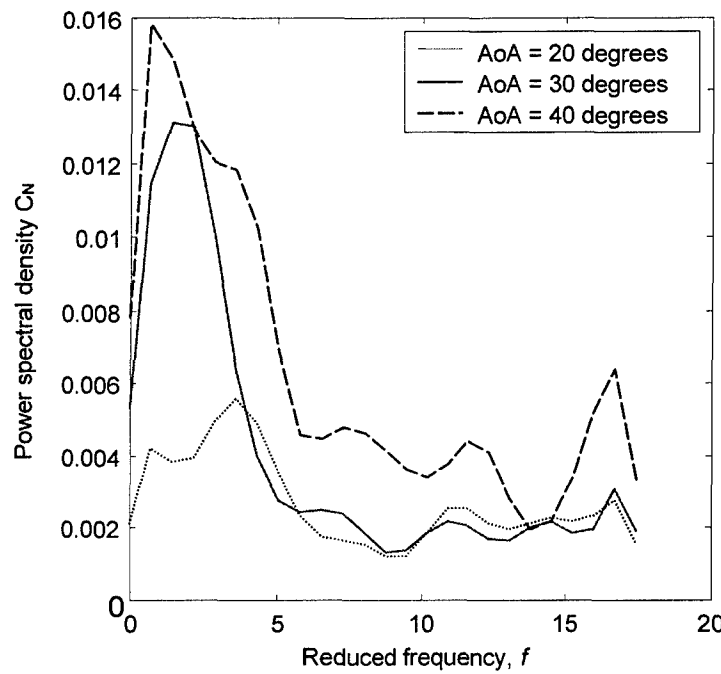


Figure 31 Variation of flexible tail normal force power spectral density with angle of attack

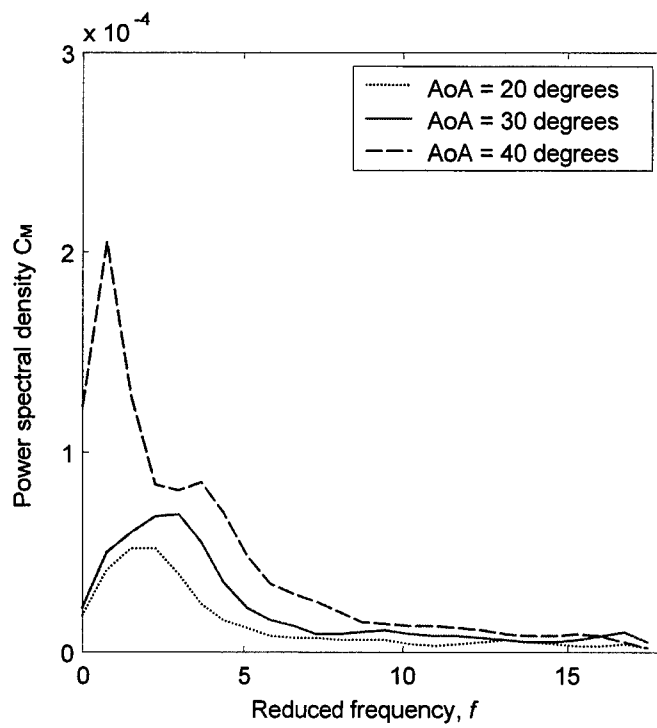


Figure 32 Variation of rigid tail bending moment power spectral density with angle of attack

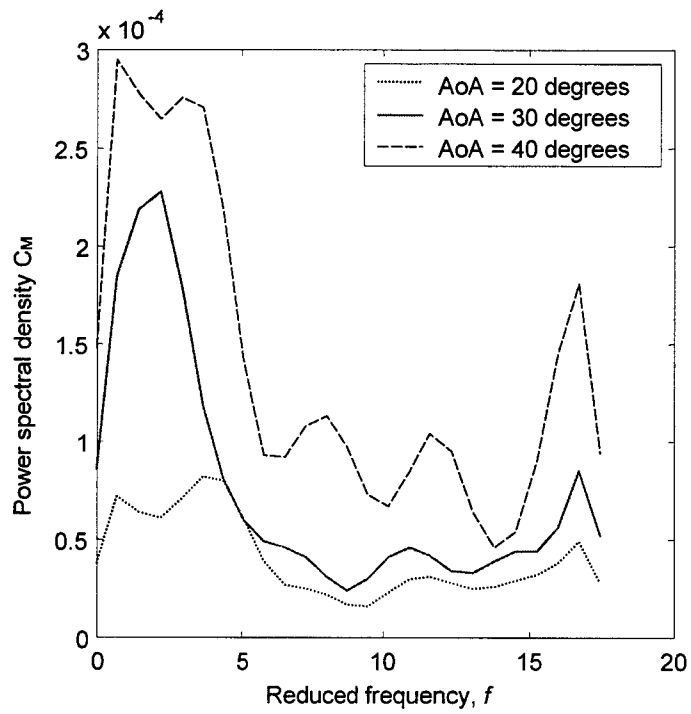


Figure 33 Variation of flexible tail bending moment power spectral density with angle of attack

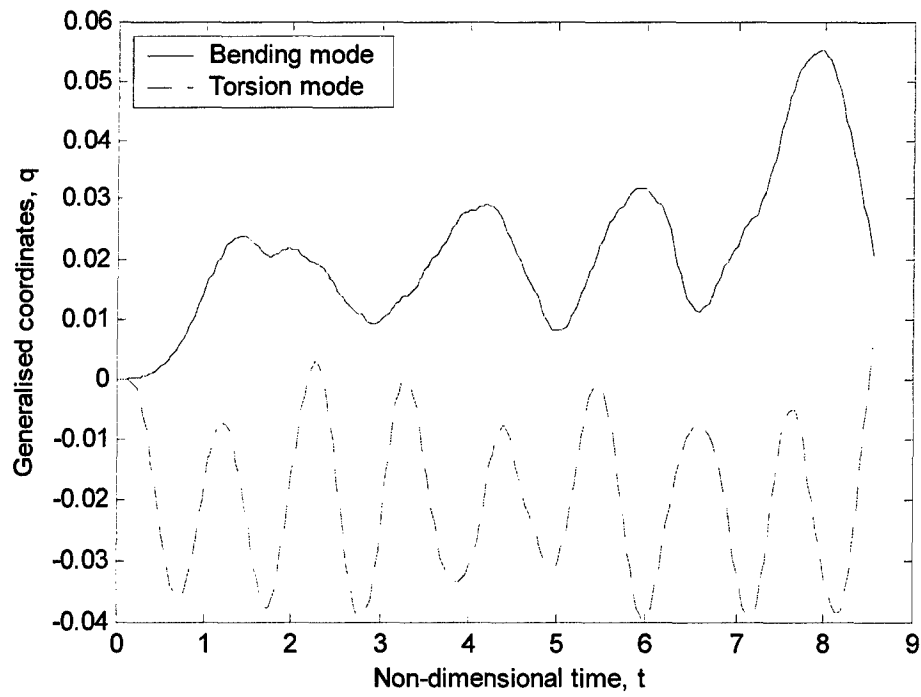


Figure 34 History of generalised coordinates at 20 degrees angle of attack

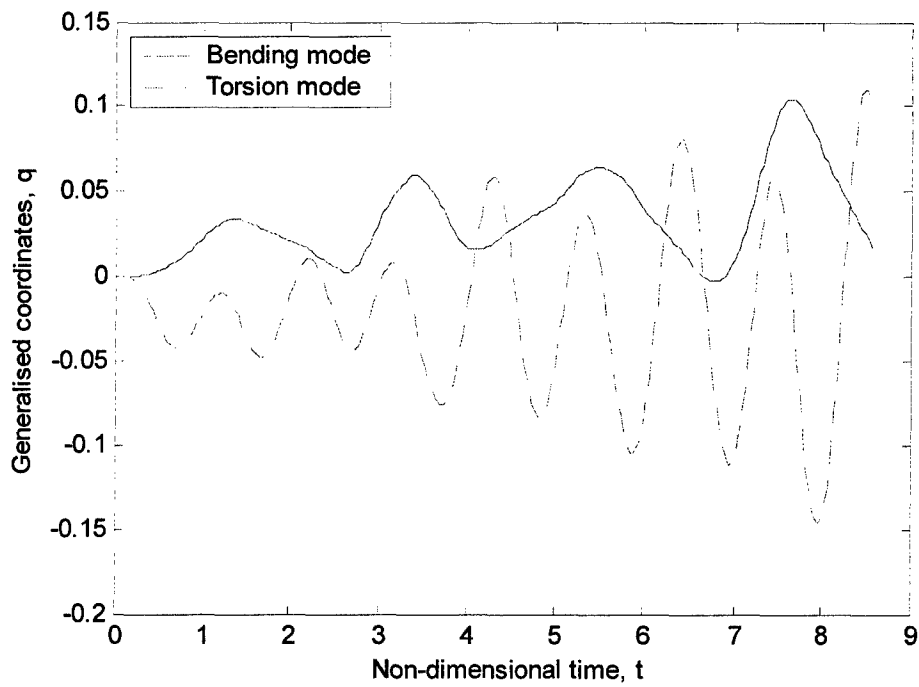


Figure 35 History of generalised coordinates at 25 degrees angle of attack



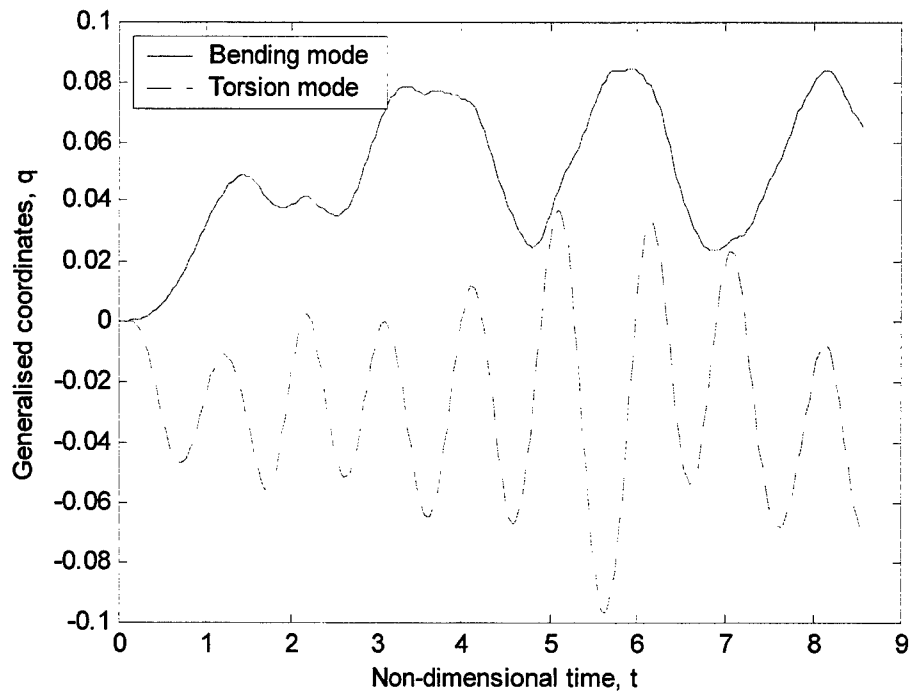


Figure 36 History of generalised coordinates at 30 degrees angle of attack

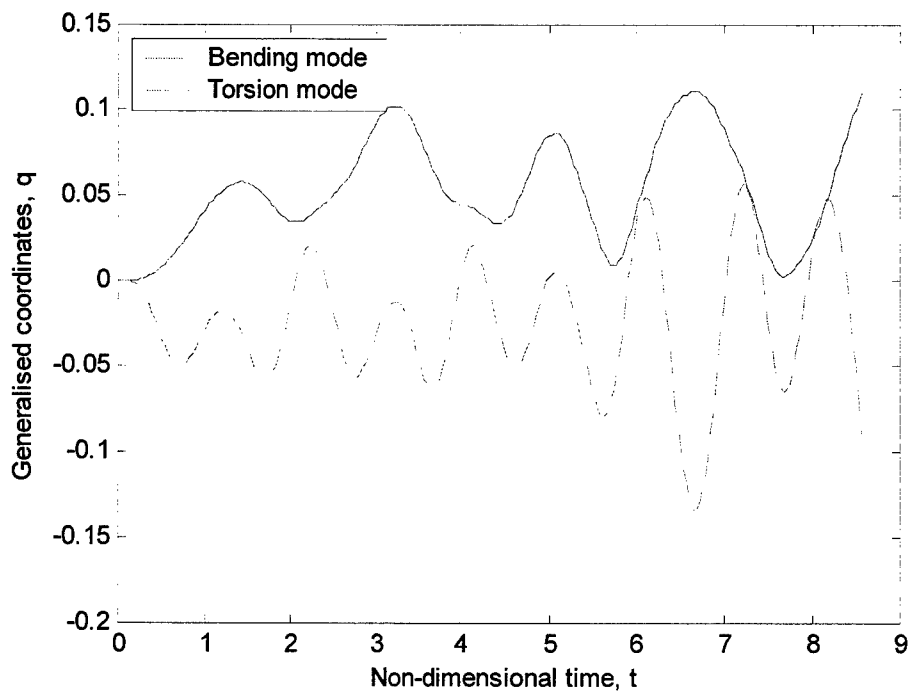


Figure 37 History of generalised coordinates at 35 degrees angle of attack

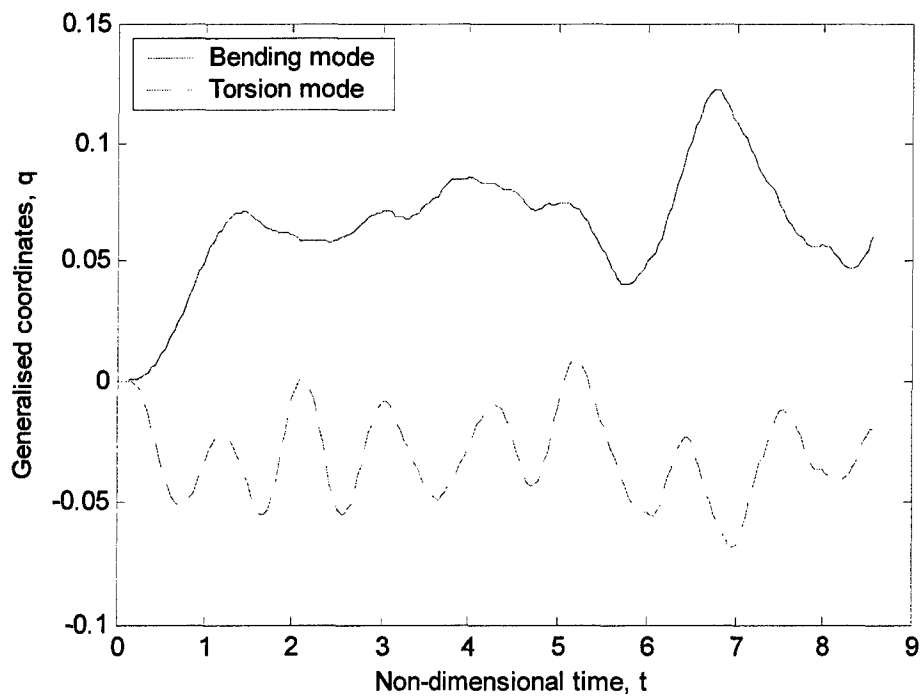


Figure 38 History of generalised coordinates at 40 degrees angle of attack

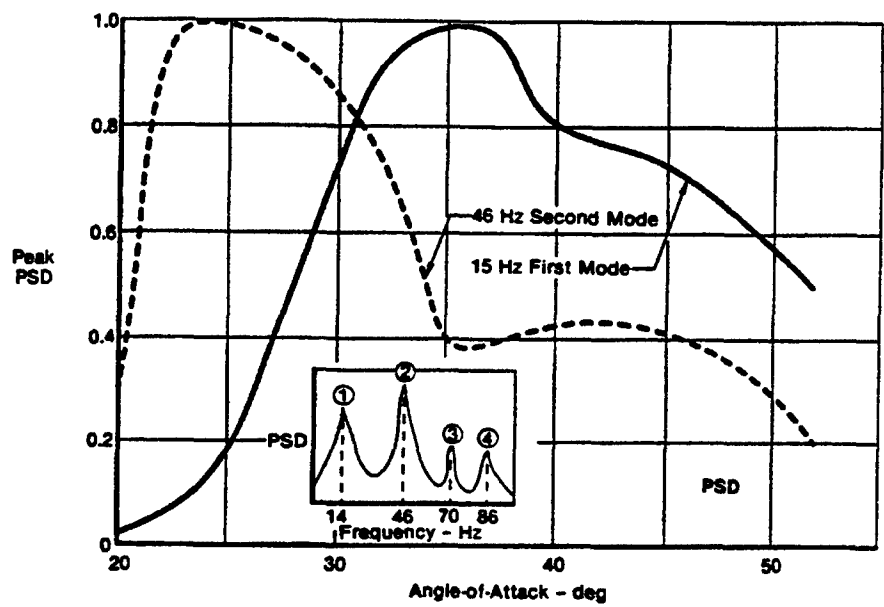


Figure 39 Measured variation of flexible vertical tail dynamic response with angle of attack (Triplett [76])

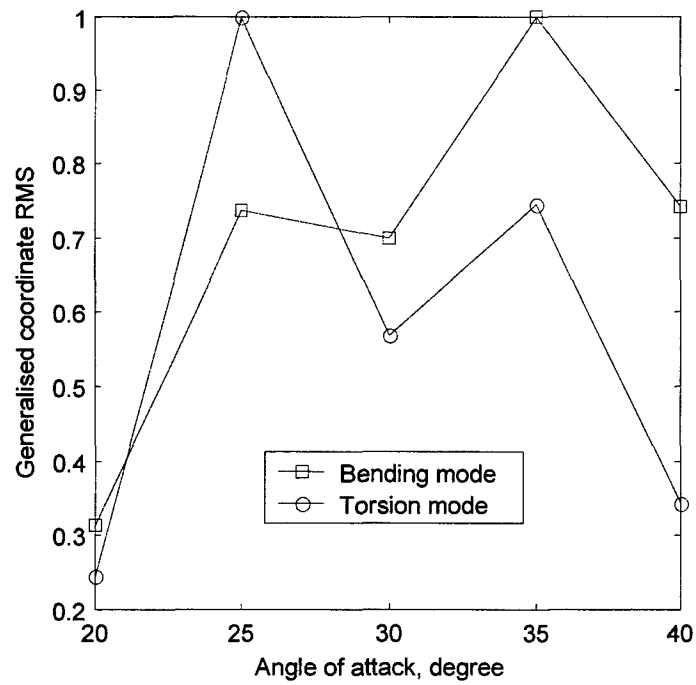


Figure 40 Variation of relative magnitude of bending and torsion modes with angle of attack

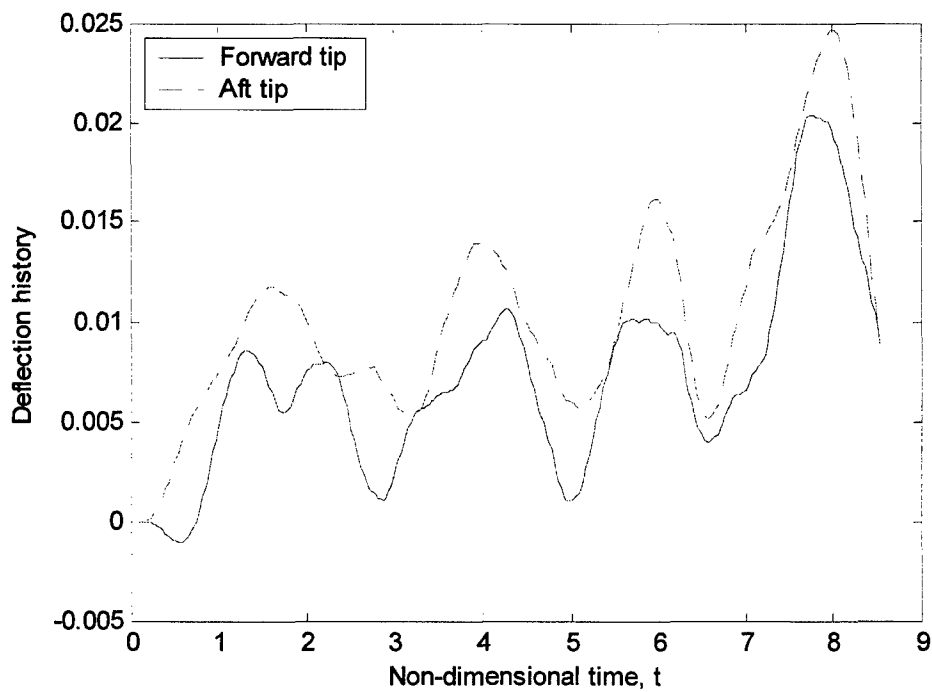


Figure 41 Tail tips deflection history at 20 degrees angle of attack

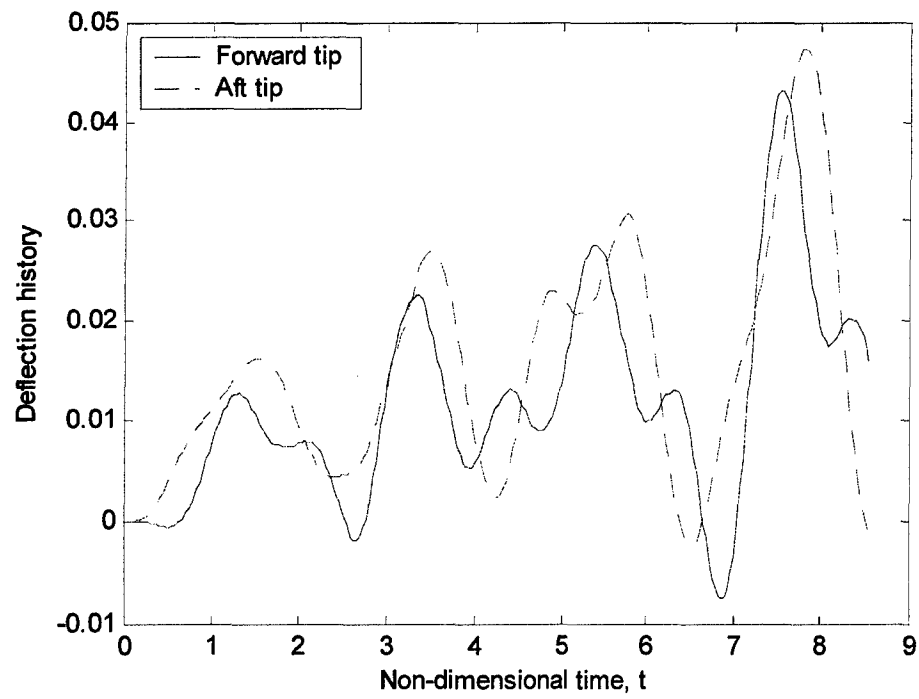


Figure 42 Tail tips deflection history at 25 degrees angle of attack

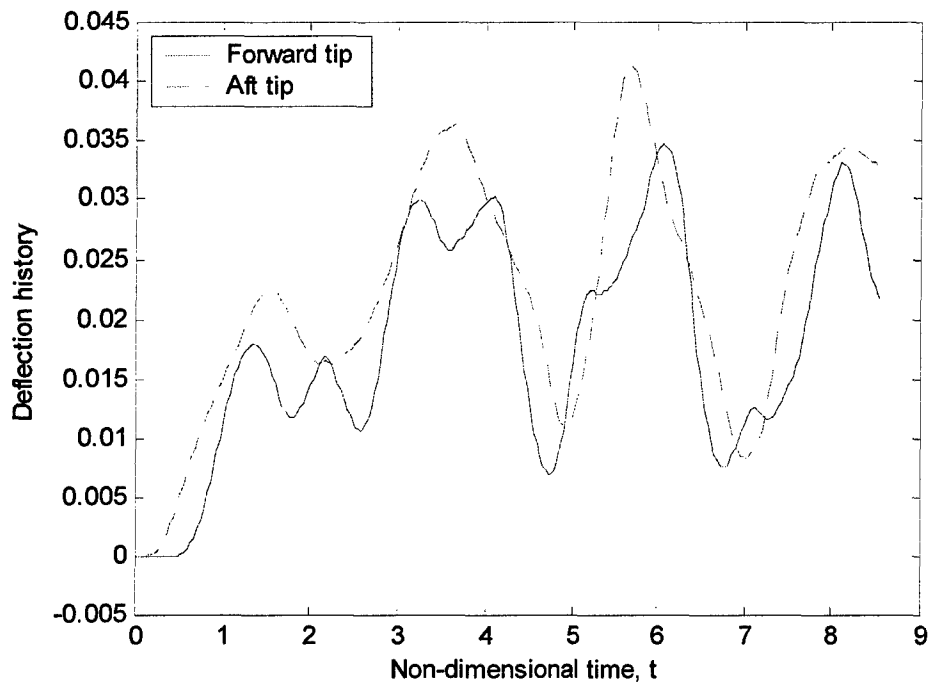


Figure 43 Tail tips deflection history at 30 degrees angle of attack

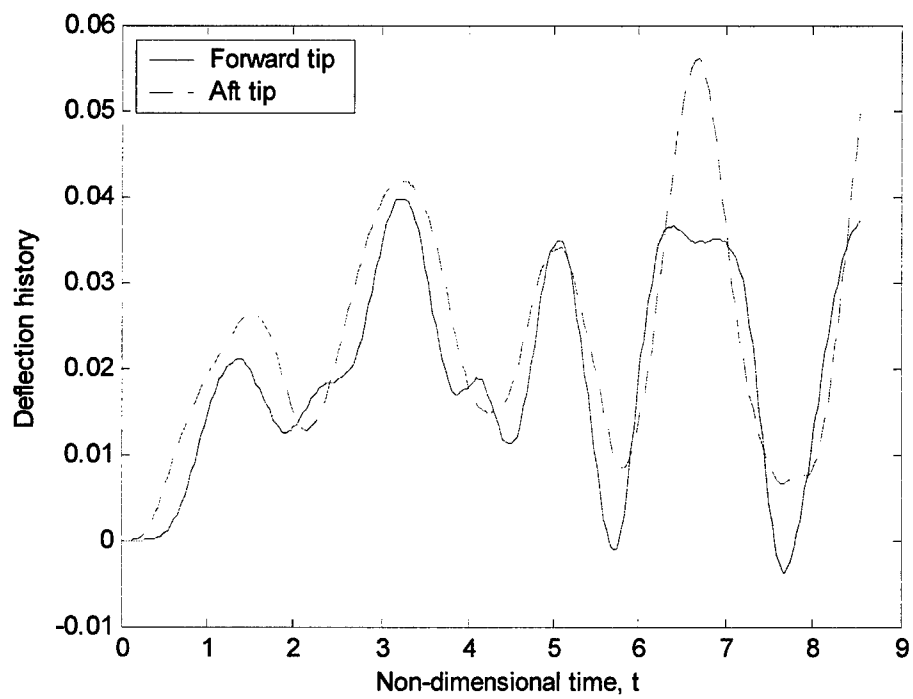


Figure 44 Tail tips deflection history at 35 degrees angle of attack

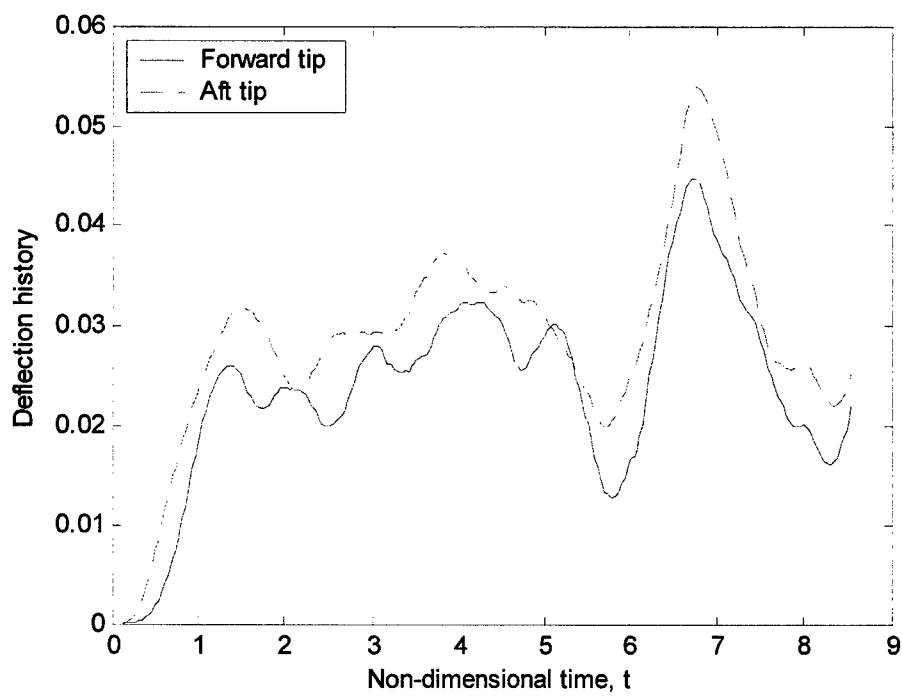


Figure 45 Tail tips deflection history at 40 degrees angle of attack

## DISTRIBUTION LIST

### Vertical Tail Dynamic Response in Vortex Breakdown Flow

Oleg Levinski

### AUSTRALIA

#### DEFENCE ORGANISATION

<b>Task Sponsor</b>	<b>CDR ARDU</b>	<b>1</b>
<b>S&amp;T Program</b>		
Chief Defence Scientist	}	shared copy
FAS Science Policy		
AS Science Corporate Management		
Director General Science Policy Development		
Counsellor Defence Science, London		1 (Doc Data Sheet)
Counsellor Defence Science, Washington		(Doc Data Sheet)
Scientific Adviser to MRDC Thailand		(Doc Data Sheet)
Scientific Adviser Policy and Command		1
Navy Scientific Adviser		(Doc Data Sheet and distribution list)
Scientific Adviser - Army		(Doc Data Sheet and distribution list)
Air Force Scientific Adviser		1
Director Trials		1
<b>Platforms Sciences Laboratory</b>		
Director		1
Chief of Airframes and Engines Division		1
Research Leader		1
Task Manager (Peter Farrell)		1
Author: Dr. Oleg Levinski		2
Loris Molent		1
David Conser		1
<b>DSTO Library and Archives</b>		
Library Fishermans Bend		1
Library Maribyrnong		1
Library Salisbury		2
Australian Archives		1
Library, MOD, Pyrmont		(Doc Data sheet)
US Defense Technical Information Center		2
UK Defence Research Information Centre		2
Canada Defence Scientific Information Service		1
NZ Defence Information Centre		1
National Library of Australia		1
<b>Capability Development Division</b>		
Director General Maritime Development		(Doc Data Sheet)
Director General Land Development		(Doc Data Sheet)
Director General C3I Development		(Doc Data Sheet)

Director General Aerospace Development	(Doc Data Sheet)
<b>Army</b>	
ABCA Standardisation Officer, Puckapunyal	4
SO (Science), DJFHQ(L), MILPO Enoggera, Queensland 4051	(Doc Data Sheet)
NAPOC QWG Engineer NBCD c/- DENGERS-A, HQ Engineer Centre Liverpool	
Military Area, NSW 2174	(Doc Data Sheet)
<b>Air Force</b>	
Aircraft Research and Development Unit	1
DGTA	1
<b>Intelligence Program</b>	
DGSTA Defence Intelligence Organisation	1
Information Centre, Defence Intelligence Organisation	1
<b>Corporate Support Program</b>	
OIC TRS, Defence Regional Library, Canberra	1
<b>UNIVERSITIES AND COLLEGES</b>	
Australian Defence Force Academy	1
Library	1
Head of Aerospace and Mechanical Engineering	1
Serials Section (M list), Deakin University Library, Geelong	1
Senior Librarian, Hargrave Library, Monash University	1
Librarian, Flinders University	1
<b>OTHER ORGANISATIONS</b>	
NASA (Canberra)	1
AGPS	1
<b>OUTSIDE AUSTRALIA</b>	
<b>ABSTRACTING AND INFORMATION ORGANISATIONS</b>	
Library, Chemical Abstracts Reference Service	1
Engineering Societies Library, US	1
Materials Information, Cambridge Scientific Abstracts, US	1
Documents Librarian, The Center for Research Libraries, US	1
<b>INFORMATION EXCHANGE AGREEMENT PARTNERS</b>	
Acquisitions Unit, Science Reference and Information Service, UK	1
Library - Exchange Desk, National Institute of Standards and Technology, US	1
National Aerospace Laboratory, Japan	1
National Aerospace Laboratory, Netherlands	1
<b>SPARES</b>	5
<b>Total number of copies:</b>	<b>55</b>

**DEFENCE SCIENCE AND TECHNOLOGY ORGANISATION  
DOCUMENT CONTROL DATA**

1. PRIVACY MARKING/CAVEAT (OF DOCUMENT)

## 2. TITLE

Vertical Tail Dynamic Response in Vortex Breakdown Flow

3. SECURITY CLASSIFICATION (FOR UNCLASSIFIED REPORTS THAT ARE LIMITED RELEASE USE (L) NEXT TO DOCUMENT CLASSIFICATION)

Document (U)  
Title (U)  
Abstract (U)

## 4. AUTHOR

Oleg Levinski

## 5. CORPORATE AUTHOR

Platforms Sciences Laboratory  
506 Lorimer St  
Fishermans Bend Victoria 3207 Australia

6a. DSTO NUMBER  
DSTO-RR-02566b. AR NUMBER  
AR-012-7906c. TYPE OF REPORT  
Research Report7. DOCUMENT DATE  
June 20038. FILE NUMBER  
2002/58624/19. TASK NUMBER  
AIR 00/14210. TASK SPONSOR  
CDR ARDU11. NO. OF PAGES  
7712. NO. OF REFERENCES  
76

## 13. URL on the World Wide Web

<http://www.dsto.defence.gov.au/corporate/reports/DSTO-RR-0256.pdf>

## 14. RELEASE AUTHORITY

Chief, Air Vehicles Division

## 15. SECONDARY RELEASE STATEMENT OF THIS DOCUMENT

*Approved for public release*

OVERSEAS ENQUIRIES OUTSIDE STATED LIMITATIONS SHOULD BE REFERRED THROUGH DOCUMENT EXCHANGE, PO BOX 1500, EDINBURGH, SA 5111

## 16. DELIBERATE ANNOUNCEMENT

No Limitations

## 17. CITATION IN OTHER DOCUMENTS

Yes

## 18. DEFTEST DESCRIPTORS

FA/18 aircraft, Airframes, Tail assemblies, Fatigue tests, Aeroelasticity, aerodynamic loads, Buffeting, Vorticities

## 19. ABSTRACT

The paper describes the development of an aeroelastic model for the prediction of empennage dynamic response due to vortex induced buffet loads. The multidisciplinary problem of tail buffeting is solved accurately in the time domain using an unsteady vortex model for prediction of aerodynamic loads and coupled aeroelastic equations for the bending and torsional deflections of the tail which are resolved using the Galerkin method. A dynamic aeroelastic analysis of empennage buffet is performed for a generic delta wing, twin vertical-tail configuration at high angles of attack. Results of computations are validated using experimental and flight test data. The present research provides advances in the predictive capability and our understanding of aircraft empennage buffet.